CAAP Final Report

Date of Report: January 9, 2019

Prepared For: *U.S. DOT Pipeline and Hazardous Materials Safety Administration*

Contract Number: DTPH5615HCAP10

Project Title: *Chemically Bonded Porcelain Enamel Coated Pipe for Corrosion Protection and Flow Efficiency*

Prepared By: *Liang Fan and Genda Chen from Missouri University of Science and Technology*
Signo Reis and Michael Koenigstein from Roesch Inc.

Contact Information: *Genda Chen, Ph.D., P.E., Email: gchen@mst.edu,*
Phone: (573) 341-4462

Table of Contents

List of Tables

List of Figures

I. Introduction

Natural gas, oil and hazardous liquid transmission and gathering pipelines have reached 484,000 miles in the U.S. [1]. Despite the best effort made to ensure safe operations, over 10,620 pipeline incidents occurred from 1994 to 2013, resulting in substantial property damage and significant injuries. These incidents were caused by natural forces (e.g. wind gusts, heavy rains/floods, lightening), excavations from third parties or operators, operation negligence, corrosion, and material defects. Among them, corrosion is the second cause to excavation for pipeline failure, accounting for 20% of the total loss. According to a 2002 survey performed by NACE International, the average, annual, corrosion-related costs for U.S. pipeline operators to monitor, replace and maintain assets for both transmission and distribution services is over $12 billion. Therefore, corrosion problems and their impact on our nation's economy and prosperity cannot be treated light in any measure.

Metallic pipelines can be corroded both internally and externally. According to the statistical data released by the U.S. Department of Transportation Pipeline and Hazardous Materials Safety Administration (PHMSA), internal corrosion accounted for 74% of the significant corrosion related incidents in 2013. Several factors account for pipe internal corrosions, like chemical ingredients of the transported commodities, crude oil or gas flow rate, and operational temperature. For oil pipelines, water that is transported along with crude oils or carried by solid particles can drop out of the crude oil and come in contact with the pipe surface [2]. When water accumulates and persists on the pipe floor for an extended period of time, internal corrosion happens. For gas pipelines, corrosion can take place when the internal surface is exposed to moisture and contaminants such as chlorides, CO_2, and sulfur compounds, forming electrolytes for electrochemical reactions [3]. Once internal corrosion happens, it will gradually reduce the pipeline wall thickness and mechanical strength, leading to severe pipeline leakage or rupture and posing tremendous threat to the surrounding neighborhood [4].

Pipelines can be protected from internal corrosion by controlling the quality of transported commodities, applying internal coatings and adding corrosion inhibitors. Among these methods, protective coating is the most cost-effective method for pipeline protection.

Internal pipeline linings are commonly divided into three categories: concrete, rubber, and plastics. However, concrete can result in smaller inside diameter with undesirable roughness. Rubber-lined pipe is not oil, flame or abrasion resistant and is susceptible to temperature change [5]. Fusion-bonded epoxy (FBE) coating is the most popular physical barrier in corrosion protection for pipelines. Although widely used, the protective coatings exhibited some undesirable characteristics. FBE coating is low in impact and abrasion resistances but high in moisture absorption. Most importantly, it has low adhesion to steel pipe, which promotes under-film corrosion.

Porcelain enamel coating is unique in being chemically bonded to steel pipe for corrosion protection and providing a glassy surface for flow efficiency. This promising technology can overcome the under-film corrosion associated with debonded coating in pipeline operations. It can also reduce pressure loss along the length of a pipeline for cost effectiveness in liquid and natural gas transport. Besides, the coating can facilitate pipeline cleaning and water disposal after hydrostatic testing [6].

To date, previous studies (Yan et al., 2011; Tang et al., 2012; 2013) have been limited to the application on reinforcing bars in concrete structures [7-9]. Further studies are needed for pipeline applications due to different steel composition, geometry and shape of steel parts, operational and environmental conditions, and design objectives. The metal oxides in enamel react with carbon and iron in steel to create alloys, which promote enamel to steel adhesion. However, the high carbon content can cause voids and pinholes on the enamel surface due to the release of gaseous CO and CO_2 during the firing process. Since the carbon content in pipeline steel is much lower than that used in reinforcement, it is easier to minimize or eliminate the bubbles and substantially reduce surface defects and roughness. Besides, unlike the deformed surface of reinforcing bars in concrete structures, the smooth surface of pipes will not cause a non-uniform layer of coating. As such, the corrosion resistance of enamel-coated pipes expects to be significantly higher than that of the enamel-coated bars in concrete structures.

Transmission pipelines are often embedded underground, externally exposed to soils with various microbes and corrosive environment, and internally exposed to pressurized liquids and natural gas. Due to corrosion or other reasons, the thin wall of the existing pipeline is sometimes uneven and not smooth prior to enamel coating. In this case, the stress concentration may occur around various dents due to internal pressure and thermal effect due to enameling process. Both residual stress and stress concentration can contribute to the Stress Corrosion Cracking (SCC) of enamel-coated steel in even a mildly corrosive environment. SCC is a cracking process of susceptible metals under a simultaneous action of corrosive environment and sufficient tensile stress, which can lead to unexpected sudden failure of steel pipes. Therefore, it is necessary to study SCC of steel pipes under the combination of thermal effect, external soil pressure, and internal pressure during operation.

II. Objectives and Scope of Work

The overarching goal of this study is to improve the corrosion protection and safety, and to reduce the pressure loss and operational cost of hazardous liquid and natural gas pipelines. To achieve the goal, this study aims to explore and develop chemically-bonded enamel coating (200-300 um) for coating uniformity, low surface roughness and high coating efficiency, and corrosion resistance. The objectives will be achieved both experimentally and numerically in the following four research tasks:

1. Optimization of enamel materials for durability, particle distribution, and thermal compatibility with steel;
2. Enameling process for coating uniformity, surface roughness, and efficiency without adverse effect on steel properties;
3. Characterization of enamel-coated pipe for microstructure/porosity, chemical adhesion, and corrosion resistance; and
4. System performance of in-situ, enamel-coated pipelines – stress distribution under thermal, external and internal pressure, and stress corrosion cracking.

III. Task 1- Optimization of enamel materials for durability, particle distribution, and thermal compatibility with steel

1. Experimental Program

API 5L X65 steel pipe (MRC Global) with an outside diameter of 323.850 mm and a wall thickness of 9.525 mm was used in this study. Small samples (25 mm × 50 mm) were cut from the full-size pipe. The chemical composition and physical properties of the steel pipe are given in Table 1.1

and Table 1.2, respectively. In Table 1.2, CTE stands for the Coefficient of Thermal Expansion, which was measured using Orton dilatometer.

Table 1.1 Chemical composition of steel pipe

Element	C	Mn	P	S	Si	Cu	Ni	Cr	Mo	Al	V	B	Ti	Cb	Fe
Wt.%	0.17	1.15	0.07	0.02	0.26	0.10	0.04	0.07	0.07	0.024	0.02	0.001	0.001	0.001	98.003

Table 1.2 Physical property of steel pipe

Grade	Yield Strength (ksi)	Ultimate Strength (ksi)	Yield/Ultimate Strength Ratio	Elongation %	CTE (ppm/℃)
API 5L X65	70	80	0.875	38.2	21.4

The thermal properties of the enamel coatings were tested with Orton dilatometer. The particle size distribution of enamel materials was determined by Mo-Sci in Rolla, MO. Light scattering particle size analyzer was used in particle size analysis. To examine the microstructure of each coating, enamel-coated samples were cold mounted in epoxy resin (EpoxyMount, Allied High-Tech Products, Inc.). Each sample was cut into a 10.0 mm thick cross section using a diamond saw. The 10.0 mm thick slice samples were abraded with silicon carbide papers with grits of 80, 180, 320, 600, 800, and 1200. After abrading, all samples were rinsed with deionized water and dried in air at room temperature. The microstructure of each sample was examined using a scanning electron microscopy (SEM, Hitachi S-4700, Tokyo). After corrosion tests, the samples were removed from the sodium chloride solution, washed with distilled water, and dried at room temperature. After drying, the surface conditions on enamel-coated samples, especially those with small corrosion products, were examined in detail.

The full-size pipe was cut into small samples (25 mm × 50 mm) in longitudinal and circumferential directions. Each sample was soldered with a copper wire to provide an electrical connection for corrosion tests. All sides of the sample except the front enamel coated surface were covered with marine epoxy (LOCTITE) to ensure that corrosion takes place through the enamel.

Electrochemical tests were conducted to understand the corrosion resistances of these five enamel coatings. All samples were immersed in 3.5 wt.% sodium chloride solution, which was prepared by adding purified sodium chloride (Fisher Scientific, Inc.) into distilled water. The samples were tested at room temperature with a typical three-electrode setup, including a 25.4 mm × 25.4 mm × 0.254 mm platinum sheet as a counter electrode, saturated calomel electrode (SCE) as a reference electrode, and the sample as a working electrode. All three electrodes were connected to a Gamry, Interface1000E Potentiostat for data acquisition. Before linear polarization resistance (LPR) and electrochemical impedance spectroscopy (EIS) tests, a stable corrosion potential was obtained by immersing the specimens in the sodium chloride solution for about 1.0 hour. Then the LPR curves were measured within 15 mV around the corrosion potential at a scan rate of 0.167 mVs^{-1}. Afterwards, the EIS test, which is used to study the resistance of the coating to corrosion, was conducted at ten points per decade around the corrosion potential, with a sinusoidal potential wave of 10 mV in amplitude and a frequency ranging from 100 kHz to 5 mHz. For each coating type, three samples were prepared and tested, and only the results of representative samples were demonstrated in this report.

2. Results and Discussion

2.1 Enamel 15R-972 and 16R-001

Two commercially-available silicate glass slurries (with clay and borax) (product ID 15R-972 and 16R-001, PEMCO) were used to prepare coatings for steel samples. The compositions of the coating are shown in Table 1.3 and Table 1.4.

Table 1.3 Chemical composition of alkali borosilicate glass: 15R-972

Element	SiO_2	B_2O_3	Na_2O	C_aO	M_nO_2	Al_2O_3	T_iO_2	K_2O	Fe_2O_3	M_gO	P_2O_5	Others
Wt.%	47.73	23.17	10.6	7.58	3.58	2.16	1.92	1.25	1.12	0.41	0.39	0.09

Table 1.4 Chemical composition of alkali borosilicate glass: 16R-001

Element	SiO_2	B_2O_3	Na_2O	C_aO	M_nO_2	Al_2O_3	T_iO_2	K_2O	Fe_2O_3	M_gO	P_2O_5	Others
Wt.%	56.13	19.37	6.34	5.67	0.60	6.05	4.38	0.48	0.45	0.40	0.05	0.08

2.1.1 Particle size analysis

For particle size analysis, the 15R-972 and 16R-001 enamel slurries were dried at 150 °C. Table 1.5 shows the particle volume percentage in different diameter ranges. The particle distributions of the two enamels are presented in Figure 1.1.

Table 1.5 Particle distributions of two types of coating powder by volume percentage

Diameter (μm)	15R-972 Volume (%)	16R-001 Volume (%)
1.385	0.000	0.001
1.520	0.001	0.013
1.669	0.015	0.076
1.832	0.088	0.227
2.011	0.256	0.463
2.207	0.521	0.748
2.423	0.833	1.064
2.660	1.171	1.400
2.920	1.513	1.739
3.205	1.835	2.056
3.519	2.124	2.332
3.863	2.341	2.531
4.241	2.486	2.659
4.655	2.546	2.704
5.110	2.558	2.701
5.610	2.543	2.667
6.158	2.534	2.632
6.760	2.547	2.613
7.421	2.569	2.597
8.147	2.614	2.599
8.943	2.632	2.577
9.818	2.674	2.576
10.78	2.698	2.562
11.83	2.781	2.605
12.99	2.884	2.672
14.26	3.026	2.774
15.65	3.178	2.884
17.18	3.261	2.927
18.86	3.331	2.955
20.71	3.315	2.910
22.73	3.353	2.925
24.95	3.405	2.968
27.39	3.505	3.071
30.07	3.599	3.179
33.01	3.577	3.186
36.24	3.429	3.079
39.78	3.103	2.810
43.67	2.681	2.462
47.94	2.232	2.105
52.62	1.824	1.806
57.77	1.512	1.613
63.42	1.281	1.501
69.61	1.115	1.440
76.42	0.983	1.377
83.89	0.860	1.276
92.09	0.744	1.132
101.10	0.628	0.951
110.98	0.509	0.749
121.83	0.379	0.539
133.74	0.243	0.338

Diameter (μm)	15R-972 Volume (%)	16R-001 Volume (%)
146.81	0.119	0.165
161.17	0.038	0.055
176.92	0.006	0.009
194.22	0.000	0.001

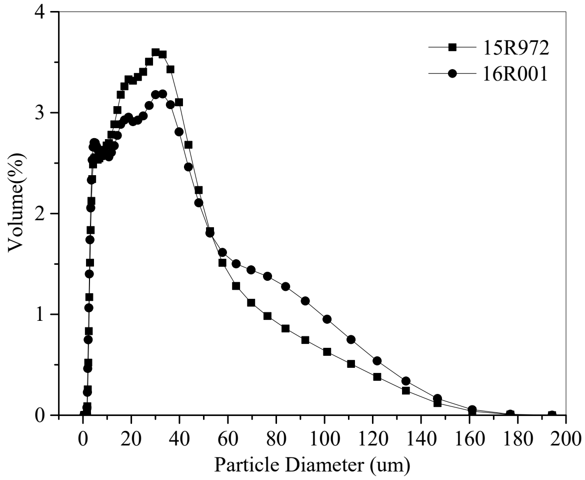

Figure 1.1 Particle distribution curve

At a fixed enamel thickness, small particles can be softened at reduced heat (temperature-time). The exposed surface increases with the decrease of particle size. As the exposed surface increases, the amount of heat (temperature-time) required to soften the particles decreases. The statistical properties of 15R-972 and 16R-001 enamel particles, such as standard deviation, 10%, 50%, and 90% passage diameters (D_{10}, D_{50}, and D_{90}), are compared in Table 1.6. It can be seen from Table 1.6 that the particle size of enamel powder 15R-972 is more uniformly distributed over the entire range of particle sizes. The voids among large particles will be filled by relatively small particles, which may result in a much smoother coating surface on steel samples.

Table 1.6 Volume statistics

	Mean (μm)	Median (μm)	Mode (μm)	S.D. (μm)	$d_{10}(\mu m)$	$d_{50}(\mu m)$	$d_{90}(\mu m)$
15R-972	24.34	16.72	31.50	23.89	4.128	16.72	53.31
16R-001	25.57	15.87	34.58	26.86	3.845	15.87	61.78

2.1.2 Thermal properties

The thermal properties of glasses 15R-972 and 16R-001 such as glass-transition temperature (T_g), softening temperature (T_s), and the coefficient of thermal expansion (CTE) were determined using the Orton automatic recording dilatometer (Model 1500). Three samples of 15R-972 coating were prepared and tested to understand the variation of test data. Since the CTE values of two samples of Glass 16R-001were quite close, the third sample was not prepared. Table 1.7 and Table 1.8 show the general thermal properties of the two glass coatings.

Table 1.7 Thermal property of glass 15R-972

Glass ID	T_g (℃)	T_s (℃)	CTE (200 to 400℃) (ppm/℃)
15R-972(1)	552	616	13.0
15R-972(2)	551	610	12.1
15R-972(3)	553	611	13.8
Average	552	612	13
STDEV	0.8	2.6	0.7

Table 1.8 Thermal property of glass 16R-001

Glass ID	T_g (℃)	T_s (℃)	CTE (200 to 400℃) (ppm/℃)
16R-001(1)	537	602	11.3
16R-001(2)	542	611	10.9
Average	540	607	11.1
STDEV	2	4.5	0.2

Figure 1.2 shows the thermal elongation in the longitudinal direction of the three glass coatings and steel as a function of temperature. The steel has a measured CTE of 19.7 ppm/℃ while the glass coatings 15R-972 and 16R001 have a measured CTE of 13.0±0.7 ppm/℃ and 11.1±0.2 ppm/℃, respectively. The CTE of the steel remains constant over a temperature range of 100 to 600℃, while the CTE of the glass coatings is constant only over a range of 200 to 400℃. The CTE difference between the steel and glass coatings will generate compressive stress on the coatings during cooling, which is desirable. The glasses 15R-972 and 16R-001 have similar thermal properties with $540 \leq T_g \leq 552$°C and $607 \leq T_s \leq 616$°C.

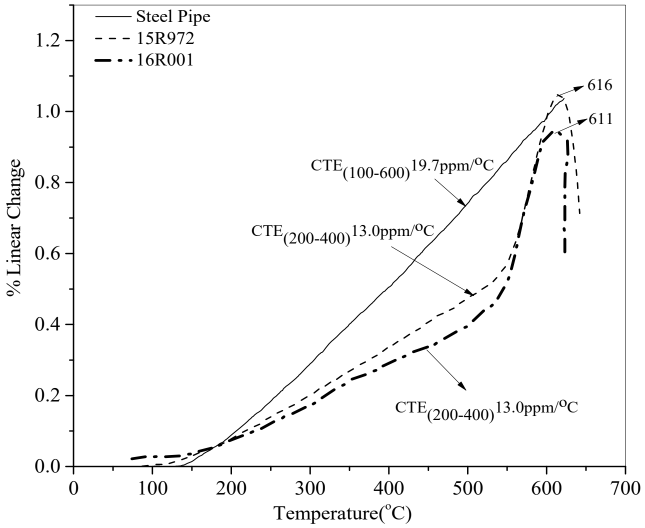

Figure 1.2 Thermal properties of two coatings and steel measured with Orton dilatometer

2.1.3 Coating characterization

The steel coupon samples are coated with two pure enamels (15R-972 and 16R-001), and three mixed enamels. The pure enamels 15R-972 and 16R-001 are designated by PE1 and PE2, respectively. The mixed enamels are designated by ME1, ME2, and ME3, respectively. ME1 was made by mixing 25 wt.% 15R-972 with 75 wt. % 16R-001, ME2 by mixing 50 wt.% 15R-972 with 50 wt.% 16R-001, and ME3 by mixing 75 wt.% 15R-972 with 25 wt.% 16R-001.

Cross-sectional SEM images of five enamel-coated steel samples are presented in Figure 1.3. The thicknesses of enamel coating PE1, PE2, ME1, ME2, and ME3 are approximately 250 µm, 363 µm, 227 µm, 159 µm, and 409 µm, respectively. The air bubbles observed in the enamel coatings were released from the high-temperature chemical reaction of the enamel with the steel substrate during enameling process. All the enamel coatings have many isolated small pores and a few large pores except that coating PE1 does not have any large pore. Enamel coating PE2 has the fewest number of small air bubbles and a few large air bubbles up to 220 µm in diameter, which is almost the same as the thickness of the coating ME2. Mixed enamels ME1, ME2, and ME3 have a few large air bubbles with a diameter of approximately 90 µm.

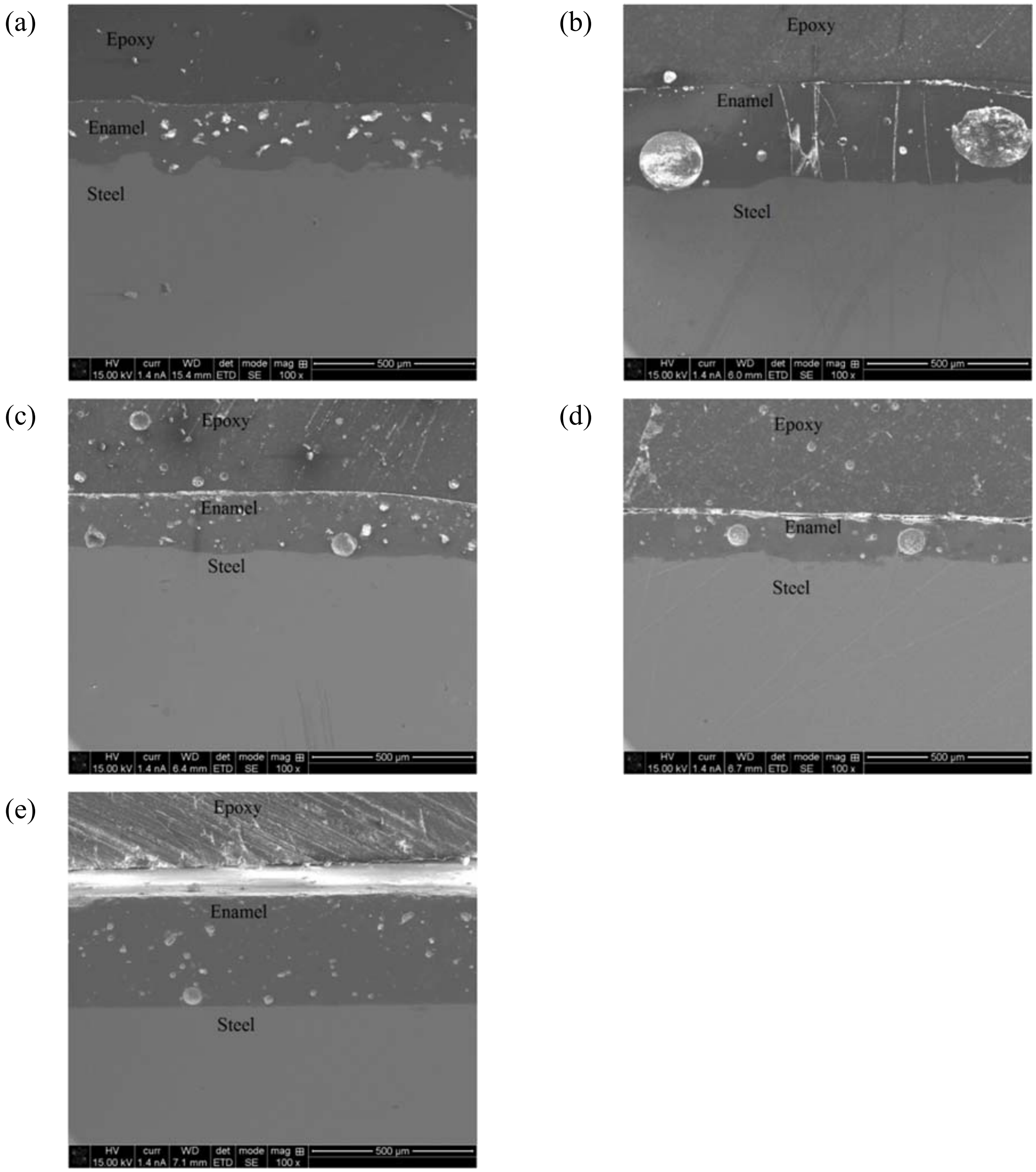

Figure 1.3 SEM images of: (a) PE1-, (b) PE2-, (c) ME1-, (d) ME2-, and (e) ME3-coated steel samples

After corrosion tests, the surface conditions of all samples were examined visually. No corrosion sign was observed on the surface of PE2, ME1, and ME2 coatings. However, some tiny corrosion spots could be seen on the surface of PE1 and ME3 coated samples as shown in Figure 1.4. This is probably due to coating damage/defects, allowing sodium chloride solution to penetrate and react with substrate steel.

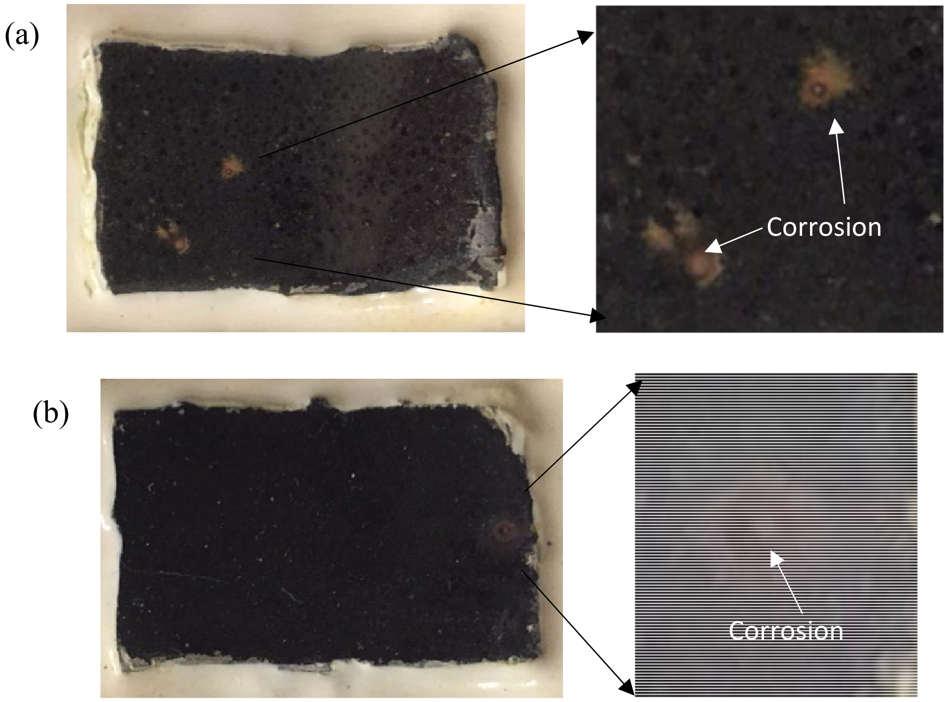

Figure 1.4 Surface conditions of: (a) PE1- and (b) ME3-coated steel samples

2.1.4 Corrosion tests

Figure 1.5 shows a 25 mm × 50 mm corrosion test sample. The uncovered enamel coating area was 20 mm×30 mm with an exposed area of 600 mm^2.

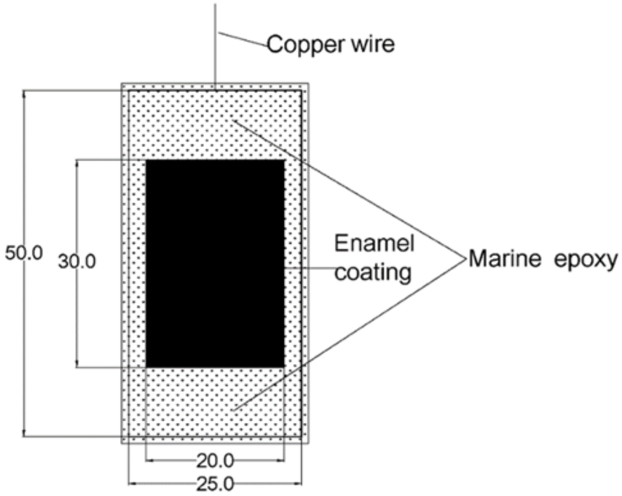

Figure 1.5 Test sample dimension (unit: mm)

2.1.4.1 Linear polarization resistance

The linear polarization resistance curves of enamel-coated and uncoated samples are presented in Figure 1.6. It is noted that the electrical currents in horizontal axis have different units (uA, nA, pA) for various samples, and are not normalized by total surface area of the samples.

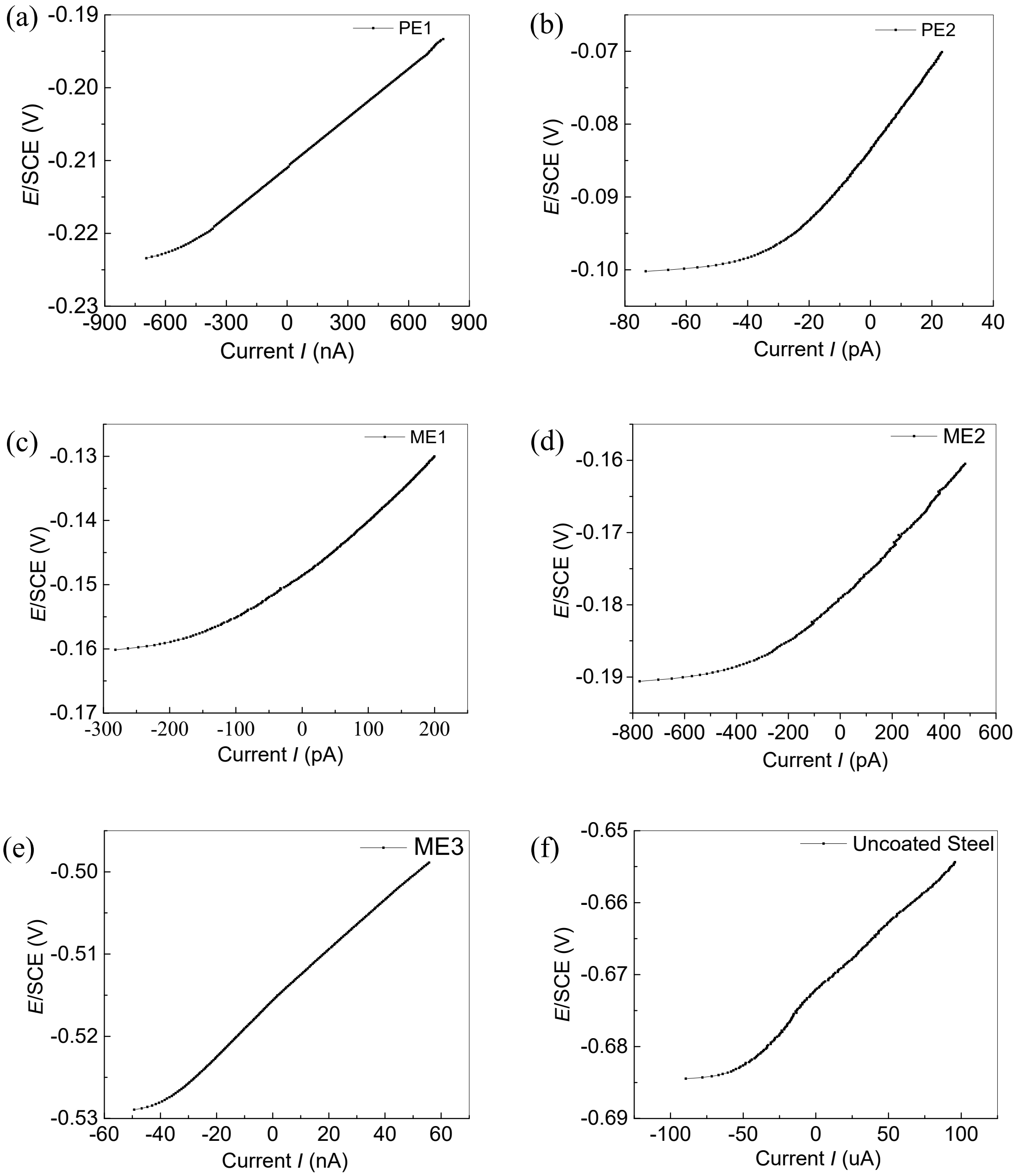

Figure 1.6 Polarization resistances for: (a) PE1-coated, (b) PE2-coated, (c) ME1-coated, (d) ME2-coated, (e) ME3-coated and (f) uncoated steel samples

The polarization resistance R_p is equal to the slope of the linear region of the polarization curve around the zero current [10]:

$$R_p = \Delta E / \Delta I \tag{1-1}$$

in which ΔE and ΔI represent the corresponding potential and current changes at the zero current. The corrosion current density i_{corr} can then be calculated by

$$i_{corr} = B/(AR_p) \tag{1-2}$$

where B is a constant related to the Tafel constants (B=26 mV was used in this study), and A is the exposed sample area. The corrosion current density can be converted into the corrosion rate by

$$Corrosion\ Rate = \frac{i_{corr}M}{\rho n F} \tag{1-3}$$

where M(=55.85 g) is the molar mass of iron, n is the ionic charge (n = 2 for iron), ρ (=7.88 g/cm^3) is the density of iron and F (=96,485 C/mol) is Faraday's constant. The corrosion potential E_{corr} corresponding to zero current in each polarization curve, polarization resistance and corrosion rate of the tested samples are listed in Table 1.9.

Table 1.9 Corrosion potential, polarization resistance and corrosion rates of various samples

	PE1	PE2	ME1	ME2	ME3	Uncoated
Ecorr (V/SEC)	-0.208	-0.085	-0.145	-0.175	-0.513	-0.690
R_p (Ω)	2.17×10^4	8.20×10^8	8.93×10^7	2.34×10^7	3.76×10^5	2.68×10^2
Corrosion Rate (mm/year)	2.15×10^{-4}	8.96×10^{-8}	6.47×10^{-7}	1.46×10^{-6}	1.55×10^{-4}	0.24

The corrosion potential of uncoated steel sample is around -0.69 V/SCE, indicating an active corrosion. This indication is supported by the high corrosion rate with a value of 0.24 mm/year. In comparison with PE1, PE2 has a higher corrosion potential, a higher polarization resistance, and a lower corrosion rate. The corrosion rate of PE2 is almost 10^5 order lower than PE1. The mixed enamels also demonstrated quite different corrosion behaviors. ME1 and ME2 are much better than ME3. The corrosion rate of the ME3 coated sample is 10^2~10^3 higher than those with ME1 and ME2 coatings. The lower corrosion resistances of PE1 and ME3, compared with their peer samples, are probably because of more damage or coating defects present on the PE1 and ME3 coated samples [11]. The coating damage or defects provided pathways for sodium chloride penetration, resulting in reduced corrosion resistance.

Based on the corrosion rates, the corrosion resistances of all the five enamel coatings can be ranked as follows: PE2>ME1>ME2>ME3>PE1. They consistently indicate that the pure enamel 16R-001 is superior to 15R-972. However, all the enamel-coated samples have much lower corrosion rates than the uncoated steel sample, and can thus prevent the steel from corrosion to certain extent.

2.1.4.2 Impedance spectrum

The electrochemical impedance spectra of samples coated with five different enamels and the uncoated sample are presented in the format of Nyquist and Bode plots in Figure 1.7. The Nyquist plot of PE1 coated sample shows two separated semi-circles with a diffusion tail. Only one big semi-circle is observed for PE2, ME1, ME2, and ME3 coated samples. This is likely because the two time constants corresponding to electrochemical reactions at the steel/electrolyte interface and the dielectric properties of enamel coating are overlapped [12]. However, two phase angle maxima in the low and high frequency ranges can be clearly seen from the phase angle-frequency diagrams of PE2, ME1, ME2, and ME3 coated samples, which correspond to the two time constants [13-14]. The uncoated steel sample showed one capacitive loop and one phase angle maxima in the low frequency range. This means only one time constant appears, which corresponds to the electrochemical reactions at the steel/ electrolyte interface. The PE2 coated sample shows up to 5 orders of magnitude higher impedance modulus than PE1 and ME3 coated samples, reaching almost 1 GΩ cm^2. The phase angles at 100 kHz of PE1, PE2, ME1, ME2, and ME3 coated samples are approximately 60°, 90°, 80°, 60°, and 40°, respectively. The higher phase angle of approximately 90° means that the enamel coating can provide good corrosion protection, and the lower phase angle indicates that the electrolyte has a large potential to penetrate through the coating, which will increase the coating capacitance [15]. All the enamel coated samples have much higher impedance values than the uncoated steel.

(a-1)

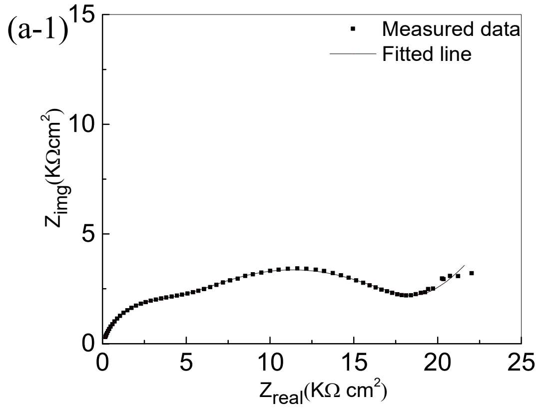

(a-2)

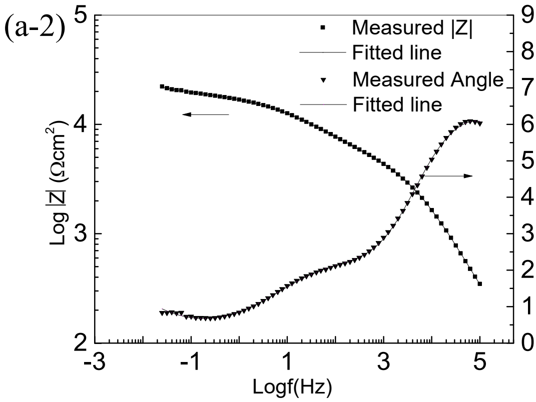

(b-1)

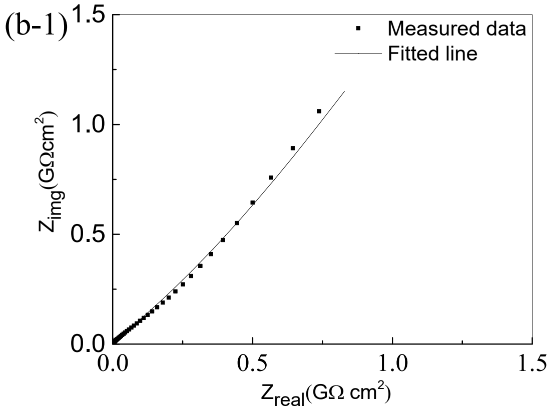

(b-2)

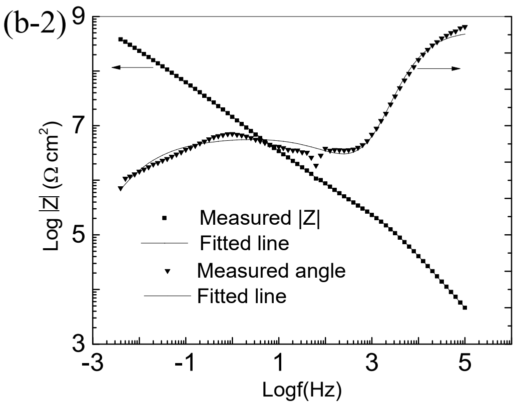

(c-1)

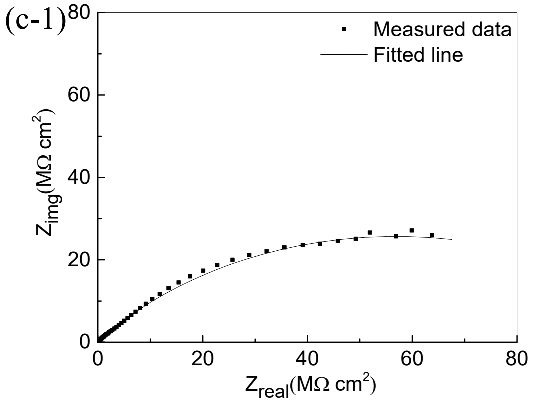

(c-2)

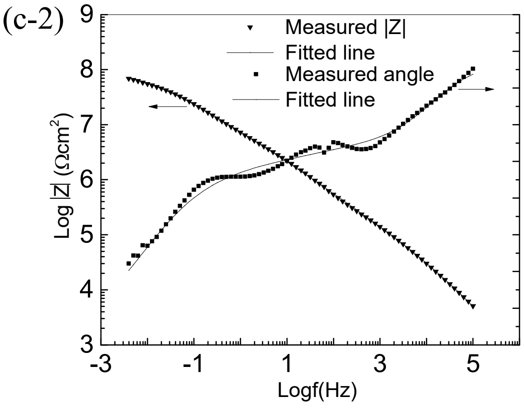

(d-1)

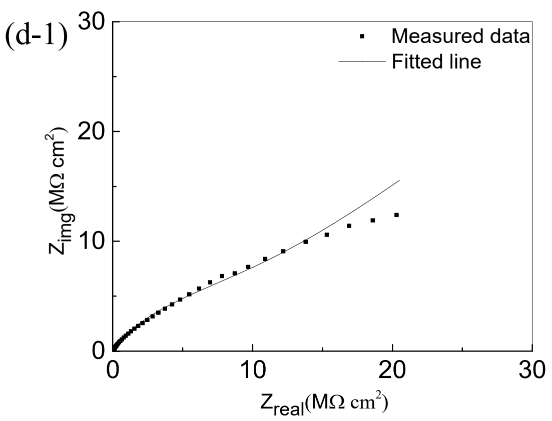

(d-2)

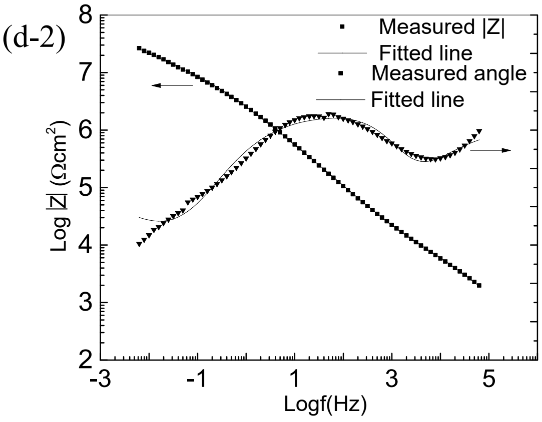

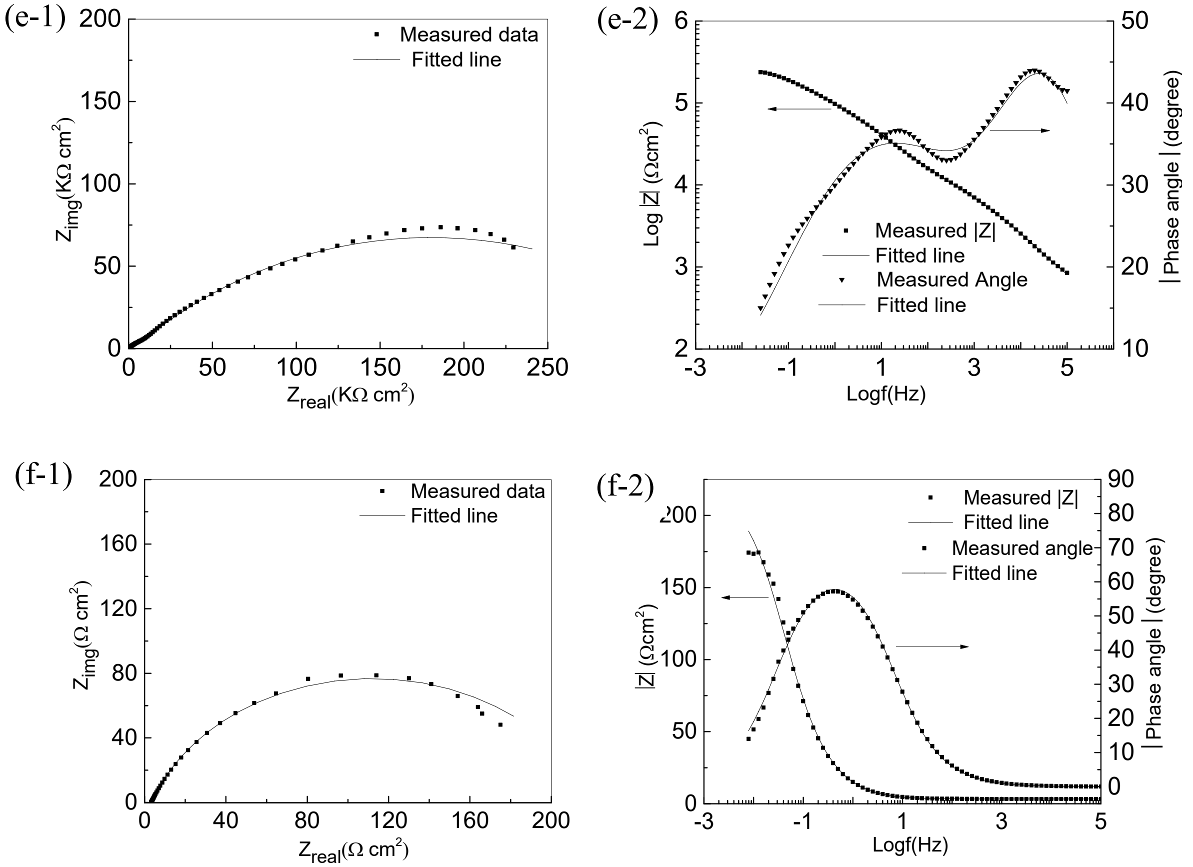

Figure 1.7 EIS diagrams (1: Nyquist plot; 2: Bode plot) for: (a) PE1-coated, (b) PE2-coated, (c) ME1-coated, (d) ME2-coated, (e) ME3-coated, and (f) uncoated steel samples

Three electrical equivalent circuit (EEC) models are chosen to fit the experimental data. In the EIS diagrams shown in Figure 1.7, the dotted points are the experimental data and the solid lines represent curve fitting by EEC models. The Warburg impedance *W* is included in model (c) to simulate the diffusion behavior, which is caused by the accumulation of corrosion products at sites with coating damage or defects. The three EEC models are illustrated in Figure 1.8. Model (a), model (b) and model (c) were used to simulate the uncoated sample; PE2-, ME1-, and ME3-coated samples; and PE1- and ME2-coated samples, respectively. The difference between model (b) and model (c) is the diffusion impedance, which is associated with the oxygen diffusion through corrosion products. As mentioned before, some damage/defects may be present on the coatings, which would form pathways for penetration of sodium chloride solution. Once the solution penetrated through these pathways to the substrate steel surface, corrosion would occur and corrosion products would be generated. The corrosion products would accumulate at these damage/defect sites, and consequently oxygen needed for the corrosion reaction had to diffuse through these corrosion products to participate in the corrosion reaction at the exposed steel surface.

Specifically, in these models, R_s represents the solution resistance, CPE_c represents the coating capacitance, R_c represents the coating resistance, CPE_{dl} represents the double layer capacitance, and R_{ct} represents the charge transfer resistance. CPE_c is used to replace a pure capacitance because of non-homogeneity in thickness and roughness of the coating [16, 17]. CPE_{dl} represents a certain deviation extent from the pure capacitance due to the distribution of reactivity [18]. A CPE is defined by two parameters Y and n, and its impedance is represented by:

$$Z_{CPE} = Y^{-1}(jw)^{-n} \tag{1-4}$$

where $Y$is a parameter with unit of $\Omega\text{-}sec^n/cm^2$, which is proportional to the pure capacitance, ω is the angular frequency in $rad\ s^{-1}$, and n is an index that represents the deviation from a pure capacitor [9]. For n =1, CPE resembles a pure capacitor with capacitance Y. For n=0, CPE represents a resistor with resistance Y^{-1}. The effective capacitance based on the CPE parameters can be obtained by [19, 20]:

$$C = Y^{1/n}R^{(1-n)/n} \tag{1-5}$$

where parameters R_c, Y_c, n_c are used to calculate the effective capacitance of enamel coatings C_c; R_{ct}, Y_{dl}, n_{dl} are used to calculate the effective capacitance of double layer C_{dl}.

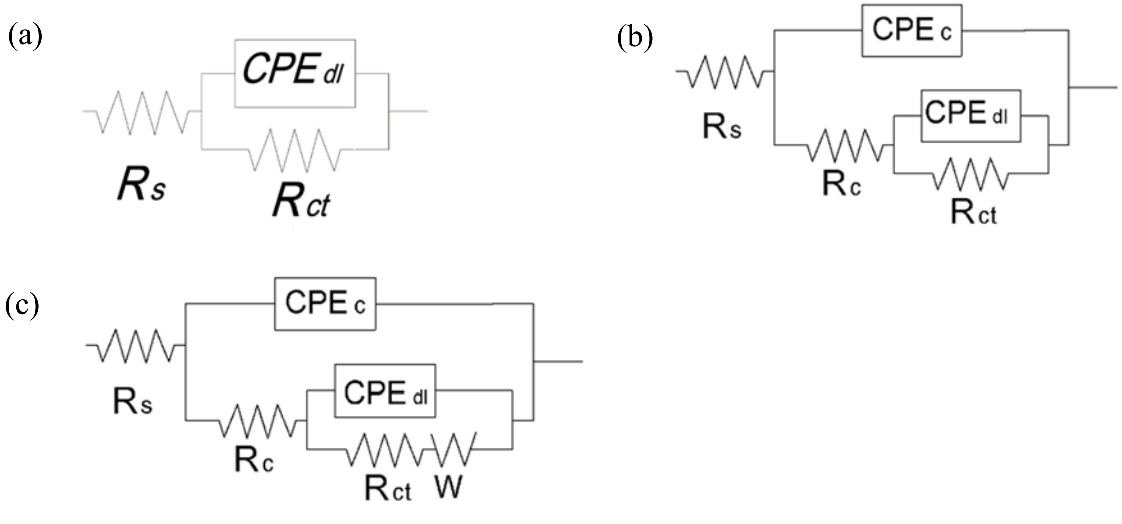

Figure 1.8 EEC models for: (a) uncoated-; (b) PE2-coated, ME1-coated, and ME3-coated; and (c) PE1-coated, and ME2-coated samples

ZSimpWin was used to fit the two EEC models into EIS data as shown in Figure 1.7. The chi-squared values are in the order of 10^{-4} to 10^{-3}, indicating a satisfactory fitting process. The parameters obtained from the fitted EEC models are listed in Table 1.10.

Table 1.10 EEC parameters obtained by fitting into experimental data

	Y_c (Ω-sec^n/cm^2)	n_c	R_c ($\Omega\ cm^2$)	C_c ($F\ /cm^2$)	Y_{dl} (Ω-sec^n/cm^2)	n_{dl}	R_{ct} ($\Omega\ cm^2$)	C_{dl} ($F\ /cm^2$)
PE1	9.44×10^{-8}	0.78	4.24×10^{3}	9.74×10^{-9}	7.65×10^{-6}	0.49	1.51×10^{4}	7.95×10^{-7}
PE2	6.10×10^{-10}	0.96	2.72×10^{5}	3.89×10^{-10}	2.09×10^{-8}	0.62	1.35×10^{9}	1.62×10^{-7}
ME1	2.05×10^{-9}	0.86	6.27×10^{4}	4.65×10^{-10}	4.55×10^{-8}	0.53	1.14×10^{8}	1.93×10^{-7}
ME2	8.64×10^{-8}	0.67	3.06×10^{4}	1.47×10^{-8}	1.25×10^{-8}	0.84	1.35×10^{7}	8.00×10^{-9}
ME3	2.61×10^{-7}	0.65	7.31×10^{3}	8.72×10^{-9}	3.44×10^{-6}	0.45	3.51×10^{5}	3.60×10^{-6}
Uncoated	-	-	-	-	1.71×10^{-2}	0.78	217	0.025

In general, the coating resistance measures the barrier performance of a coating against electrolyte penetration and the coating capacitance indicates the diffusion of electrolyte solution into the coating. Both parameters are closely related to the dielectric property, microstructure, thickness, and defect of the coating itself. The PE2 coating has the highest coating resistance and the lowest capacitance, which means higher electrolyte penetrating resistance and lower electrolyte diffusion into coating, respectively. The PE1 coating and ME3 coating have the lowest coating resistance and relatively higher coating capacitance, which provide the least protection from chloride attack.

The charge transfer resistance measures the ease of electron transfer across the metal surface, which is inversely proportional to corrosion rate [21]. The uncoated steel sample has the lowest charge transfer resistance (217 Ω cm^2) and the highest double layer capacitance (0.025 F/cm^2). The PE2 coating has the highest charge transfer resistance (1.35×10^9 Ω cm^2), which is five orders of magnitude larger than that of coating PE1, and quite close to the R_p from linear polarization resistance test. The double layer capacitance C_{dl}, calculated from Eq. (5), is also a measure of ease of charge transfer. The lower double layer capacitance values of coatings PE2, ME1 and ME2 indicate better corrosion performance compared with coatings PE1 and ME3. The higher charge transfer resistance and the lower double layer capacitance of coating PE2 show better resistance to the transfer of electrons across the metal surface [22]. The index n_c of coating PE2 is 0.957, which means the coating is quite close to a pure capacitor. However, the index n_c of coating ME3 (=0.648) is the smallest, indicating the great non-homogeneity property of this coating. The corrosion resistance ranking for all five enamel coatings obtained from the EIS results is consistent with that from the LPR tests.

2.1.5 Conclusions

Based on the experimental results and analysis, the following conclusion can be drawn:

1. The tested enamel coatings vary from 160 to 410 μm thick, containing numerous isolated small pores and large air bubbles that were generated during the enameling process.
2. The LPR test results are consistent with the EIS results. The corrosion rates of the steel samples coated with PE1 and ME3 are 2.15×10^{-4} mm/year and 1.55×10^{-4} mm/year, respectively, which are higher than those of the samples with PE2, ME1, and ME2 coatings. The EIS results also show that PE1 and ME3 have lower coating resistance and higher coating capacitance, as well as lower charge transfer resistance and higher double layer capacitance in sodium chloride solution than the rest enamel coatings.
3. All five enamel coatings increase the corrosion resistance of pipeline steel. Their corrosion resistances are ranked by PE2 > ME1 > ME2 > ME3 > PE1. The poor corrosion resistance of PE1 and ME3 coatings are most likely attributed to coating damage and defects, which provides pathways for electrolyte penetration.

2.2 Enamel Tomatec and GP2118

2.2.1 Thermal properties

The thermal properties of glasses Tomatec (slurry) and GP2118 (powder) such as glass-transition temperature (T_g), softening temperature (T_s), and the coefficient of thermal expansion (CTE) were determined using the Orton automatic recording dilatometer (Model 1500). Three samples were prepared for each coating and tested to understand the variation of test data. The samples of glass enamel were prepared by melting glass powder in alumina crucibles in air at 1250 °C for 1 h. The melted sample was quenched in air by pouring it into a $1 \times 1 \times 5$ cm^3 steel mold. The samples were transferred into a furnace and annealed at 450 °C for 4 h. Dilatometric analysis measurements were then performed in flowing synthetic air at a heating rate of 10 °C/min.

Figure 1.9 shows the thermal elongation in the longitudinal direction of the two glass coatings and steel as a function of temperature. The steel has a measured CTE of 19.7 ppm/$℃$ while the glass coatings Tomatec slurry and GP2118 powder have a measured CTE of 13.0 ppm/$℃$ and 10.9

ppm/°C, respectively. The CTE of the steel remains constant over a temperature range of 100 to 600°C, while the CTE of the glass coatings is constant only over a range of 200 to 400°C. The CTE difference between the steel and glass coatings will generate compressive stress on the coatings during cooling, which is desirable. The glasses Tomatec and GP2118 have similar thermal properties with $506 \leq T_g \leq 552$°C and $578 \leq T_s \leq 616$°C.

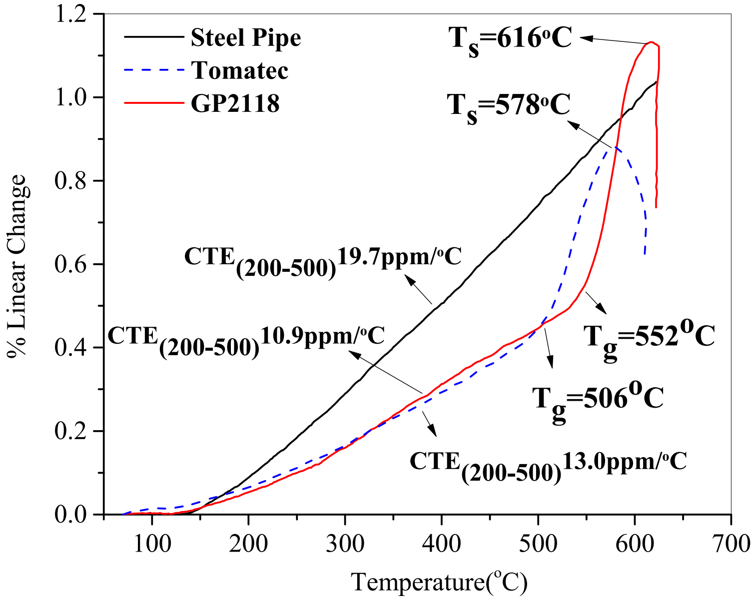

Figure 1.9 Thermal properties of two coatings and steel measured with Orton dilatometer

2.2.2 Coating characterization

Cross-sectional SEM images and representative EDS analyses of enamel-coated steel samples are presented in Figure 1.10. EDS analyses were performed on the coating sample taken within the small white square in the respective SEM images. Powder enamel (GP2118) coating (P series) of approximately 180 μm in thickness as shown in Figure 1.10(a-1) has an amorphous structure with a few isolated air bubbles corresponding to a porosity of 3.51%. The largest air bubble is 41 μm in diameter. The magnified interface layer as shown in Figure 1.10(a-2) shows the extensive formation of an island-like structure in the enamel coating, reinforcing interfacial bond [**23**]. EDS analysis as shown in Figure 1.10(a-3) indicates that the principal components in the coating include silicon (Si), sodium (Na), manganese (Mn), potassium (K), calcium (Ca), iron (Fe), titanium (Ti), and aluminum (Al). Boron, a major component of the glass frit, could not be detected by the EDS system used due to its lightweight nature.

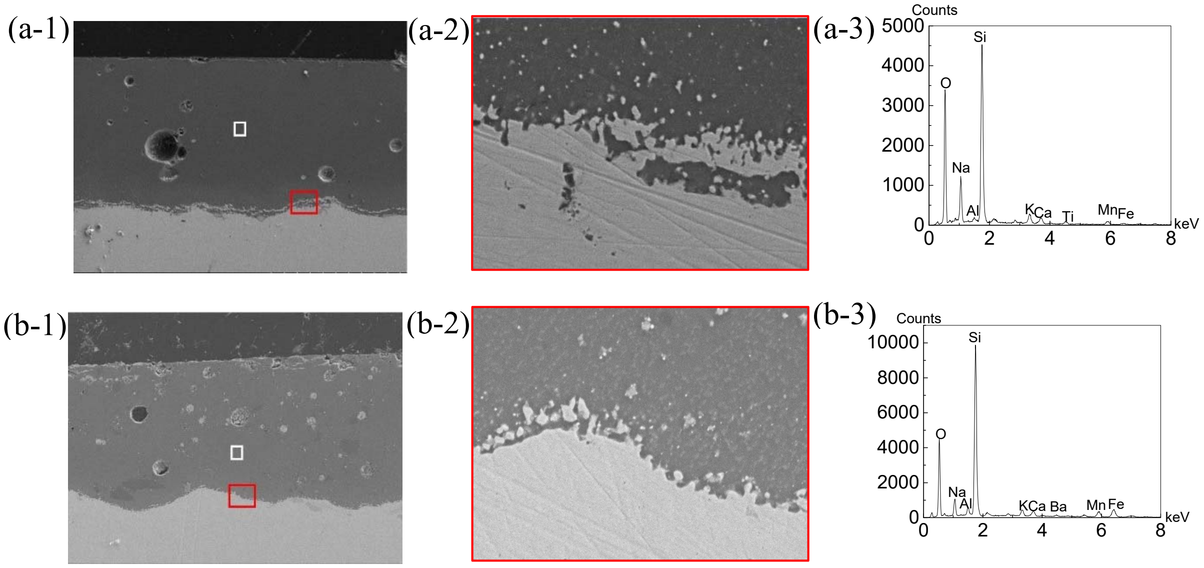

Figure 1.10 Cross-sectional SEM images and EDS analysis of (a-1, a-2, a-3) powder enamel-coated sample and (b-1, b-2, b-3) slurry enamel-coated sample before corrosion tests with different magnifications: (a-1) 250×, (a-2) 2500×, (b-1) 250× and (b-2) 2500×

The slurry enamel (Tomatec) coating (S series) as shown in Figure 1.10(b-1) is approximately 235 μm thick and has a porosity of 6.57%. It has more, but smaller air bubbles than the powder enamel coating. Figure 1.10(b-2) also shows anchor points growing into the coating, indicating strong chemical bond at the enamel-steel interface. EDS analysis in Figure 1.10(b-3) indicates that silicon (Si), sodium (Na), manganese (Mn), aluminum (Al), iron (Fe), calcium (Ca), potassium (K), and barium (Ba) are the detected principal components. Once again, EDS analysis could not detect boron.

The air bubbles in the coating were formed in the enameling process by entrapped gases such as H_2, CO, and CO_2. During the firing process, the dissolved oxygen reacted with carbons in the steel, releasing gaseous CO/CO_2. The atomic hydrogen diffused into the steel to form hydrogen gas (H_2). In the cooling process, the gas H_2, CO, and CO_2 were no longer able to escape since the gases were entrapped in the solidified enamel [23-24].

2.2.3 Corrosion tests

2.2.3.1 OCP Tests

The OCP represents the potential between the working electrode and the reference electrode when no external potential is applied to the test system. Figure 1.11 presents the OCPs of uncoated, enamel- and epoxy-coated steel samples after one hour of immersion. The variation in OCP among the three identical uncoated samples is much smaller than that of the enamel- and epoxy-coated samples. The average OCP of three uncoated steel samples shows a gradually decreasing trend from the beginning of -0.39 V to the end of -0.48 V. The average OCPs of the powder and slurry enamel-coated samples increase rapidly in the first 500 seconds due to the capacitive charging of enamel coating and then slowly approach to an asymptotical value of 0.88 V and 0.4 V, respectively. The OCP changing trend of three epoxy-coated samples are inconsistent. However, the OCP of each sample after one hour of immersion remains positive with an average value of 0.2 V. Compared with the uncoated steel samples, the higher positive OCP values of enamel- and epoxy-coated samples imply a superior barrier effect to the penetration of electrolyte through the open pores or localized defects. Thus, the coated samples can prevent the electrolyte from being in contact with the substrate steel.

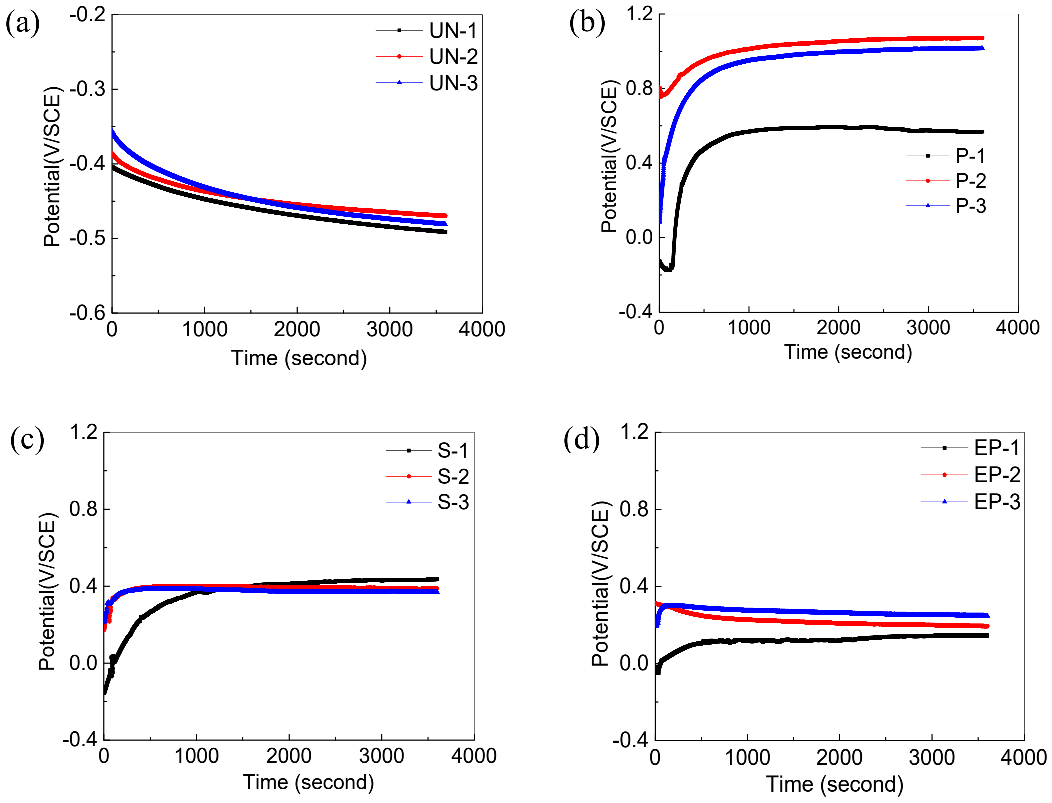

Figure 1.11 The OCPs of various samples in 3.5 wt.% NaCl solution: (a) uncoated, (b) powder enamel-coated, (c) slurry enamel-coated (d) epoxy-coated steel samples

2.2.3.2 EIS Tests

The electrochemical impedances of uncoated, enamel- and epoxy-coated samples are presented in the format of Bode plots in Figure 1.12. In the Bode diagrams, the impedances and phase angles among the three identical samples with each coating are quite consistent. The impedance diagrams of enamel- and epoxy-coated samples show a 45° slope in a log-log scale while those of the uncoated samples start with a slope of larger than 45° at low frequency and gradually decrease to 0° at high frequency. The impedances of all the enamel- and epoxy-coated samples at a frequency of 0.005 Hz are approximately 4×10^{10} Ω cm^2. Although relatively low due to potential coating defects, the impedances are 10^9 times higher than those of the uncoated samples. In addition, the phase angles of the enamel- and epoxy-coated samples approach to 90° at high frequency while those of the uncoated samples are close to 0°. The phase angle diagrams confirm that both the enamel and epoxy coatings provide high resistances to the penetration of electrolyte and thus satisfactory corrosion protection [15].

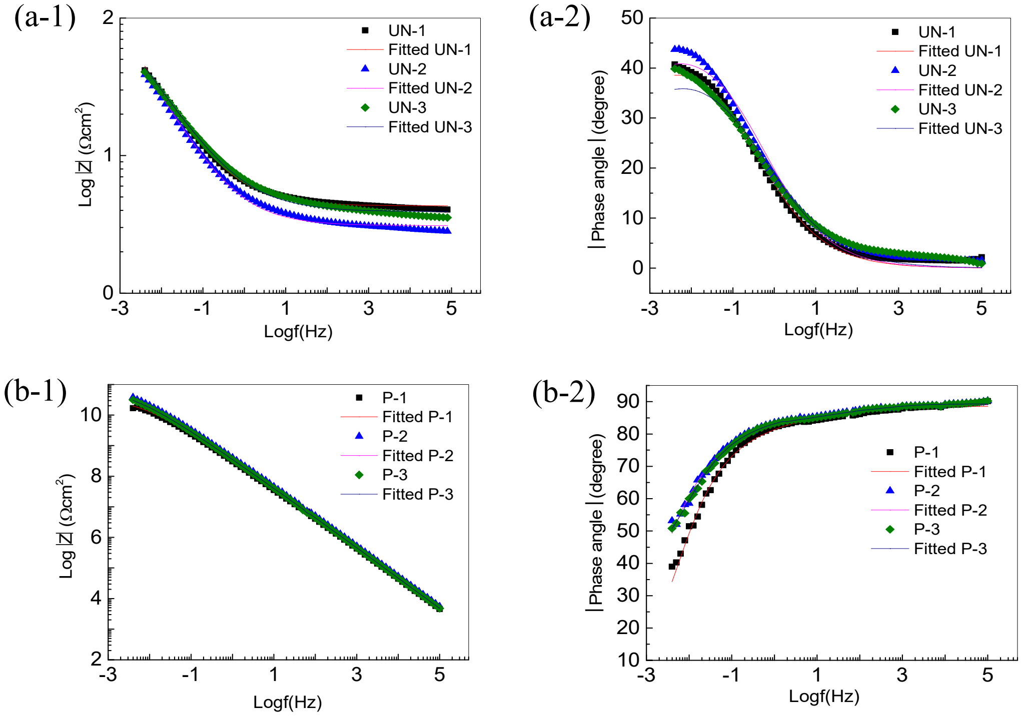

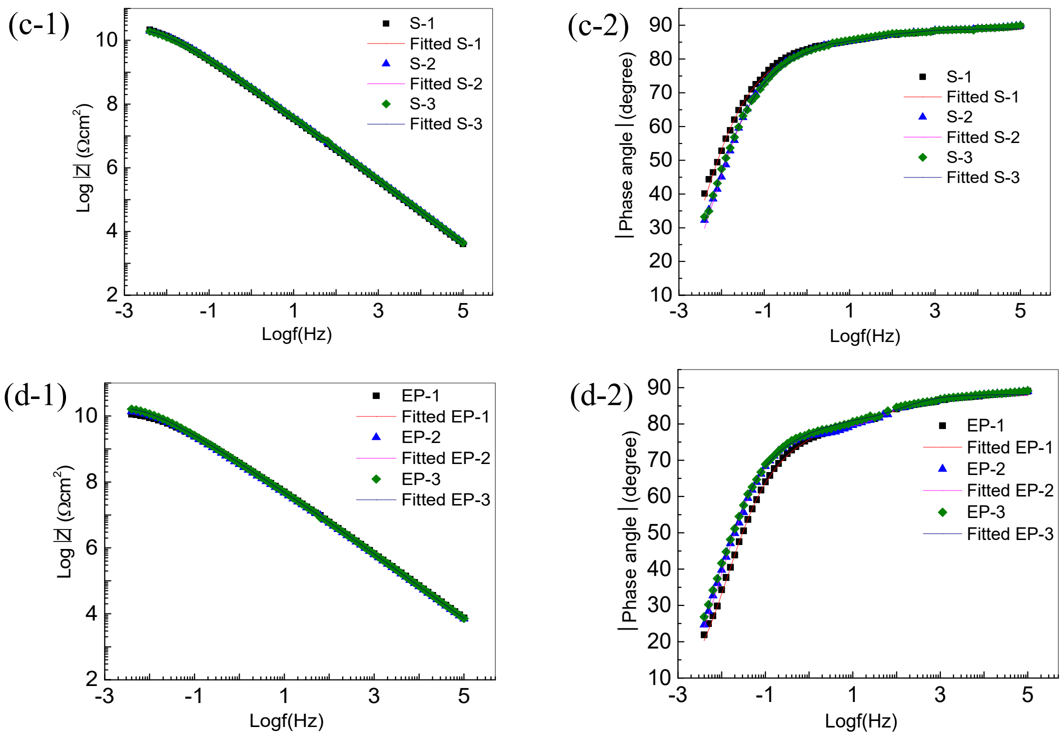

Figure 1.12 EIS diagrams (1 and 2: Bode plot) for: (a) uncoated, (b) powder enamel-coated, (c) slurry enamel-coated (d) epoxy-coated steel samples

Two EEC models were chosen to fit the experimental data [25] as illustrated in Figure 1.13. Models (a) and (b) were used to simulate the uncoated and coated samples, respectively. In the two models, R_s represents the solution resistance, R_c and R_{ct} represent the pore resistance of coating and the charge transfer resistance at the steel-electrolyte interface, respectively, and CPE_c and CPE_{dl} represent the contribution of coating capacitance and double layer capacitance to the total impedance, respectively.

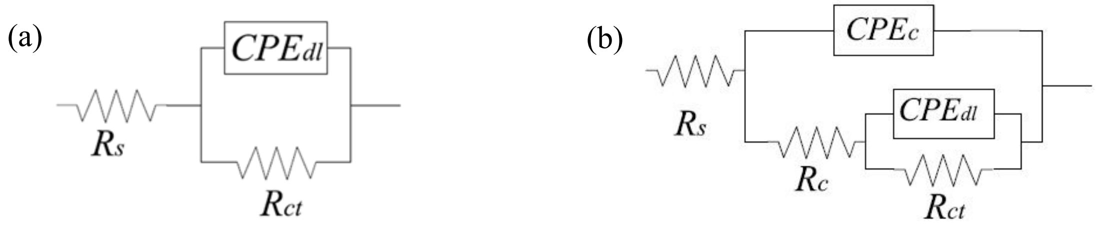

Figure 1.13 EEC models for: (a) uncoated, (b) powder enamel-coated, slurry enamel-coated and epoxy-coated samples

For the uncoated samples, there is only one time constant corresponding to the electrochemical reaction at the steel-electrolyte interface. For the enamel- and epoxy-coated samples, there are indeed two time constants, which correspond to the electrochemical reaction at the steel-electrolyte interface and the dielectric properties of coatings [26]. In the Bode plots, the two time constants are not easily identifiable since they are overlapped [27].

ZSimpWin was used to determine the parameters of two EEC models based on the EIS data recorded. The chi-squared values were in the order of 10^{-4} to 10^{-3} for all the samples, indicating a satisfactory fitting of the two proposed EEC models. The parameters obtained from curve fitting are listed in Table 1.11.

Table 1.11 EEC parameters obtained by fitting into experimental data

	Y_c (Ω-sec^n/cm^2)	n_c	R_c ($\Omega\ cm^2$)	C_c ($F\ /cm^2$)	Y_{dl} (Ω-sec^n/cm^2)	n_{dl}	R_{ct} ($\Omega\ cm^2$)	C_{dl} ($F\ /cm^2$)
P-1	4.26×10^{-10}	0.98	2.56×10^{7}	3.96×10^{-10}	2.24×10^{-10}	0.65	3.22×10^{10}	6.57×10^{-10}
P-2	3.38×10^{-10}	0.99	4.72×10^{7}	3.22×10^{-10}	1.38×10^{-10}	0.63	4.84×10^{10}	4.24×10^{-10}
P-3	3.71×10^{-10}	0.99	2.71×10^{7}	3.57×10^{-10}	1.70×10^{-10}	0.69	4.44×10^{10}	4.23×10^{-10}
S-1	4.58×10^{-10}	0.99	4.37×10^{7}	4.36×10^{-10}	2.01×10^{-10}	0.64	3.99×10^{10}	6.43×10^{-10}
S-2	4.21×10^{-10}	0.99	3.40×10^{7}	4.00×10^{-10}	2.06×10^{-10}	0.63	2.94×10^{10}	5.80×10^{-10}
S-3	4.06×10^{-10}	0.99	3.54×10^{7}	3.84×10^{-10}	1.88×10^{-10}	0.64	2.87×10^{10}	4.87×10^{-10}
EP-1	2.84×10^{-10}	0.98	3.42×10^{7}	2.56×10^{-10}	3.09×10^{-10}	0.67	1.46×10^{10}	6.40×10^{-10}
EP-2	3.12×10^{-10}	0.98	6.39×10^{7}	2.83×10^{-10}	3.11×10^{-10}	0.71	1.83×10^{10}	6.29×10^{-10}
EP-3	2.91×10^{-10}	0.98	3.78×10^{7}	2.64×10^{-10}	2.79×10^{-10}	0.69	2.26×10^{10}	6.34×10^{-10}
UN-1	-	-	-	-	0.15	0.52	386	6.54
UN-2	-	-	-	-	0.17	0.53	422	7.31
UN-3	-	-	-	-	0.13	0.49	337	7.56

In general, the pore resistance represents the ability of coating to resist the penetration of electrolyte solution while the coating capacitance indicates the ease of electrolyte diffusion into the coating. Both parameters are closely related to the dielectric property and microstructure of the coating [9, 15]. As shown in Table 1.11, the pore resistances of all the enamel- and epoxy-coated samples are between 10^7 and 10^8 Ω cm^2. The coating capacitances for all the enamel- and epoxy-coated samples range from 10^{-10} to 10^{-9} F/cm^2. The large pore resistance and small coating capacitance indicate that both the enamel and epoxy coatings are strong barriers against the penetration and diffusion of electrolyte. The index n_c of all the coatings are close to 1, which means that the coatings behave like pure capacitors.

The corrosion rate at the metal surface is inversely proportional to the charge transfer resistance (R_{ct}) of the metal sample, which is an indication of how easy electrons can transfer across the metal surface [15, 28]. Among all the samples tested, the uncoated steel samples have the lowest charge transfer resistance of 381±42 Ω cm^2. The charge transfer resistances of all the coated samples range from 10^{10} to 10^{11} Ω cm^2, which is approximately 10^8 times larger than those of the uncoated samples. The double layer capacitance (C_{dl}) is also a measure of the ease of charge transfer across the interface between the substrate steel and electrolyte. The double layer capacitances of all the coated samples (10^{-10} - 10^{-9} F/cm^2) are approximately 10^{10} times smaller than those (7.14±0.53 F/cm^2) of the uncoated samples. The substantially higher charge transfer resistance and lower double layer capacitance of the enamel- and epoxy-coated samples clearly demonstrate their superior performance in resisting the transfer of electrons across the metal surface.

2.2.3.3 PP Tests

Potentiodynamic polarization (PP) plots of the uncoated, enamel-coated and epoxy-coated samples immersed in 3.5 wt.% NaCl solution are presented in Figure 1.14 to illustrate the overall kinetics of the corrosion process. It can be seen from Figure1.14 that the anodic portion of polarization curves for all the samples tested show the same changing trend although some fluctuations can be observed from the uncoated steel samples. The fluctuations are likely because the existing rusts or corrosion products formed on the surface of uncoated steel samples affect the diffusion of oxygen and water molecule [29].

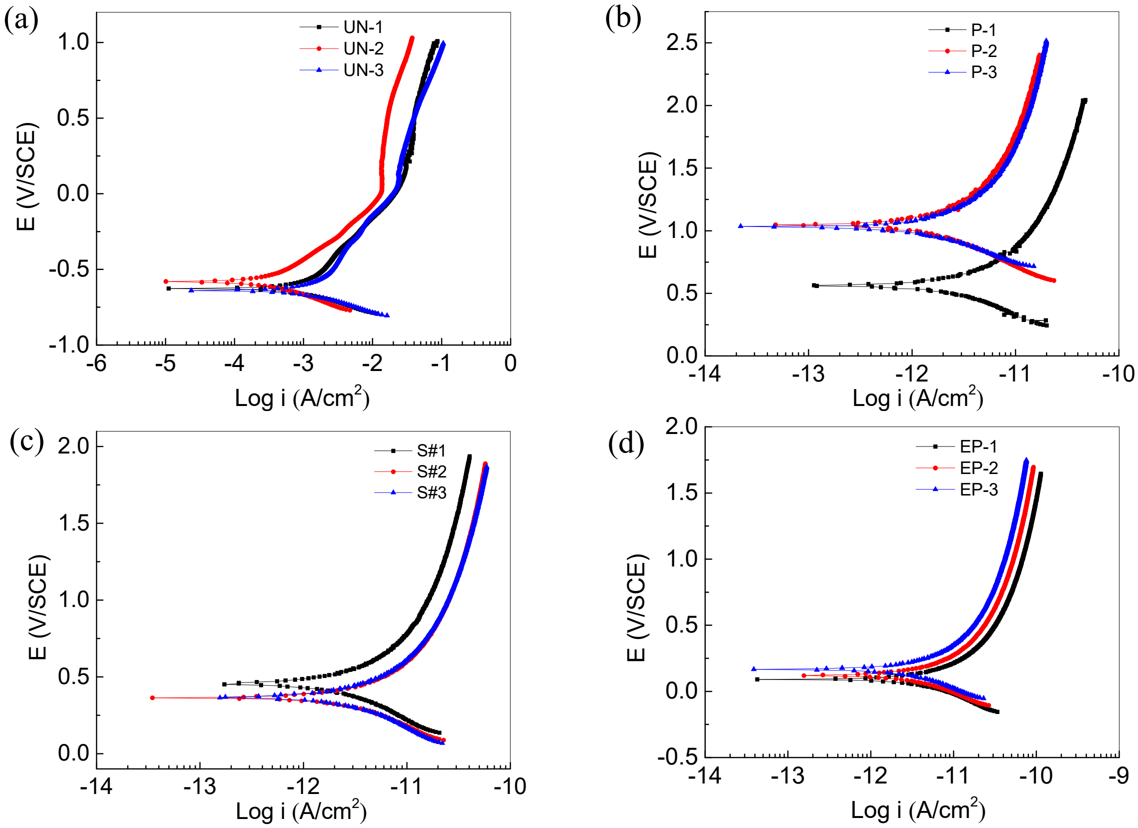

Figure 1.14 Potentiodynamic polarization curves for: (a) uncoated, (b) powder enamel-coated, (c) slurry enamel-coated and (d) epoxy-coated steel samples

The corrosion potential (E_{corr}) and corrosion current density derived from the potentiodynamic polarization plots are presented in Figure 1.15(a-c). These bar charts show the average plus/minus one standard deviation of each electrochemical parameter from the tests of three identical samples. The corrosion potentials of all the enamel- and epoxy-coated samples are positive with the highest value of 0.88 V for the powder enamel coating while those of the uncoated samples are negative with an average value of -0.62 V. The corrosion potentials of powder and slurry enamel-coated samples as shown in Figure 1.15(a) are consistent with the OCPs as displayed in Figure 1.11. The corrosion potentials of the uncoated and epoxy-coated samples are smaller than their OCPs. The uncoated and epoxy-coated samples are thus more susceptible to the disturbance of charging currents than the enamel-coated samples. This is because the changing polarization leads to a continuous variation of the charging current density stored at the substrate-electrolyte interface and the potentiodynamic polarization curve is easily distorted around the corrosion potential where the charging current is hard to be separated directly from the small faradaic current [30]. The average corrosion currents of all the enamel- and epoxy-coated samples are around 10^{-12} A, which are about 10^{9} times smaller than that of the uncoated samples. Thus, all the coatings can protect the substrate metal from corrosion.

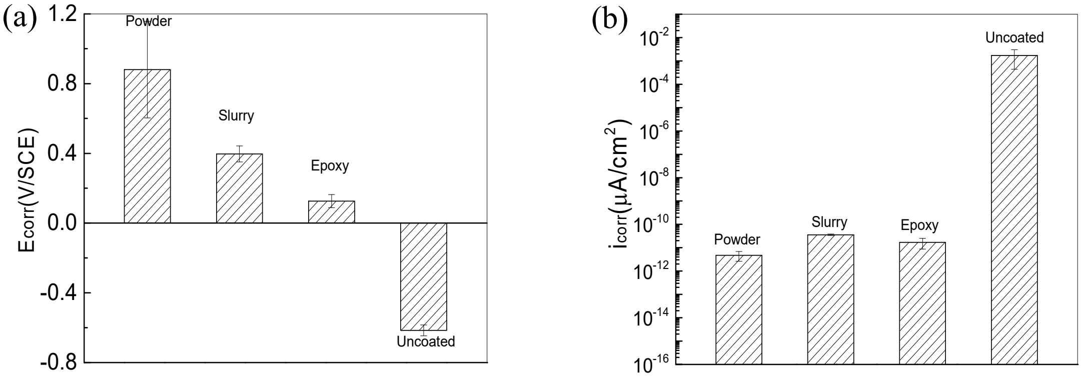

Figure 1.15 Electrochemical parameters extracted from potentiodynamic polarization curves: (a) corrosion potential, (b) corrosion current density

2.2.4 Coating characterization after corrosion tests

Cross-sectional SEM images and representative EDS analyses of enamel-coated steel samples after corrosion tests are presented in Figure 1.16. Compared with the SEM images and EDS analyses before corrosion tests in Figure. 1.10, the coating microstructure, bonding interface between the coating and steel, and principal components remain basically the same in powder and slurry enamel coatings. The sodium content changes little and chloride is not detected by EDS analyses. Therefore, the electrolyte did not penetrate through the coatings during corrosion tests, and the enamel coatings are effective barriers to protect substrate steel from corrosion.

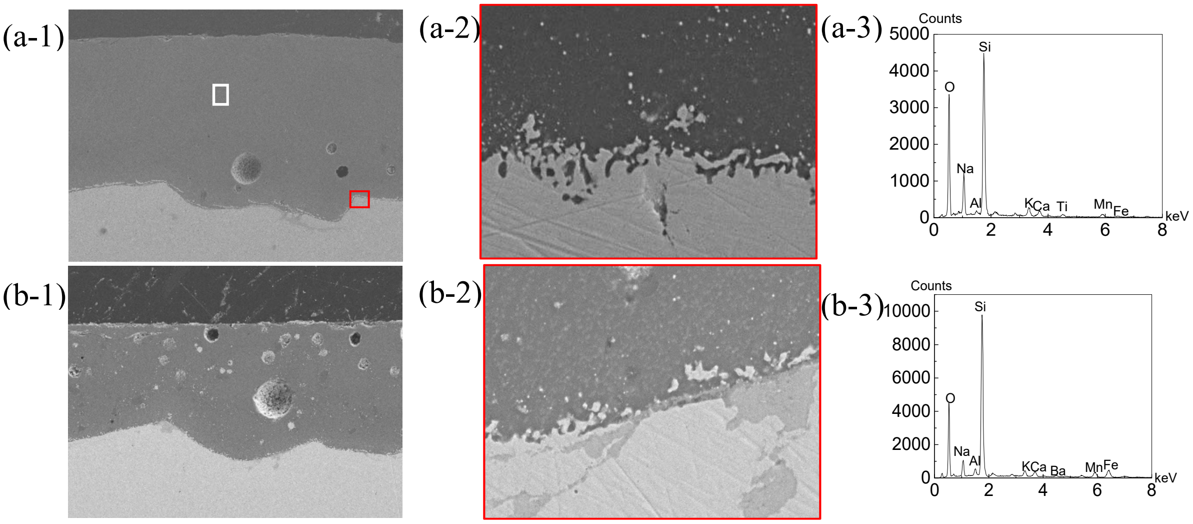

Figure 1.16 Cross-sectional SEM images and EDS analysis of (a-1, a-2, a-3) powder enamel-coated sample and (b-1, b-2, b-3) slurry enamel-coated sample after corrosion tests with different magnifications: (a-1) 250×, (a-2) 2500×, (b-1) 250× and (b-2) 2500×

2.2.5 Conclusions

Based on the experimental results and analysis, the following conclusions can be drawn:

1. The thicknesses of powder and slurry enamel coatings are 180 μm and 235 μm, corresponding to a porosity content of 3.51% and 6.57%, respectively. The powder enamel coating contains fewer but larger isolated air bubbles than the slurry enamel coating. Both coatings cope with small iron protrusions very well, which ensure strong bonding between the coatings and their substrate steel.
2. The open circuit potentials of three uncoated steel samples decreased to an average value of -0.48 V after 1 hour of immersion in 3.5wt.% NaCl solution while those of the enamel- and epoxy-coated samples are positive. This comparison implies that both the enamel and epoxy coatings behave like a barrier for corrosion protection.
3. EIS tests showed that the impedances of both enamel- and epoxy-coated samples at a low frequency of 5 mHz were approximately 10 GΩ cm^2, and the phase angles at high

frequency approached to 90°. These results demonstrate that these coatings provided excellent corrosion protection for the substrate steel.

4. Potentiodynamic polarization tests showed that all the enamel- and epoxy-coated samples had a positive corrosion potential and a significantly lower corrosion current than the uncoated samples.
5. Comparison of the SEM images and EDS analyses of two enamel-coated steel samples before and after corrosion tests shows nearly the same coating microstructure and the same enamel-steel interface with no presence of chloride. Therefore, the electrolyte did not penetrate through either the powder or slurry enamel coating during corrosion tests, both effectively protecting substrate steel from corrosion.
6. The powder enamel coating applied through the electrostatic spray process has a smoother surface and higher corrosion resistance than the slurry enamel coating. In addition, the electrostatic process requires less coating time and is thus a practical solution in pipeline field applications. Due to their superior performance, the Tomatec and GP2118 enamel coatings were chosen in the following experiments.

IV. Task 2 Enameling process for coating uniformity, surface roughness, and efficiency without adverse effect on steel properties

An API 5L X65 steel pipe (MRC Global) with 323.85 mm in outer diameter and 9.53 mm in wall thickness was used as substrate metal in this study. The steel pipe was first cut into 18 25mm×50mm coupon specimens. The cut specimens were then steel blasted for 1 min to remove mill scale and rusts, and finally cleansed with a commercially available cleansing solvent.

Two types of enamel were applied on the steel coupons: Tomatec slurry and GP2118 powder as shown in Figure 2.1. The enamel slurry was prepared by first milling glass frits, clay and certain electrolytes, and then mixing them with water until the mixture is in a stable suspension state. The enamel slurry was manually sprayed on coupon specimens using a spray gun, which was powered by a jet of compressed air as specified in Table 2.1. The specimens were heated at 150 °C for 10 minutes to drive off moisture, fired at 815°C for 10 min, and finally cooled to room temperature. For electrostatic spraying, the GP2118 enamel powder with an average particle size of 32.8 um was used. An electric field was formed between a nozzle electrode and the sample. Enamel particles, propelled out of the spray gun by a stream of air, became negatively charged, migrated towards the sample (positive electrode) and were deposited. After power spraying, the steel coupons were moved into a furnace and fired at 843 °C for 10 minutes, and then moved out and cooled to room temperature. The thickness of the Tomatec coating was controlled by the spraying time while the thickness of the GP2118 coating was controlled by the number of spray guns. The surface roughness is reported in Section V.

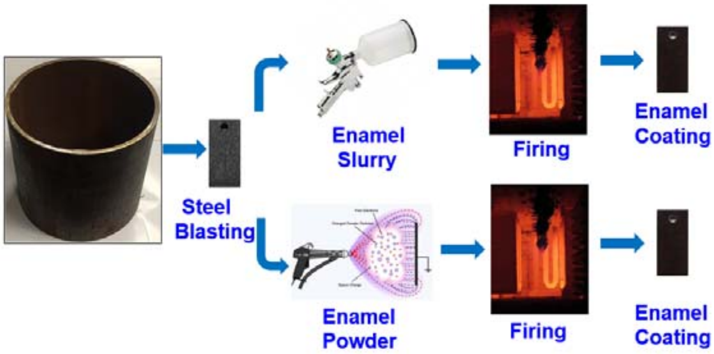

Figure 2.1 Wet coating process vs. electrostatic coating process

Table 2.1 Coating parameters

Coating application parameters	Wet manual spaying	Electrostatic-dry automatic spraying
Chain speed (m/min)	-	12FPM
Voltage (kV)	-	80KV
Atomisation pressure	3.5	0.65
Slip throughput per guns	0.6	0.35
Number of guns	1	12
Distance gun to work piece (cm)	40	50
Transfer efficiency (%)	40	60-80

V. Task 3 Characterization of enamel-coated pipe for microstructure, porosity, chemical adhesion, and corrosion resistance

1. Experimental Program

The phases in coating were examined directly on the surface of coated steel samples by X-ray diffraction (XRD, Philip X’ Pert) with diffraction angle (2θ) varied between 10° and 55°.

To examine the microstructure of each coating, enamel-coated samples were cold mounted in epoxy resin (EpoxyMount, Allied High-Tech Products, Inc.). Each one was cut into a 10.0 mm thick cross section using a diamond saw. The 10.0 mm thick slice samples were abraded with silicon carbide papers with grits of 80, 180, 320, 600, 800, and 1200. After abrading, all samples were rinsed with deionized water and dried in air at room temperature. The microstructure of each sample was examined using a scanning electron microscopy (SEM, Hitachi S-4700, Tokyo). After corrosion tests, the samples were taken out of the sodium chloride solution, washed with distilled water, and dried at room temperature. After drying, the surface conditions on enamel-coated samples particularly with small corrosion products were examined.

The coating thickness and roughness were measured with a coating thickness gauge MiniTest 6008 and optical microscope Hirox, respectively. The bond strength between the coating and its substrate steel were determined using PosiTest following the ASTM D4541-09 [31]. To enhance its bond with the coating, a 20-mm-diameter dolly at base was roughened with abrasive papers, and cleansed with alcohol to remove oxidation and contaminants. The base of the dolly was adhered with a uniform layer of glue to the test coating surface. After curing for 24 h, the coating around the dolly was removed using a 20-mm cutting tool in order to isolate the dolly on a specific test area. The dolly was finally pulled off the sample surface perpendicularly at a stress rate of 0.4 MPa/s. The maximum strength of each coated sample was recorded.

1.1 Investigate the Long-term Corrosion Performance of Small Coupon Samples in 3.5 wt.% NaCl Solution

Open circuit potential (OCP), linear polarization resistance (LPR), and electrochemical impedance spectroscopy (EIS) tests were carried out to monitor the corrosion evolution of the enamel- and epoxy-coated steel samples. A standard three-electrode system was used for electrochemical tests, including a 25.4 mm × 25.4 mm × 0.254 mm platinum sheet as a counter electrode, saturated calomel electrode (SCE) as a reference electrode, and the coated sample as a working electrode. All three electrodes were connected to a Gamry, 1000E Potentiostat/Galvanostat for data acquisition. After each stable OCP was recorded, an EIS test was performed with a sinusoidal potential wave of 10 mV in amplitude around the OCP and a frequency of 100 kHz to 5 mHz. The LPR test was conducted by scanning a range of ±15 mV around the OCP at a scan rate of 0.167 mV/s.

1.2 Investigate the Performance of Large Enamel-Coated Samples with Salt Spray Test

For the salt spray test, the steel pipe was cut into 12 samples with dimensions of 3 in. by 6 in. Each sample was covered with marine epoxy (LOCTITE) in all sides except the front enamel-coated surface. Half of the 12 specimens were coated with enamel GP2118 while the remaining 6 specimens were coated with enamel Tomatec. Three impact points are created on half of samples to simulate the mechanical damage threat. The specimens were spaced approximately 3 in. (75 mm) from each other and placed on the panel with holes for accumulated solution to flow away. The salt fog was constantly distributed throughout the chamber and the average fall-out rate was approximately 2.37 fl-oz (70 mL) for each 12.4 sq-in. (8000 sq-mm) of horizontal surface area over a period of 48 hours. The solution was made by adding 5% USP grade sodium chloride by weight into distilled water. The temperature within the chamber was maintained at 95 ± 3 °F (35 ±2 °C) throughout the whole testing period.

During the test, the chamber was opened periodically for sample surface examination. The undamaged samples were tested for 6 weeks and retrieved after corrosion spots had been observed on all the sample surfaces. While the damaged samples were tested for only one week since the mechanical damaged spots were corroded more rapidly. After testing, coating morphology was evaluated through visual and microscopic cross-sectional examinations. Each enamel-coated sample was first cold-mounted in epoxy resin (EpoxyMount, Allied High Tech Products, Inc.), and cut into a 10.0 mm thick cross section with a diamond saw. The cross-section of the exposed steel was held against an 8-in.-diameter (203 mm) rotating platform and polished with carbide papers from the coarsest to the finest with grits of 180, 320, 600, 800, and 1200. A steady stream of water was used to continually saturate the surface of the polishing paper fixed on the rotating platform. After abrading, all samples were rinsed with deionized water and dried at room temperature. Examination of a finished cross section was then conducted using a scanning electron microscopy (SEM, Hitachi S-4700, Tokyo).

1.3 Investigate Corrosion Resistance of Pipeline Steel with Damaged Enamel Coating and Cathodic Protection

To study the effect of damage on the corrosion resistance of enamel coating, one damage area as shown in Figure 3.1 was created at the center of each enamel-coated sample using an impact test apparatus according to the ASTM Standard G14 [32]. The apparatus consists of a 0.91 kg steel rod with a hemispherical head and a vertical section of hollow aluminum tubing to guide the rod. The weight rod was dropped from a height of 84 cm to damage the coatings. A close-up view in Figure 3.1 shows the detail around the damaged area.

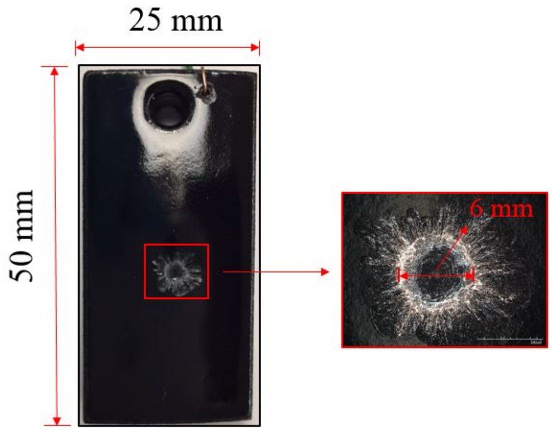

Figure 3.1 Impact induced coating damage

For the pipeline steel with damaged enamel coating and cathodic protection (CP), each coupon sample was embedded into the mount epoxy except the surface of enamel coating to be tested for corrosion performance, as shown in Figure 3.2(a). The mount epoxy was over 2 mm thick to ensure that the enamel coating surface is the response site during electrochemical tests. A PVC funnel (1 cm in diameter) was attached onto the coating surface covering the damage area as shown in Figure 3.2(b). The sample was placed in a large plastic container with the funnel faced up. The funnel and container were filled with 3.5 wt. % NaCl solution to ensure that the funnel is completely submerged. The solution was prepared by adding purified sodium chloride (Fisher Scientific, Inc.) into distilled water. CP was introduced for the entire coated area.

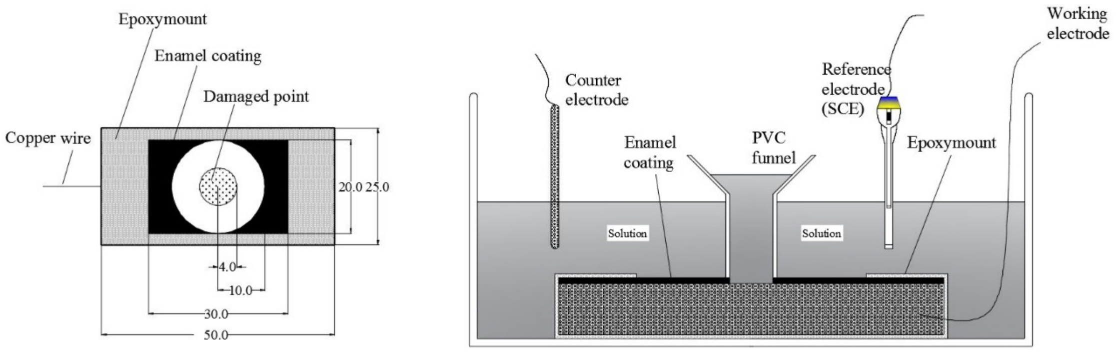

Figure 3.2 Schematic representation of the double electrochemical cell (unit: mm)

During electrochemical tests, the 3.5 wt. % NaCl solution around the damaged coating area was separated by the funnel from the solution around the remaining intact coating area. Otherwise, the electrochemical responses would have been concentrated on the damaged area since its impedance would be much lower than that of the other area and, thus, the measured responses would be representative to neither the damaged coating areas nor the other intact coating area. For the same reason, the damaged and intact coating areas were tested up to 10 days and 70 days, respectively.

The electrochemical tests were conducted at room temperature every 5 days in a classic three-electrode system with a saturated calomel electrode (SCE) as the reference electrode, a graphite rod as the counter electrode, and a coupon sample as the working electrode. The three electrodes were connected to an Interface1000E Potentiostat (Gamry Instrument) for measurement. The SCE and graphite rods were immersed in the large container for the intact enamel coating area, as shown in Figure 3.2, and in the funnel for the damaged enamel coating area (not shown in Figure 3.2 for clarity). One sample was subjected to zero cathodic potential (under the open circuit potential or OCP condition), another one to a cathodic potential of -0.85 vs. SCE/V and the third one to a cathodic potential of -1.15 vs. SCE/V. Potentiostatic tests were first conducted to measure currents for 1,000 seconds at -0.85 vs. SCE/V or -1.15 vs. SCE/V. EIS tests were then conducted under a sinusoidal potential wave (10 mV in amplitude and a frequency range of 10^5 to 10^{-2} Hz) around a cathodic potential of zero, -0.85 vs. SCE/V and -1.15 vs. SCE/V. EIS test data were simulated with classical EEC and analyzed with the software ZSimpWin.

2. Results and Discussion

2.1 Investigate the Long-term Corrosion Performance of Small Coupon Samples in 3.5 wt.% NaCl Solution

2.1.1 Phases in enamel

XRD patterns on the surface of GP2118 and Tomatec enamel-coated samples are identified and displayed in Figure 3.3. Quartz SiO_2 is present in both types of enamel coatings. The highest intensity peaks of quartz SiO_2 were at 26 ° and 26.5 ° for GP2118 and Tomatec enamels, respectively.

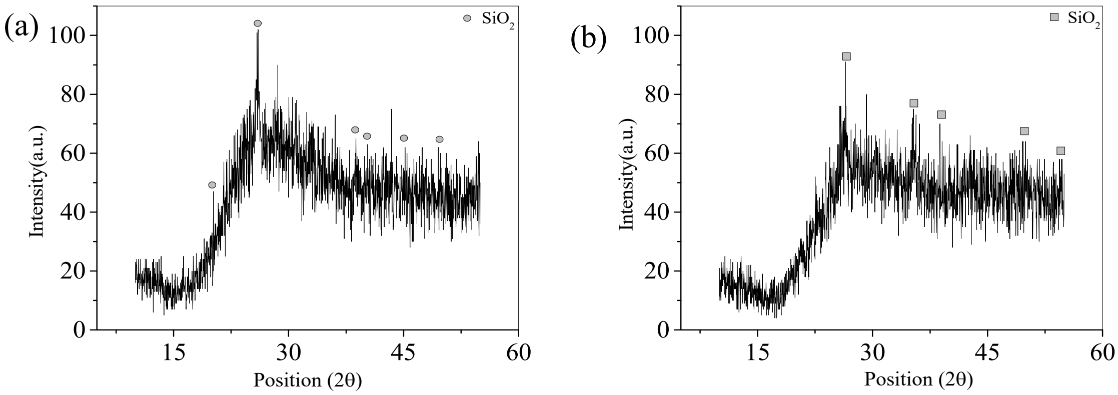

Figure 3.3 XRD patterns for enamel coating: (a) GP2118, and (b) Tomatec.

2.1.2 Microstructure at enamel-substrate interface

Cross-sectional SEM images at the steel-coating interface with different magnifications are presented in Figure. 3.4. The enamel coatings have a solid structure with disconnected air bubbles through the coating thickness as shown in Figures 3.4(a-1) and 3.4(b-1). The air bubbles were formed during the high-temperature chemical reaction of the enamel glass frit with the steel during firing process [24]. The enamel coatings have numerous isolated small pores with the exception of GP2118 enamel that has a few large pores with a diameter of approximately 105 μm. The porosity content of Tomatec enamel was measured to be 4.26%, which is lower than 12.72% for the GP2118 enamel. Figure 3.2(a-2) and Figure 3.2(b-2) show the magnified enamel-steel interfaces at which small-Fe protrusions grow into the enamel coating to form various anchor points. These epitaxial spinel particles improve the bonding between the enamel and its steel substrate [33].

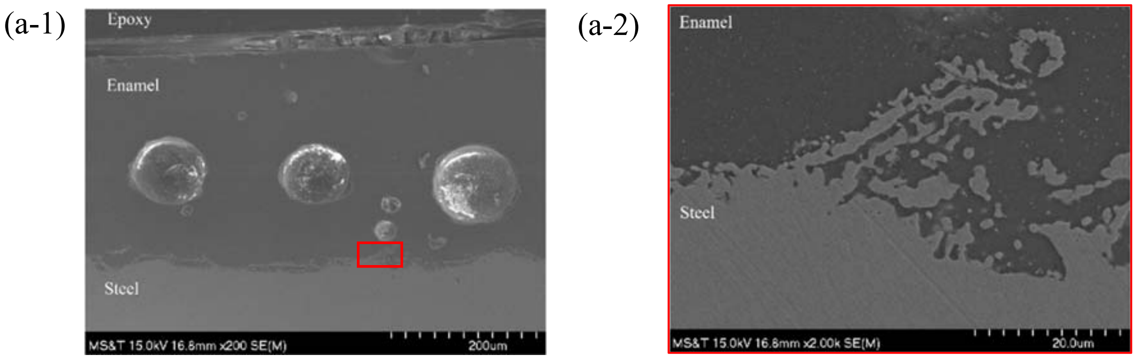

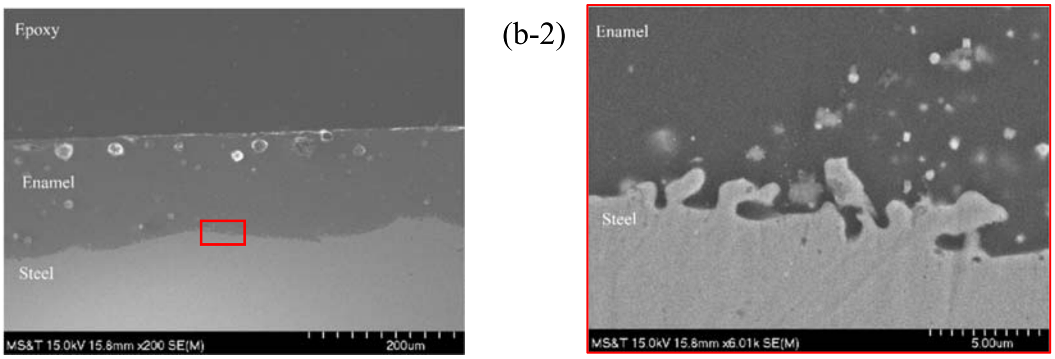
(b-1) (b-2)

Figure 3.4 Cross-sectional SEM images of (a) GP2118, and (b) Tomatec with different magnifications: (a-1) 200×, and (a-2) 2k×, (b-1) 200×, (b-2) 6k×

2.1.3 Pull-off strength

The measured thickness, surface roughness, and bond strength of three types of coatings are summarized in Table 3.1. The average and the standard deviation of the thickness and surface roughness of each coating were calculated from 27 measurements taken from three different samples that were polished to have a flat surface for pull-off test. The average and the standard deviation of the bond strength of each coating were calculated from the three pull-off tests conducted. It can be seen from Table 4 that epoxy coating is the thickest (396 µm) and Tomatec enamel is the thinnest (230 µm). The roughness of the three coatings is around 1 µm, indicating smooth surfaces in all specimens.

Table 3.1 Coating thickness, surface roughness, and adhesion strength

Coating	Thickness (µm)	Roughness (µm)	Bond strength (MPa)	Failure mode
GP2118	340±23	1.05±0.33	17.89±0.84	Mixed
Tomatec	230±8	0.85±0.15	16.85±0.73	Mixed
Epoxy	396±45	0.86±0.06	8.01±2.06	Mixed

At the completion of pull-off tests, the dolly and substrate fracture surfaces are shown in Figure. 3.5. In a pull-off bond test, four possible failure modes include: (1) adhesion break between the coating and its steel substrate; (2) cohesion break within the coating layer; (3) glue break; and (4) mixed break or a combination of the above breaks at multiple locations [34].

Enamel coatings have a mixed failure mode involving a break inside the coating (cohesive break) and a break in glue used to bond the dolly to the specimen. Epoxy coating also has a mixed failure mode involving a break inside the coating (cohesive break), a break between the coating and the substrate steel (adhesive break), and a glue break. There are no adhesive breaks for enamel coatings since the anchor points on the interface increase the bonding between an enamel coating and its substrate steel as shown in Figure 4. Specifically, GP2118 enamel coating has the highest bond strength with an average value of 17.89 MPa, epoxy coating has the lowest bond strength of 8.01 MPa, and Tomatec enamel coating has a bond strength of 16.85 MPa.

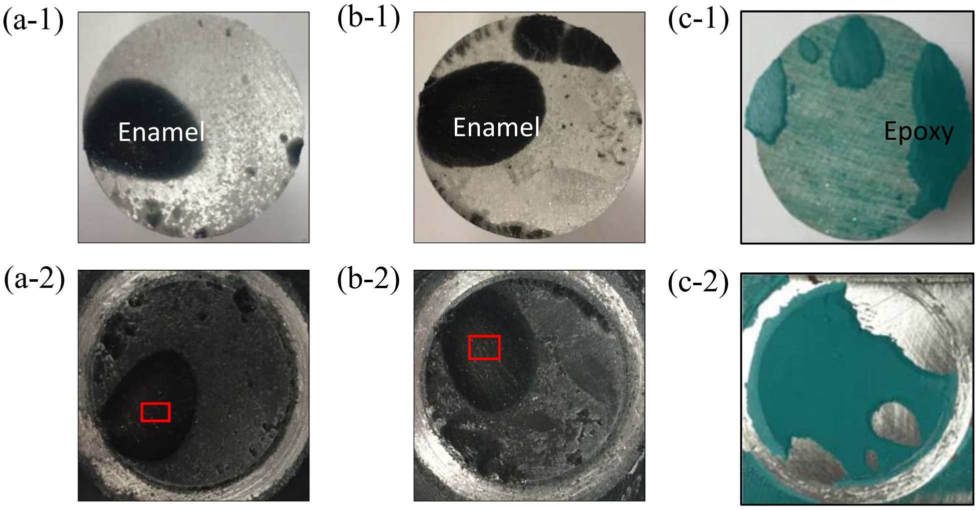

Figure 3.5 Fracture surface morphologies of steel coupons coated with (a) GP2118 enamel, (b) Tomatec enamel, and (c) epoxy: (1) dolly and (2) steel coupons

Figure 3.6(a) and Figure 3.6(b) represent the magnified fracture surface morphologies as shown in Figure 3.5(a-2) and Figure 3.5(b-2), respectively. When the dolly was pulled off the coated specimen at right angle, a crack initiated and propagated across large air bubbles within the coating under increasing loads. Figure 3.7(a) and Figure 3.7(b) show SEM images for the cross sections of the tested specimens in rectangular areas of Figure 3.5(a-2) and Figure 3.5(b-2), respectively. The fracture surfaces of the specimens are generally smooth with the minimum remained coating thicknesses of approximately 70 µm and 40 µm for GP2118 and Tomatec enamels, respectively. In comparison with Figure 3.4, Figure 3.7(a) and Figure 3.7(b) indicate that the fracture surfaces are far away from their corresponding bonding layers at the enamel-substrate interfaces and pass through the weakest layer connecting large air bubbles in the coating since the adherence of enamel on steel surfaces is chemically strengthened with the growth of epitaxial spinel particles in the enamel during chemical reaction in the firing process [33].

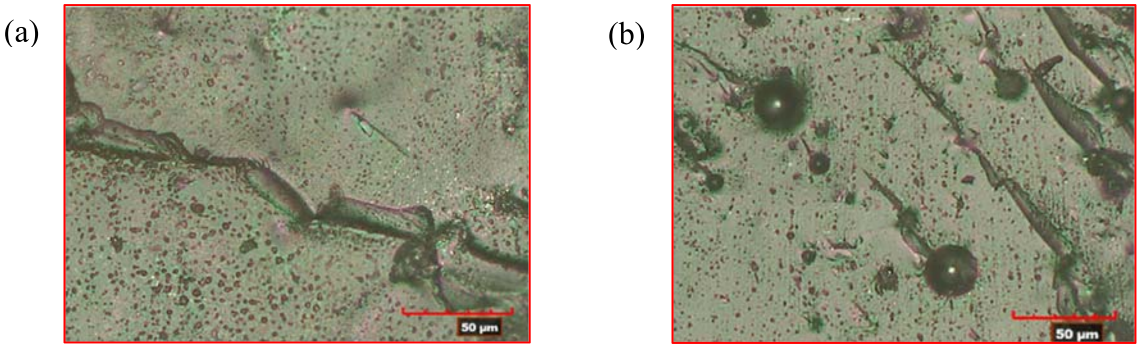

Figure 3.6 Magnified fracture surface morphologies of (a) GP2118 enamel in Figure 3.5(a-2) and Tomatec enamel in Figure 3.5(b-2)

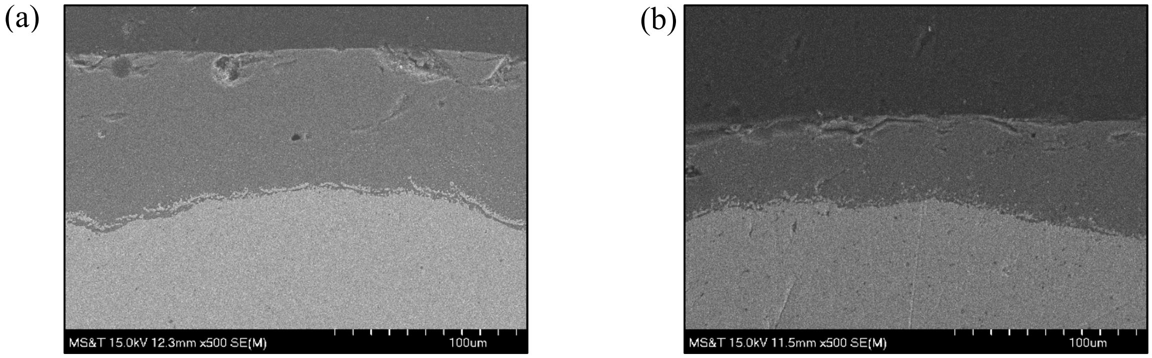

Figure 3.7 SEM images for the cross sections of remained GP2118 and Tomatec enamel coatings in rectangular areas of Figure 3.5(a-2) and Figure 3.5(b-2)

2.1.4 Electrochemical tests

All samples were immersed in 3.5 wt.% NaCl solution and tested at room temperature for 69 days. The solution was prepared by adding purified sodium chloride (Fisher Scientific, Inc.) into distilled water. At the time of 1, 3, 6, 13, 27, 41, 55, and 69 days, open circuit potential (OCP), linear polarization resistance (LPR), and electrochemical impedance spectroscopy (EIS) tests were carried out to monitor the corrosion evolution of the enamel- and epoxy-coated steel samples. The LPR test was conducted by scanning a range of ±15 mV around the OCP at a scan rate of 0.167 mV/s. The LPR curves are used to determine the polarization resistance R_p, which is equal to the slope of the linear region of a polarization curve around zero current:

$$R_p = \Delta E / \Delta i \tag{3-1}$$

where ΔE and Δi represent the voltage and current increments, respectively, in the linear portion of the polarization curve at i=0. LPR measurements were used to calculate the corrosion current density by the Stern-Geary equation:

$$i_{corr} = \beta_a \beta_c / [2.303(\beta_a + \beta_c) R_p] \tag{3-2}$$

where β_a and β_c represent the anodic Tafel constant and the cathodic Tafel constant, respectively, and i_{corr} is the corrosion current.

2.1.4.1 OCP

Figure 3.8 presents the average ± standard deviation of OCP values when each coated sample was immersed in the sodium chloride solution up to 69 days. In general, the variation of three data points for each test coating is large in the first 6 days and reduced afterward. The average OCP values of the GP2118 and Tomatec enamel-coated samples decrease significantly in the first 13 days, and then approach an asymptotic value of -0.25 and -0.3 V/SCE, respectively. The average OCP of the epoxy-coated samples decreases dramatically in the first 6 days, and gradually approaches -0.32 V/SCE. The initial rapid drop of OCP values is due to the penetration of electrolyte through the defects in coating. As corrosion products formed over time gradually clog the defects, the corrosion process decelerates and becomes stabilized eventually. According to ASTM C876, if potentials are more positive than -127 mV/SCE, the possibility for reinforcing steel corrosion is less than 10%. When the potential ranges from -127 mV to -276 mV/SCE, corrosion probability is uncertain and corrosion probability is higher than 90% for OCPs lower than -276 mV/SCE [35]. The OCPs of the final immersion day indicated that GP2118 enamel significantly increased the exposure time span in solution to severe corrosion compared with Tomatec enamel and epoxy coating.

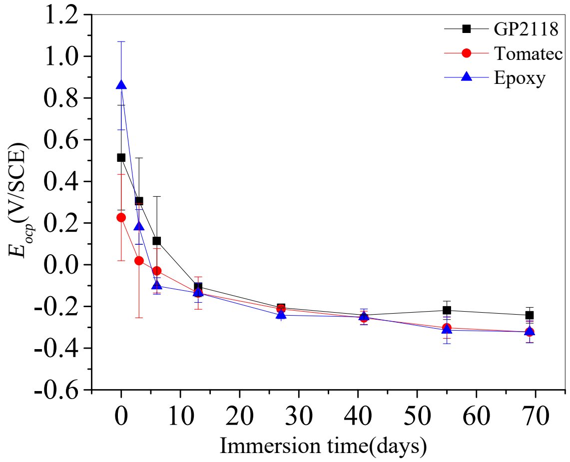

Figure 3.8 OCP values of various samples in 3.5 wt.% NaCl solution for up to 69 days

2.1.4.2 LPR

Figure 3.9 displays the average ± standard deviation of the corrosion current densities of three identical samples for each coating, calculated from Eq. (3-2), as a function of immersion time up to 69 days. Overall, the average corrosion current densities of the enamel- and epoxy-coated samples share a similar trend of increase over time because the gradual penetration of electrolyte through the coating increases the corrosion current in the samples. Specifically, the average corrosion current densities of GP2118 and Tomatec enamel-coated samples significantly increase from 7.05×10^{-13} A/cm^2 and 1.03×10^{-12} A/cm^2 in 1 day of corrosion tests to 6.76×10^{-10} A/cm^2 and 6.25×10^{-10} A/cm^2 in 27 days, and then are gradually stabilized at $6.82\times10^{--9}$ A/cm^{2}and 5.76×10^{-9} A/cm^2, respectively. For the epoxy-coated samples, the starting corrosion current density (3.24×10^{-13} A/cm^2) in 1 day of immersion and the ending corrosion rate (2.00×10^{-8} A/cm^2) in 69 days are respectively lower and higher than their corresponding values of the enamel-coated samples. Consistent with the OCP evolution over time, LPR data indicate that the epoxy-coated samples degrade more rapidly than the enamel-coated samples. According to the Durar Network Specification [10], the corrosion level may be divided into four levels, passivity when $i_{corr} <$ 0.1μA/cm^2, low corrosion when 0.1μA/cm^2 $< i_{corr} <$ 0.5μA/cm^2, high corrosion when 0.5μA/cm^2 $< i_{corr} <$ 1μA/cm^2, and very high corrosion when 1μA/cm^2 $< i_{corr}$. For all the enamel- and epoxy-coated samples, the corrosion current densities are less than 0.1μA/cm^2, which indicates that all the enamel and epoxy coatings can provide good corrosion protection for the substrate steel.

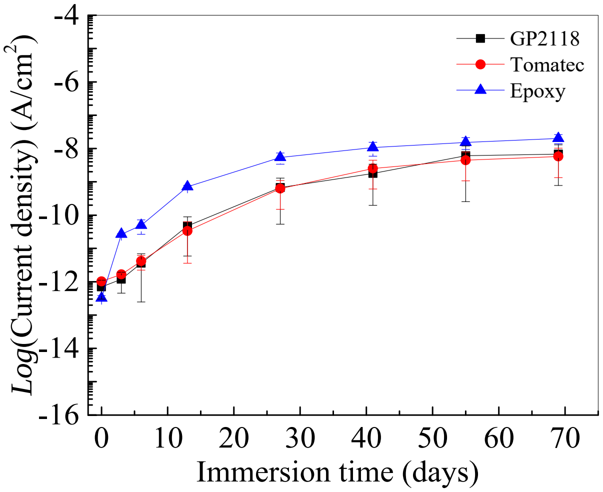

Figure 3.9 Corrosion rates of various samples in 3.5 wt.% NaCl solution for up to 69 days

2.1.4.3 EIS

Figure 3.10 shows the EIS Bode diagrams of 3 representative samples with 2 types of enamel coatings and 1 epoxy coating when immersed in 3.5 wt.% NaCl solution up to 69 days. Overall, the Bode diagrams of enamel- and epoxy-coated samples are similar, indicating similar corrosion performance of the coated samples. Specifically, the impedance values of enamel-coated samples at low frequency 5 mHz drop slightly from 10^{11} Ω cm^2 in the first 6 days, rapidly in the following 5 weeks, and then slowly to over 10^6 Ω cm^2 in the final 4 weeks. These impedances are still higher than 10^5 Ω cm^2 [15], a threshold value below which the protection of coatings as barriers is basically lost. The horizontal platform in impedance diagrams gradually extends from very low frequency at the beginning of tests to middle frequency over time. Therefore, the impedance spectra gradually deviate from those that represent pure capacitive behavior, indicating that the coating resistance and coating capacitance decreased and increased, respectively, as a result of electrolyte penetration through the coating [14]. The phase angles always approach to 90° at high frequency but decrease quickly with immersion time at low and middle frequencies, which is mainly due to the rapid reduction of coating resistance [15].

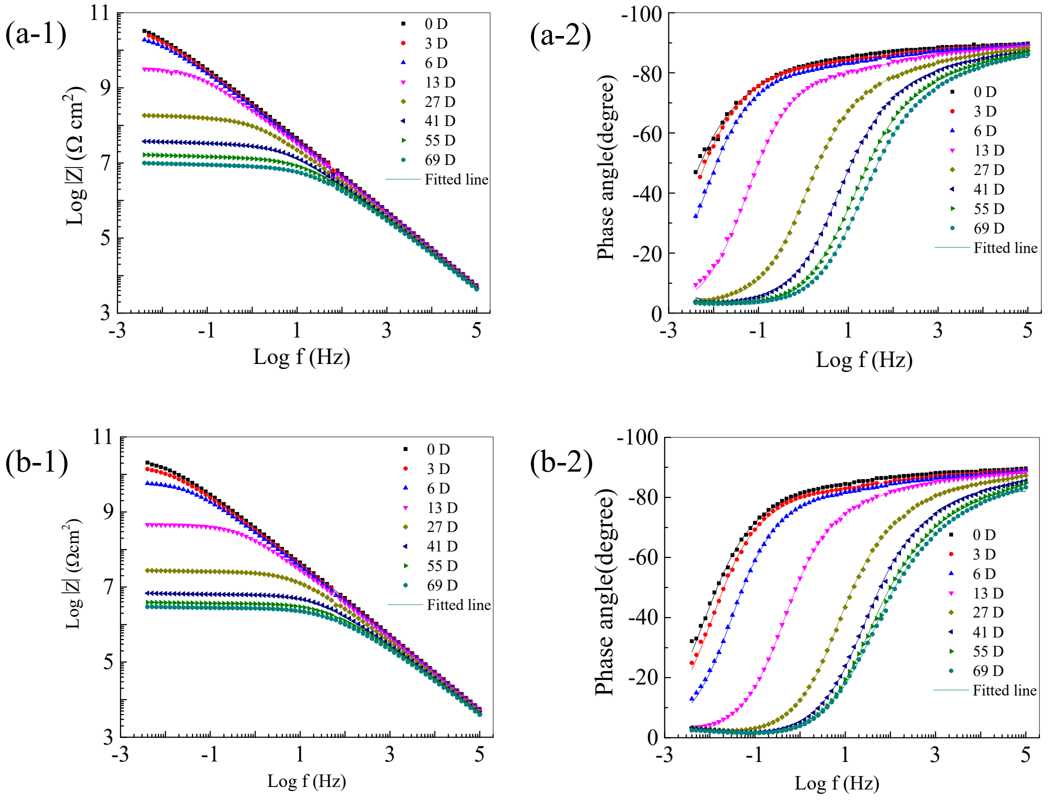

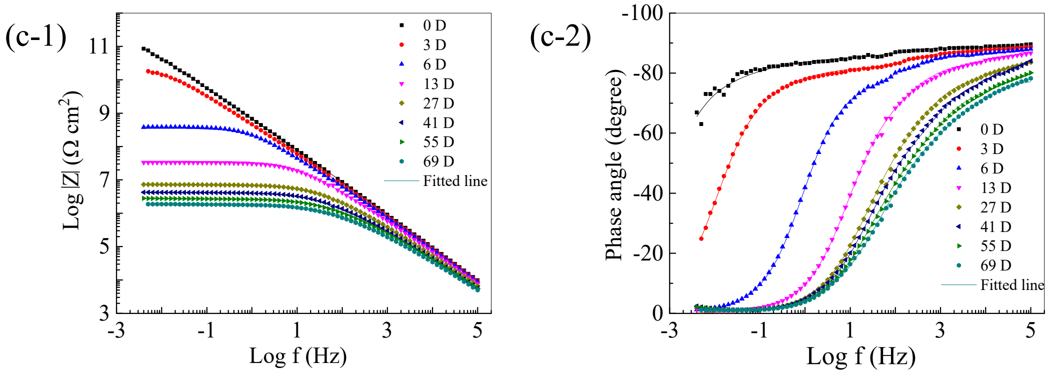

Figure 3.10 Bode diagrams for (a) GP2118-, (b) Tomatec-, and (c) epoxy-coated steel samples: (1) impedance and (2) phase angle

In the Bode diagrams, the dotted data points in various symbols mean measurements taken at different times of corrosion tests while the solid lines represent curve fitting by two equivalent electric circuit (EEC) models as shown in Figure. 3.11. Model (a) in Figure. 3.11 was used to fit the EIS test data up to 13 days of immersion with water and oxygen molecules arriving at the substrate surface and reacting with the steel. However, only one capacitive loop was observed in phase-angle diagrams. This is likely because the two time constants corresponding to electrochemical reactions on the substrate steel/electrolyte interface and the dielectric properties of enamel coatings are nearly in the same order of magnitude. After 27 days of immersion, Model (b) in Figure 3.11 was used to fit the EIS test data till the end of corrosion tests in 69 days. In this case, a Warburg impedance *W* was included to take into account the diffusion behavior, which was caused by the accumulation of corrosion products on the corrosion active sites.

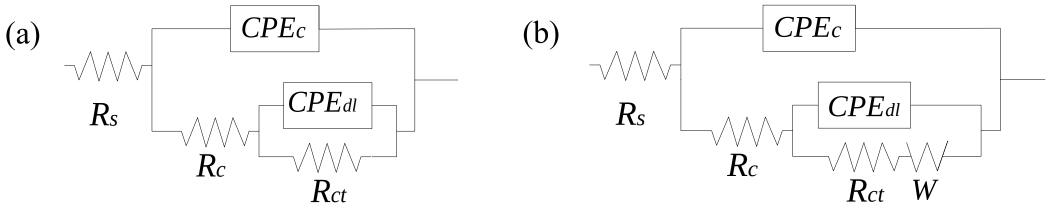

Figure 3.11 EEC models of enamel- and epoxy-coated samples: (a) in the first 13 days and (b) from 27th day to the end of tests

ZSimpWin was used to determine the parameters in the two EEC models based on the EIS test data recorded. A chi-squared value of 10^{-4} to 10^{-3} achieved indicated a satisfactory fitting goodness. Specifically, R_s represents the solution resistance, R_c and CPE_c mean the coating resistance and capacitance, R_{ct} and CPE_{dl} represent the charge transfer resistance and the double layer capacitance at the electrolyte-steel interface. A constant phase element (CPE) was introduced to signify the deviation from a pure capacitor. For example, CPE_c took into account the non-homogeneity in coating thickness and roughness, and CPE_{dl} accounted for a non-uniform distribution of potential.

Figure 3.12 shows the properties of enamel and epoxy coatings: coating resistance R_c and coating capacitance C_c, in which the average ± standard deviation values were determined from the measurements taken from three samples of identical condition. In general, the coating resistance measures the performance of a coating as a barrier against electrolyte penetration, which is closely related to coating microstructures such as open pores and pinholes. The coating capacitance indicates the diffusion of electrolyte solution into the coating, which is associated with the dielectric property, microstructure, and thickness of the coating. It can be observed from Figure 3. 12 that resistances of the two enamel coatings decrease gradually while the coating capacitances slightly increase with the immersion time. The reason is that electrolyte solution gradually penetrates into the coating, thus increasing the coating capacitance. The properties of epoxy coating follow the same changing trend as the enamel coatings. However, after 13 days of immersion, the resistance and capacitance of the epoxy coating are smaller and larger, respectively, than those of the enamel coatings. Therefore, enamel can more effectively prevent electrolyte from penetrating through the coating than epoxy.

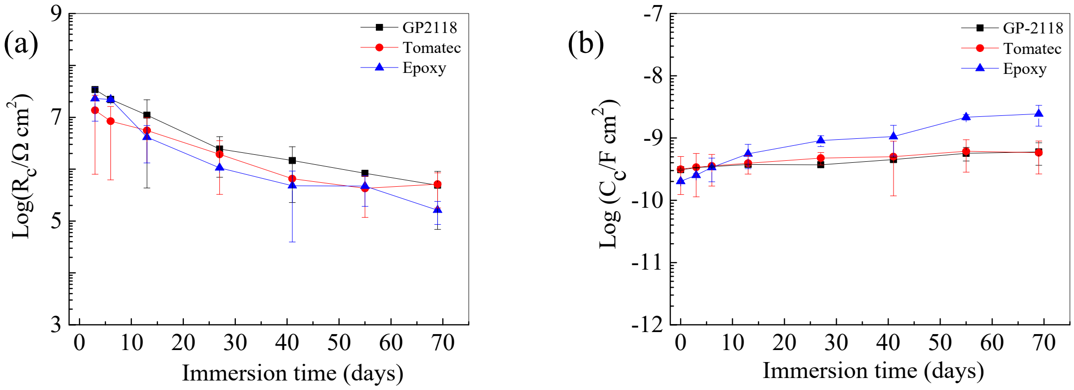

Figure 3.12 Comparison of coating properties: (a) coating resistance R_c and (b) coating capacitance C_c

Figure 3.13 displays the steel-solution interfacial properties of enamel- and epoxy-coated samples: charge transfer resistance R_{ct} and double layer capacitance C_{dl}, in which the average± standard deviation values were determined from the measurements taken from three samples of identical condition. The charge transfer resistance is a measure of how easily electrons can transfer across the metal surface, which is inversely proportional to the corrosion rate [28]. It can be seen from Figure 3.13 that the charge transfer resistances of the enamel- and epoxy-coated samples decrease rapidly with immersion time since more electrochemically reactive spots appear on the substrate interface over time. After 3 days of immersion, the GP2118 enamel-coated samples have the highest charge transfer resistance among three types of coating, which is in general agreement with the low corrosion rates as presented in Figure 3.9. The double layer capacitance C_{dl}, calculated from Eq. (1-5), is also a measure of the ease of charge transfer. The C_{dl} of epoxy-coated samples increases rapidly with immersion time up to 13 days and gradually to arrive at 33.29 nF cm^{-2} at 69 days of immersion. The C_{dl} of Tomatec enamel-coated samples slightly fluctuates over time and finally reaches to 3.85 nF cm^{-2}. The C_{dl} of GP2118 enamel-coated samples is quite stable throughout the corrosion tests with a value of 0.77 nF cm^{-2}, which is the lowest among the three coatings at the end of corrosion tests in 69 days. Among three types of coatings, GP2118 enamel most effectively protects its substrate steel from corrosion since its charge transfer resistance and double layer capacitance are respectively the highest and the lowest.

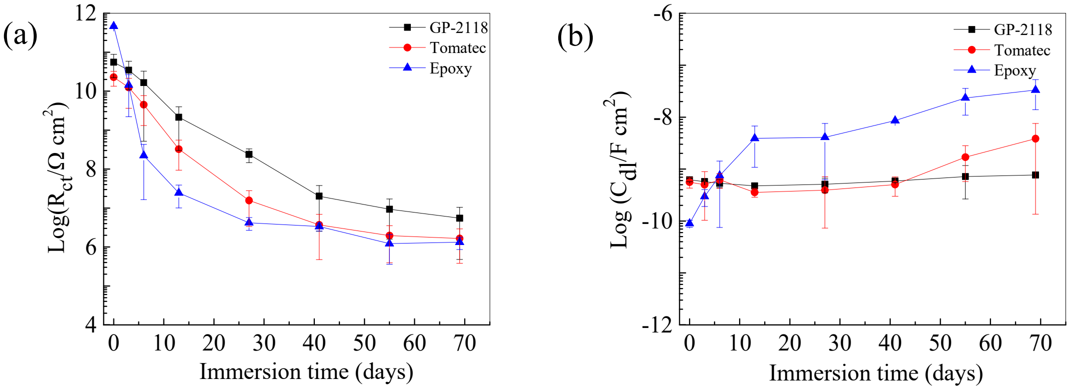

Figure 3.13 Comparison of steel-solution interfacial parameters: (a) charge transfer resistance and (b) double layer capacitance

2.1.5 Visual observation after corrosion tests

After corrosion tests, the surface conditions of all tested samples were examined visually. No corrosion products was observed on the surface of enamel and epoxy coatings. All the coatings can provide excellent corrosion protection for their substrate steel. This observation is consistent with the electrochemical test data such as the lowest corrosion resistances exceeding their threshold value.

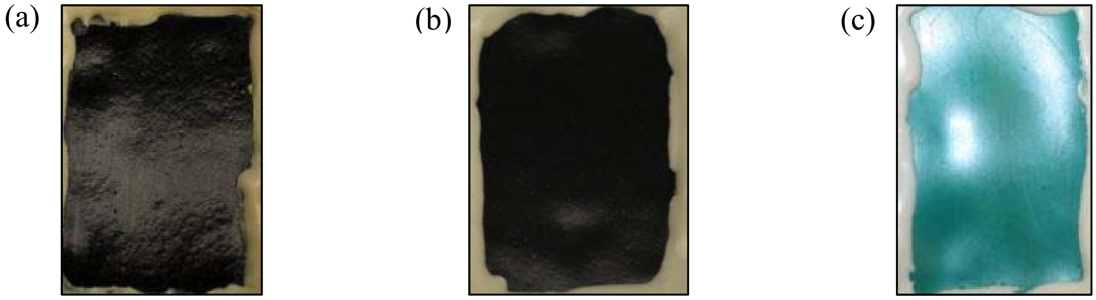

Figure 3.14 Surface conditions of (a) GP2118 enamel-, (b) Tomatec enamel-, and (c) epoxy-coated samples after corrosion tests

2.1.6 Conclusions

In this study, the phase composition, microstructure, surface roughness, bond strength, and corrosion resistance of GP2118 enamel-coated, Tomatec enamel-coated, and epoxy-coated samples have been investigated. Based on the test results and analysis, the following conclusions can be drawn:

1. Quartz SiO_2 phase was identified in GP2118 powder and Tomatec slurry enamels. Their coatings on steel samples have solid structures with disconnected pores, resulting in a porosity content of 12.72% and 4.26%, respectively. The enamel and epoxy coatings tested have a surface roughness of approximately 1.0 μm.
2. The enamel coatings applied on steel pipe samples failed in mixed mode involving a break inside a coating layer and a break in the glue used to attach a test dolly to the coating. They showed no adhesive break since small Fe protrusions grew into the coatings to form anchor points at enamel-steel interfaces. In addition to the breaks in enamel coating, the epoxy coating may also fail at the coating-steel interface due to weak bond.
3. The results from three electrochemical tests (OCP, LPR, and EIS) are in general agreement. As electrolyte gradually penetrates through various coatings over time, the OCP values of all coated samples decreased, the corrosion current densities increased, and the coating resistance and charge transfer resistance decreased while the coating capacitance and double layer capacitance increased. The epoxy coating degraded more rapidly than the

enamel coatings tested. Overall, there is no obvious sign of corrosion in all coated samples tested in 69 days as confirmed by visual inspection.

4. The Bode diagrams of GP2118 enamel-, Tomatec enamel-, and epoxy-coated samples evolve over time in similar ways. At the completion of corrosion tests in 69 days, the average impedances of the three types of samples at 5 mHz were reduced to 9.04 MΩ cm^2, 3.12 MΩ cm^2, and 1.88 MΩ cm^2, respectively, while their phase angles at high frequency all approached to 90°. The coatings are good barriers against electrolyte penetration and can protect substrate steel from corrosion in sodium chloride solution. The enamel coatings revealed the same corrosion protective behavior as the epoxy coating.

2.2 Investigate the Performance of Large Enamel Coated Samples with Salt Spray Test

Salt spray test, as an accelerated corrosion test, produces a corrosive attack to coated samples in order to evaluate the performance of coating for corrosion protection. Coated samples are placed in and periodically taken out of a chamber for examination on the potential formation of corrosion products on the sample surface. In general, the more corrosion-resistant the coating is, the longer the test lasts prior to the appearance of corrosion products.

The salt spray test was conducted according to the standard practice for operating salt spray (Fog) Apparatus (ASTM B1187-16) with the Q-FOG cyclic corrosion tester as shown in Figure 3.15. Generally, a salty fog, which is continuously supplied with salt water and a steady stream of clean compressed air, is injected into the enclosed chamber through a nozzle (or atomizer) located in the middle of the chamber's floor. The salt solution that gradually accumulates inside the chamber is disposed through a drain positioned on the chamber floor. Besides, an elevated temperature is maintained inside the chamber with the built-in heating units.

Figure 3.15 Salt spray chamber

2.2.1 Surface observation

Figure 3.16 shows the surface conditions of six undamaged specimens after each week's salt spray. The left three samples were coated with GP2118 enamel and the right three samples were coated with Tomatec enamel. After two weeks' testing, none of the samples showed any signs of corrosion. By the end of the third week, the second Toamtec enamel-coated sample showed one corrosion spot. After four weeks' testing, the first GP2118 enamel-coated sample showed one corrosion spot and the first Tomatec enamel-coated sample showed two corrosion spots. After five weeks of salt spray tests, the corrosion spot generated on the second GP2118 enamel-coated sample and the third Tomatec enamel-coated sample. By the end of the sixth week, a tiny corrosion spot started on the third GP2118 enamel-coated sample surface. Thereafter, all the samples had corrosion spots of various size. Figure 3.17 showed each sample surface condition at the completion of salt spray tests. The red circles showed the exact corrosion spots and all the corrosion spots were relatively small. Only pitting corrosion generated and no significant corrosion occurred during the entire salt spray tests.

1st week

2nd week

3rd week

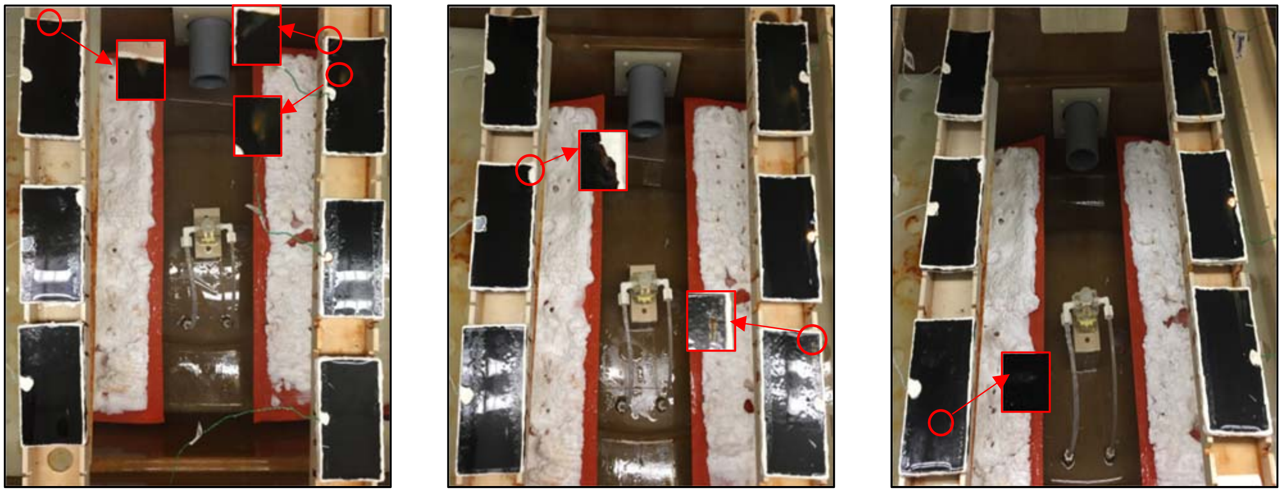

4th week

5th week

6th week

Figure 3.16 Undamaged specimen surface conditions after each week of salt spray tests. (Left: enamel GP2118; Right: enamel Tomatec)

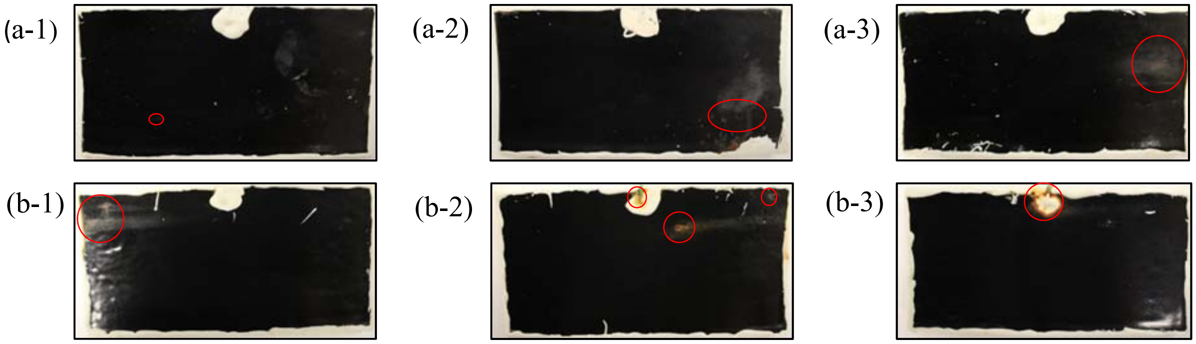

Figure 3.17 Undamaged specimen surface conditions after 6 weeks of salt spray test. (a: GP2118 enamel; b: Tomatec enamel)

Figures 3.18 (a) and 3.18 (b) show the surface conditions of six damaged specimens prior to the salt spray test and after 48 hours of salt spraying, respectively. After 48 hours of testing, brown corrosion products on damaged points of all the tested samples were clearly observed, except the third Tomatec enamel-coated sample showed minor corrosion on the damaged points only. Figure 3.19 shows the sample surface conditions after one week of salt spray tests. Severe corrosion happened around the impact points with corrosion products flew down.

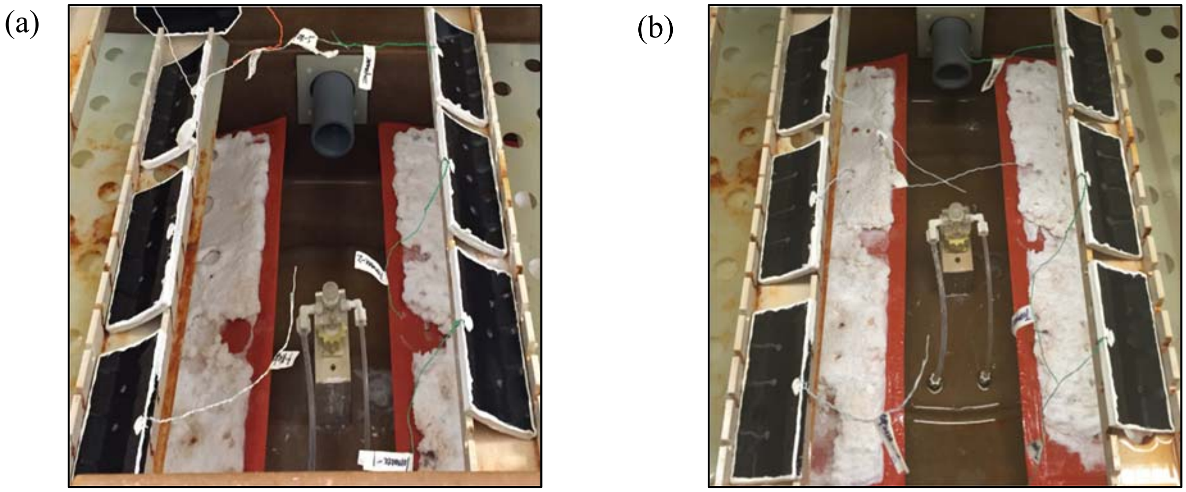

Figure 3.18 (a) Damaged specimen layout prior to salt spray test; (b) Specimen surface conditions after 48 hours of salt spray tests. (Left: GP2118 enamel; Right: Tomatec enamel)

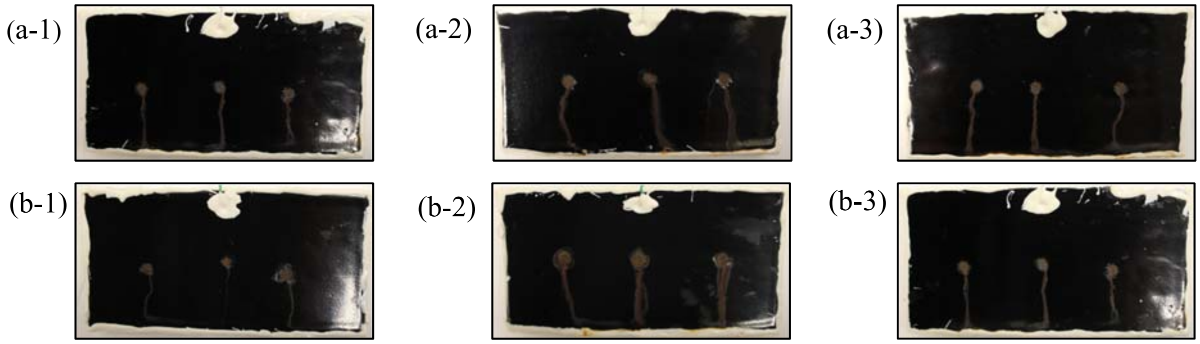

Figure 3.19 Specimen surface conditions after one week of salt spray test
(a: damaged GP2118 enamel; b: damaged Tomatec enamel)

2.2.2 Microstructure of GP2118 and Tomatec enamel-coated samples

Cross-sectional SEM images of both enamel-coated steel samples are presented in Figure 3.20. GP2118 enamel-coated sample has an amorphous structure with approximately 180 μm thick. The air bubbles in the coating are disconnected and the porosity content is approximately 3.51%. The coating contains several big air bubbles with a diameter of up to 41 μm. For the Tomatec enamel-coated sample, the coating thickness is approximately 235 μm. It has more air bubbles with a porosity content of 6.57% and the largest diameter smaller than that of GP2118 enamel. Figures 3.20(a-2) and 3.20(b-2) show the corrosion sections of damaged areas. The substrate steel remained covered with enamel coating and the bonding between the enamel coating and its substrate steel remained in existence.

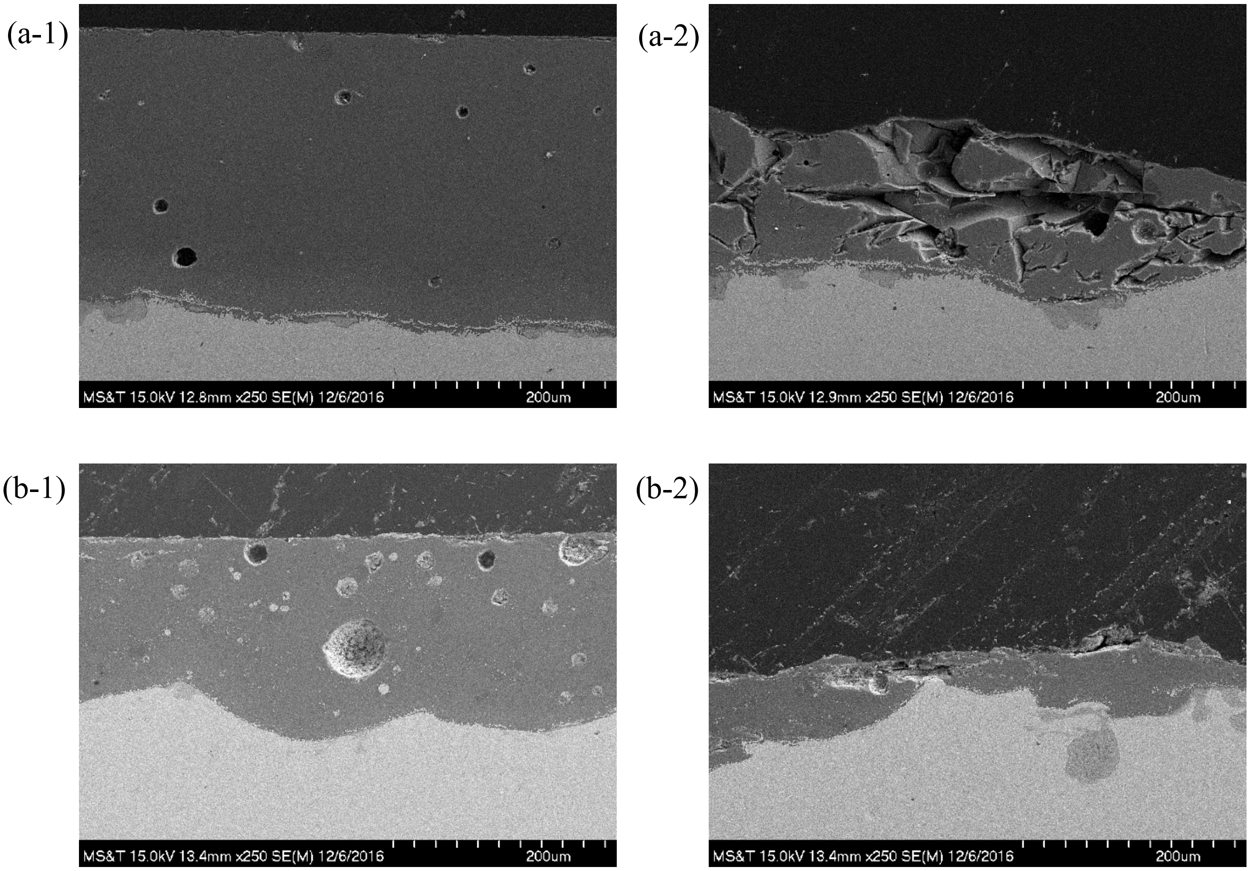

Figure 3.20 Cross-sectional SEM images of (a) GP2118 enamel, (b) Tomatec enamel with magnification of 200×

2.2.3 Conclusions

Intact enamel-coated samples performed well throughout the salt spray test. Only minor corrosion spots appeared on the surface of samples. For the damaged samples, corrosion occurred quickly on the impact points and the SEM images showed that the substrate steel remained covered with enamel coating and the bond between the enamel coating and the steel remained intact.

2.3. Investigate Corrosion Resistance of Pipeline Steel with Damaged Enamel Coating and Cathodic Protection

2.3.1 Characterization of enamel coatings

Cross-sectional SEM images of enamel-coated steel samples tested under the OCP and CP (-1.15V/SCE) conditions are presented in Figure 3.21. In general, the enamel coatings have amorphous structures with isolated air bubbles. Gaseous CO, CO_2, and H_2 are generated during the firing process of enameling. When cooled down, these gases are trapped as a thick layer of enamel is solidified, generating the isolated air bubbles. Figures 3.21(a) and 3.21(b) represent the radial sections crossing the damage area by stitching five SEM images taken at five points in radial direction as shown in Figure 3.1. Due to the falling-off of chipped coating after impact tests, the coating thickness decreased gradually from 244 μm to 4 μm for samples to be tested under the OCP, and from 190.48 μm to 4 μm for samples to be tested under -1.15 V/SCE. However, the substrate surface is still covered with a thin layer of enamel coating at the center of damaged area as indicated in Figure 3.1.

Figures 3.21(c) and 3.21(d) are the magnified details at enamel-steel interfaces from Figures 3.21(a) and 3.21(b). They show the extensive formation of an island-like structure in the enamel coating during the firing process, thus forming a durable enamel-steel interface transition zone. The island-like structure are the iron-alloys formed as a result of the chemical reactions of metal oxides in the enamel and the carbon and iron in the steel. No cathodic delamination was found after the corrosion tests, and the CP thus did not affect the mechanical condition of the interface between the enamel coating and steel substrate.

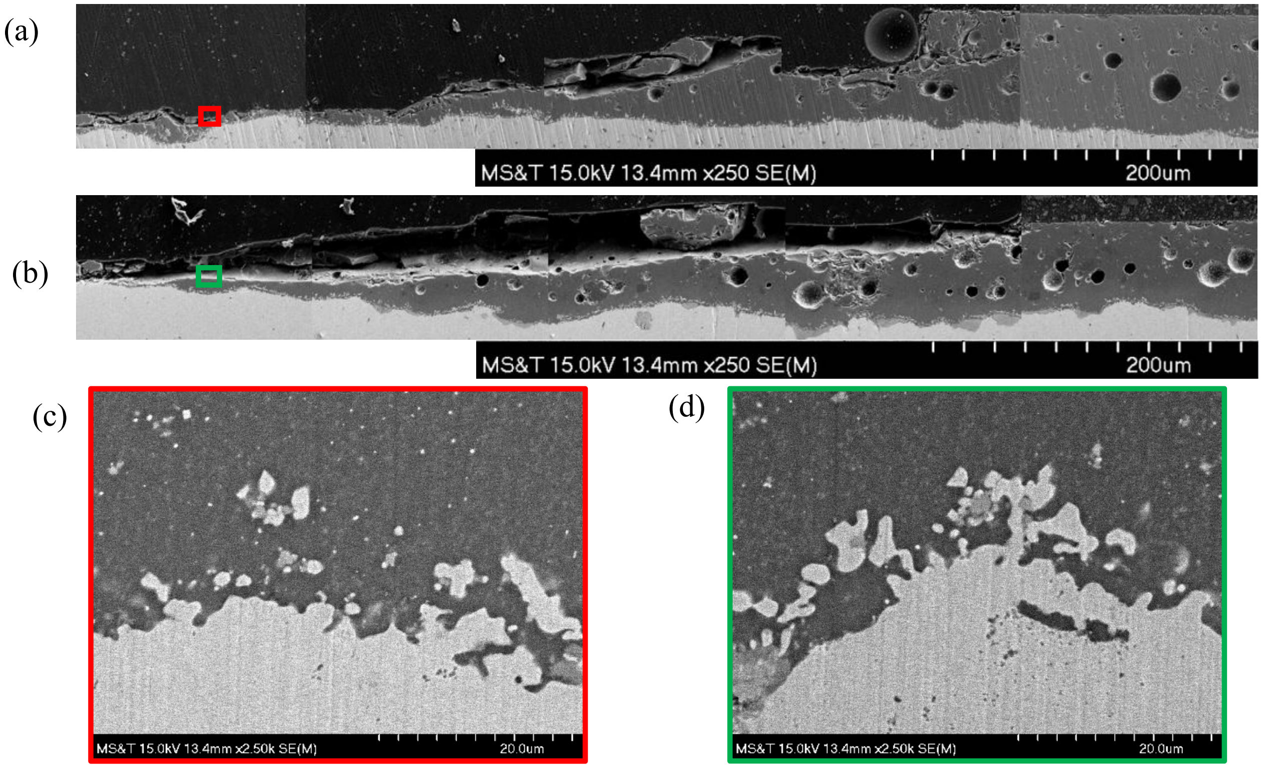

Figure 3.21 Cross-sectional SEM images of enamel-coated samples under the OCP (a and c) and -1.15 V/SCE (b and d) with a magnification of 250× (a and b) and 2500×(c and d)

2.3.2 Electrochemical tests

2.3.2.1 EIS

Figure 3.22 shows the EIS Bode diagrams of 3 representative samples tested under a cathodic potential of -1.15 V/SCE and -0.85 V/SCE, and an OCP, respectively, in intact enamel coating (a-1, b-1 and c-1) and damaged enamel coating (a-2, b-2 and c-2). Both the measured (Meas.) data in various symbols and their fitted (Ftd.) curves are presented in Figure 3.22. On a log-log scale, the impedance of the sample tested under -1.15 V/SCE in the first 40 days decreased linearly with the frequency; this relation was independent of the day of testing as indicated in Figure 3.22(a-1). Starting from the 50th day, the impedance experienced a gradual decrease at low frequency but remained over 10 GΩ cm^2 at a frequency of 0.02 Hz. The phase angles in the high and middle frequency ranges were close to 90° during the entire immersion time and increased with the frequency in the low frequency range.

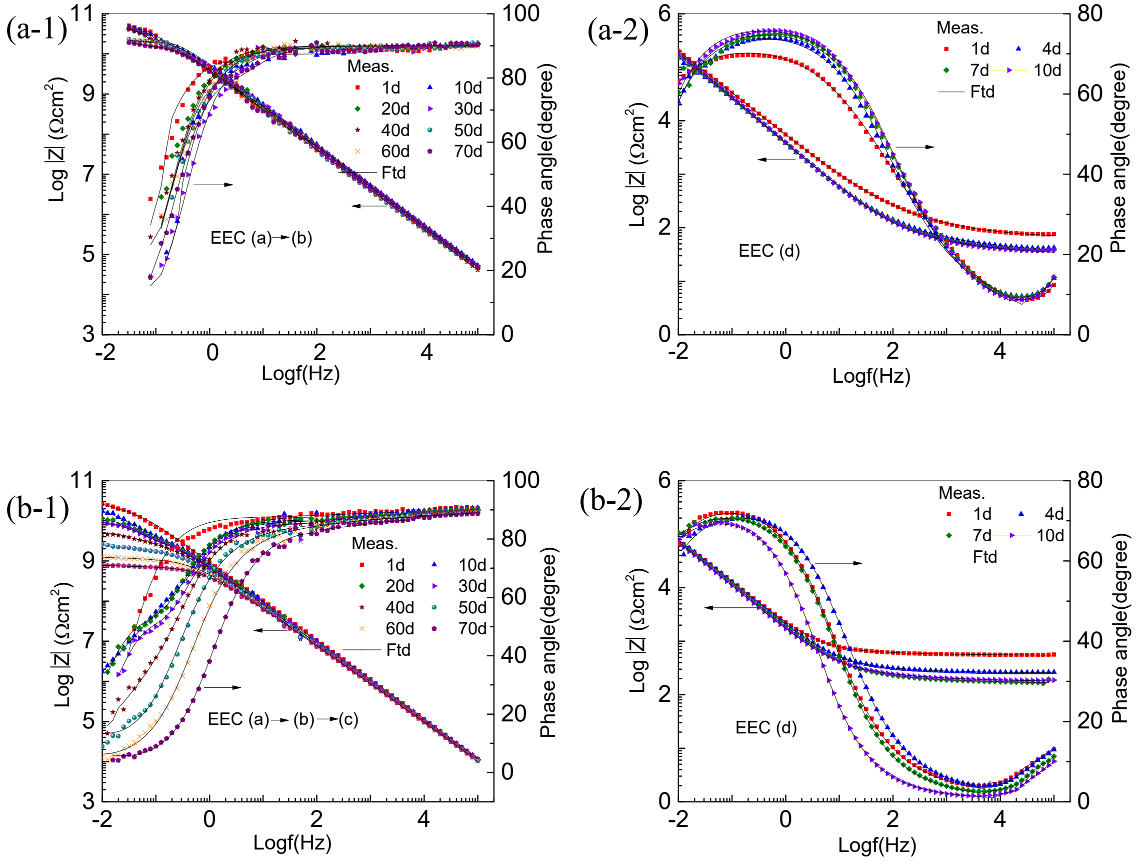

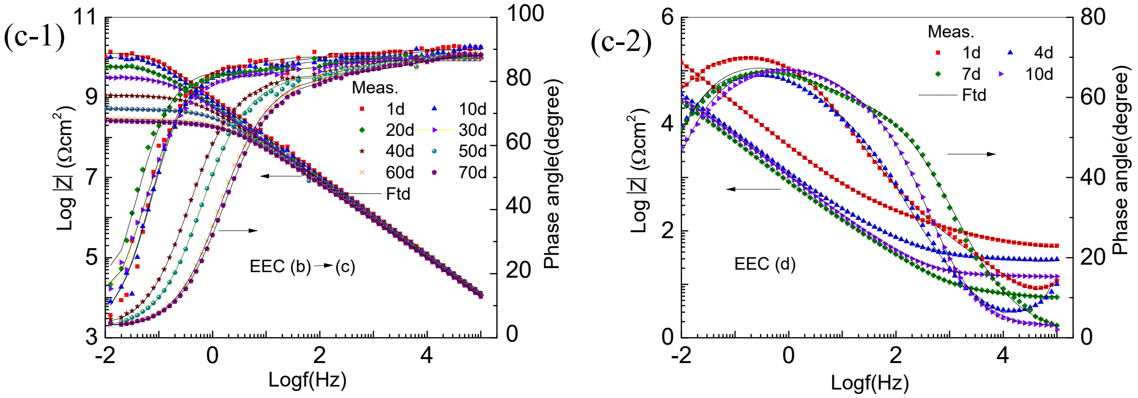

Figure 3.22 Bode diagrams of enamel-coated samples immersed in 3.5 wt.% NaCl solution up to 70 days at (1) intact coating zone, and up to 10 days at (2) damaged coating zone under a cathodic potential of (a) -1.15 vs. SCE/V, (b) -0.85 vs. SCE/V, and (c) the OCP

For the sample tested under a cathodic potential of -0.85V/SCE, as shown in Figure 3.22(b-1), the impedance on a log-log scale decreased linearly in the first 10 days and then showed a gradually-expanding horizontal plateau in the low to middle frequency range over time. The impedance at a frequency of 0.02 Hz decreased from 24 GΩ cm^2 at the beginning to 0.76 GΩ cm^2 at the end of the test. The phase angle increased with the frequency from the low to middle frequency range and remained 90° till 70 days of immersion time in the high frequency range. The phase-frequency curves in the low frequency range were shifted towards the middle frequency range over the immersion time.

The impedance and phase angle of the sample tested under the OCP, as shown in Figure 3.22(c-1), showed a similar trend to the sample tested under a cathodic potential of -0.85V/SCE, particularly towards the end of corrosion tests. However, the horizontal plateau was further extended to the middle frequency range and the impedance at a frequency of 0.02 Hz was 0.26 GΩ cm^2 after 70 days of testing.

Figures 3.22(a-2), 3.22(b-2) and 3.22(c-2) show the Bode diagrams of the samples tested in the damaged-coating zone. Overall, the Bode diagrams of the samples tested under the CP and the OCP are similar, indicating comparable corrosion performances of all the samples in the damaged zone. The impedance became stable after four days of immersion in the solution. Because of the damage made on the coating, the impedance at 0.02 Hz was approximately 0.1 MΩ cm^2, which is 10^6 times smaller than that of the samples tested in the intact coating zone. On a log-log scale, the impedance linearly decreased in the low frequency range and gradually approached an asymptotic value in the high frequency range. The maximum phase angle, lower than 80°, appeared in the low frequency range, indicating that corrosion had already taken place in the steel substrate.

Figure 3.23 shows four EEC models used to fit the EIS test data taken from different samples under various test conditions.

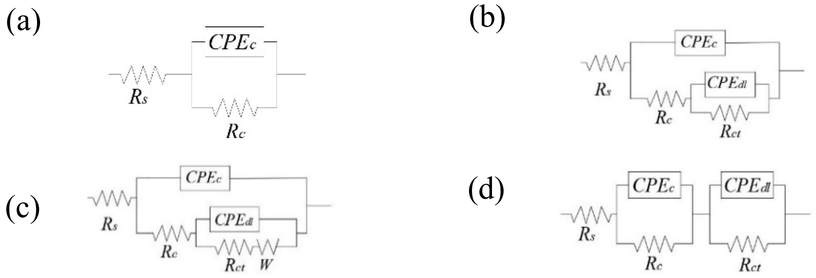

Figure 3.23 Equivalent electrical circuit (EEC) models

The EEC models used to fit into the EIS data from various tested samples are included in Figure 3.23. Model (a) was used for the samples with intact coating tested under -1.15V/SCE up to 40 days, considering the decrease in coating resistance and increase in coating capacitance as water begins to seep through the channels in enamel coating. Here, R_s represents the solution resistance, R_c and CPE_c mean the pore resistance and capacitance of the coating, respectively. After 40 days of immersion when water and oxygen molecules arrived at the substrate surface and reacted with the substrate steel, the EIS data was fitted with Model (b) till the end of corrosion tests. Here, R_{ct} is the charge transfer resistance and CPE_{dl} is the double layer capacitance at the steel-electrolyte interface. However, only one capacitive loop was observed in the phase-frequency diagram. This is likely because the time constant associated with the dielectric properties of enamel was difficult to distinguish from that of the electrochemical reaction at the steel-electrolyte interface.

For the intact enamel coating zone under -0.85V/SCE, Model (a) was used in the first 10 days of immersion, Model (b) was applied from the 15th day to the 45th day, and Model (c) was used till the last day of testing. A Warburg impedance W in Model (c) was included to take into account the diffusion behavior, which was induced by the accumulation of corrosion products at the corrosion active sites. For the intact coating zone under the OCP, Model (b) was used for tests up to 40 day and Model (c) for the remaining tests.

For all the damaged coating zones, two time constants can be clearly observed in the phase-frequency diagram and Model (d) was thus used to fit the test data. While Model (b) was applicable for the intact coating zone when the solution has penetrated through the channel in the coating and is in contact with the substrate steel, Model (d) is more appropriate for the damaged-coating zone since the coating layer becomes thinner and the solution can penetrate the coating easily. The electrochemical reactivity occurred uniformly on the damaged coating surface.

Figure 3.24 shows the changes of pore resistance R_c and capacitance CPE_c of intact coatings. In general, the pore resistance measures the ease of electrolyte penetration into the coating, which is related to the number and distribution of open pores and pinholes in the enamel coating. The coating capacitance also indicates the extent of electrolyte diffusion into the coating, which is associated with the thickness and dielectric property of the coating. The R_c value of the sample tested under -1.15 V/SCE decreased from 57.6 GΩ cm^2 to 4.92 GΩ cm^2 while the R_c value of the samples tested under -0.85V/SCE and the OCP decreased more rapidly from 20.9 MΩ cm^2 to 1.57 MΩ cm^2 over 70 days. The coating capacitance of all the samples increased with immersion time since the electrolyte solution gradually penetrated the coating, thus increasing the coating capacitance. All the samples tested under the CP have larger coating resistances than the samples under the OCP. Thus, the CP improved the coating performance [14]. The sample tested under -1.15 V/SCE has a larger coating resistance and smaller coating capacitance than its respective values of the sample under -0.85 V/SCE. This result indicates that the higher cathodic potential used in tests does not adversely affect the coating property; it can decelerate the degradation process of the coating.

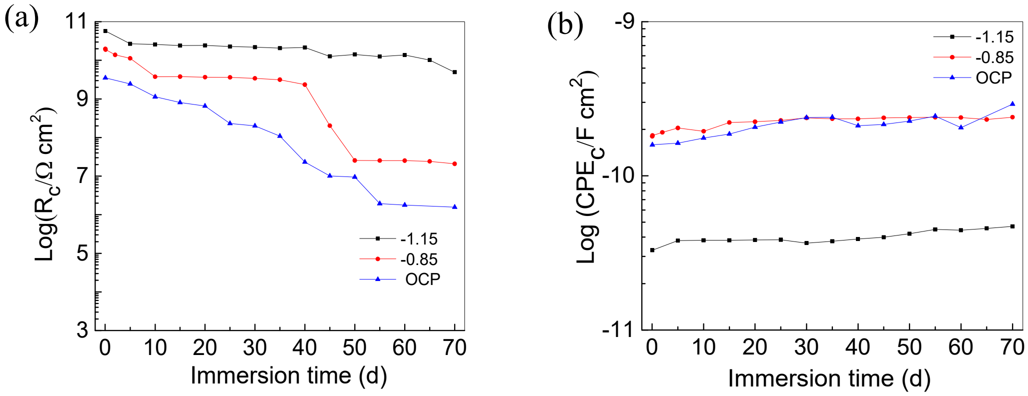

Figure 3.24 Properties of intact coating under various CP levels: (a) pore resistance R_c and (b) capacitance CPE_c

The R_c values of the damaged coating decreased rapidly over immersion time in days (d). Specifically, the R_c value of the samples under the CP dropped from approximately 400 Ω cm^2 to 150 Ω cm^2 while the R_c value of the sample under the OCP reduced more dramatically from 500 Ω cm^2 in one day to 110 Ω cm^2 in 10 days, indicating the failure of coating in protecting the substrate steel. The CPE_c values of all the tested samples reached nearly the same value of 2 mF· cm^2 after four days of immersion. Therefore, after coating has damaged, the CP has little effect on the coating performance.

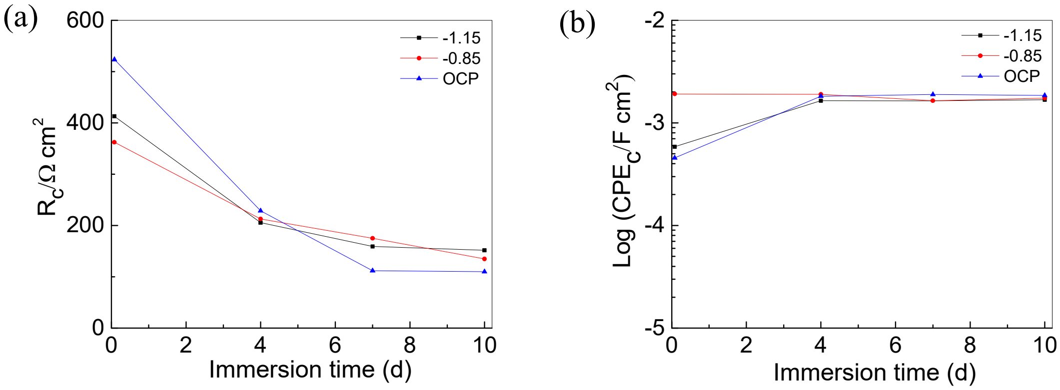

Figure 3.25 Damaged coating properties: (a) pore resistance R_c and (b) capacitance CPE_c

Figure 3.26 displays the properties of the steel-electrolyte interface under intact coating: charge transfer resistance R_{ct} and double layer capacitance CPE_{dl}. The charge transfer resistance is the resistance against electrons transferring across the steel surface, which is inversely proportional to the corrosion rate [10]. For the samples tested under -1.15 V/SCE, -0.85V/SCE and the OCP, the charge transfer resistances were reduced to 1.13 GΩ cm^2, 0.7 GΩ cm^2, and 0.14 GΩ cm^2, respectively, at the end of tests in 70 days. This comparison indicated an increasing electrochemical reaction on the steel-electrolyte interface over time when the level of CP decreased. The double layer capacitance CPE_{dl} is also a measure of the ease of charge transfer across the steel-electrolyte interface. The CPE_{dl} of the samples tested under -1.15 V/SCE, -0.85V/SCE and the OCP were increased to 6.523×10^{-11} F cm^{-2}, 1.613×10^{-10} F cm^{-2}, and 4.314×10^{-10} F cm^{-2}, respectively, at the end of tests in 70 days. The sample tested under -1.15 V/SCE has the highest charge transfer resistance and the lowest double layer capacitance. Thus, the higher the cathodic potential, more effectively the electrochemical reactions can be delayed at the steel-electrolyte interface [14].

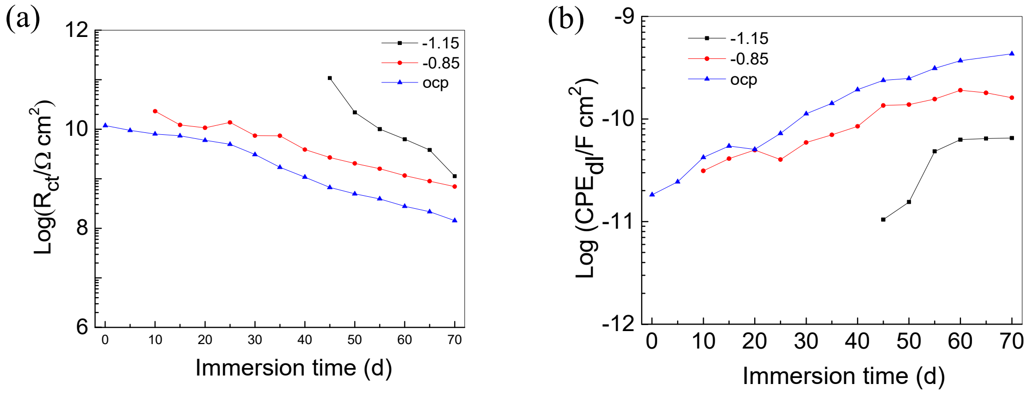

Figure 3.26 Properties of the steel-electrolyte interface under intact enamel coating: (a) charge transfer resistance R_{ct} and (b) double layer capacitance CPE_{dl}

After enamel coating was damaged, the charge transfer resistances of the samples tested under -1.15 V/SCE , -0.85V/SCE and the OCP slightly decreased to 4.96×10^5 Ω cm^2, 3.78×10^5 Ω cm^2, and 6.67×10^4 Ω cm^2 after 10 days of immersion, respectively, which is about 10^4 times smaller than that of the intact coating tested after 70 days of immersion. The double layer capacitances of the samples tested under -1.15 V/SCE, -0.85V/SCE and the OCP also changed slightly, which are 1.37×10^{-4} F cm^{-2}, 6.08×10^{-4} F cm^{-2}, and 5.48×10^{-4} F cm^{-2} after 10 days of immersion, respectively. They are approximately 10^6 times larger than those of the samples with intact enamel coating tested after 70 days of immersion.

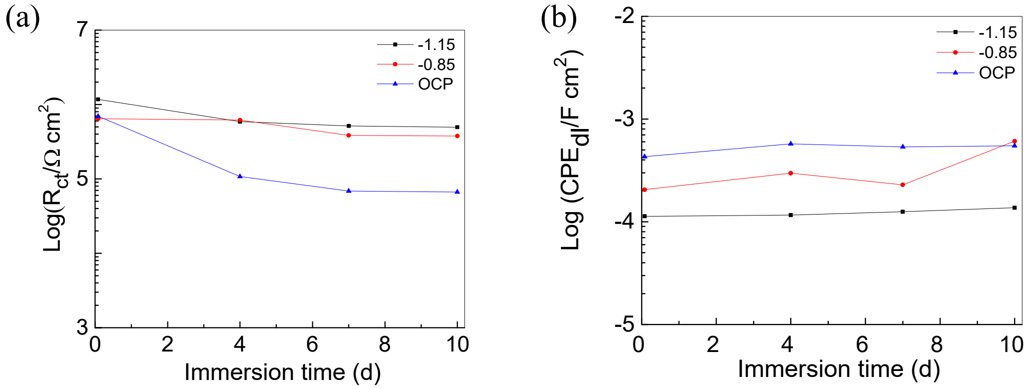

Figure 3.27 Properties of the steel-electrolyte interface under damaged enamel coating: (a) charge transfer resistance R_{ct} and (b) double layer capacitance CPE_{dl}

2.3.2.2 Potentiostatic

Figure 3.28(a) shows the variation of current taken from the intact enamel coating zone under -0.85 vs. SCE/V and -1.15 vs. SCE/V. Each dot represents one measurement data per day until the end of tests in 70 days. The current fluctuated around -0.2 nA from the beginning to 45 days of immersion for both samples. Then, the sample tested under -1.15 V/SCE decreased slowly to approximately -0.3 nA at the end of tests while the sample tested under -0.85 V/SCE decreased dramatically to approximately -0.8 nA at the end. Similarly, Figure 3.28(b) presents the variation of current on two samples with the damaged enamel coating. The currents of both samples reached approximately -5 µA after 10 days of immersion, which is about 10^4 times larger than those of the respective tested samples with the intact enamel coating as more electrochemically reactive spots are generated. In all test cases, the measured current is always negative, implying that the CP current can flow through the coating along electrolyte pathways to reach the metal substrate and protect the steel from corrosion [36].

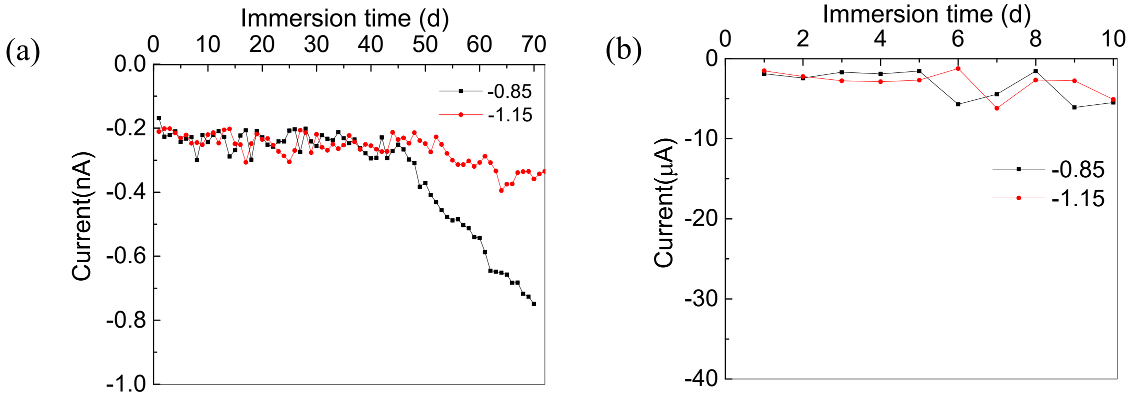

Figure 3.28 Variation of current applied on various samples under -0.85 vs. SCE/V and -1.15 vs. SCE/V: (a) intact coating zone and (b) damaged coating zone

2.3.3 Visual observations after corrosion tests

At the conclusion of corrosion tests, the damaged spots of all tested samples were examined visually. No corrosion products were observed on the damaged surface under the cathodic potential of -1.15V/SCE. Brown corrosion products can be clearly seen on the damage point of the samples tested under the OCP.

Figure 3.29 Damaged surface conditions of the samples tested under (a) -1.15 vs. SCE/V, (b) -0.85 vs. SCE/V and (c) the OCP after corrosion tests

2.3.4 Conclusions

Based on the experimental results and analysis from one representative sample in each test condition, the following conclusions can be drawn:

1. Enamel residuals remained between anchor points of the substrate steel after the enamel coating had been chipped off due to impact loading. During all the corrosion tests, no further delamination was found, and the CP did not change the coating properties and the mechanical condition at the coating-substrate interface.
2. At the intact coating areas, the higher potential (up to -1.15 V/SCE) applied in CP, the higher the coating resistance and charge transfer resistance. The CP does not cause debonding between the coating and its steel substrate, decelerates the degradation process of the coating and delay the electrochemical reactions at the steel-electrolyte interface.
3. The resistances of all the damaged coatings are less than 1 kΩ cm^2, indicating the loss of their barrier effect in protecting the substrate steel from corrosion. The introduction of CP does not improve the coating performance once damaged.
4. The resistances against electrolyte penetration into the enamel coating and charge transfer through the steel-electrolyte interface in the intact and damaged enamel coating areas differed by at least 10^4 times after 70 days of tests. It is thus important to separate the electrochemical processes in the intact and damaged zones during corrosion tests.

VI. Task 4 System performance of in-situ enamel-coated pipelines – stress distribution and stress corrosion cracking

1. Experimental Program

The commercial software ABAQUS was used to establish a finite element model of steel samples and their enamel coating process. The model was used to understand the effect of coating process on initial stress, and simulate the stress distribution under thermal, external and internal pressure.

The phase of the as-received steel and the steel fired at 840 °C for two hours are examined using the XRD. The potentiodynamic tests of X65 steel were conducted in the simulated alkaline soil solution at a scan rate of 50 mV/s and 0.5 mV/s, respectively, to investigate the electrochemical polarization on the occurrence of stress corrosion cracking (SCC). The working area of the electrode was 1.0 cm^2. A saturated calomel electrode (SCE) was used as the reference electrode and a Pt plate as a counter electrode.

Slow strain rate tests (SSRT) were carried out on smooth cylindrical tensile samples inside the autoclave as shown in Figure 4.1. The coupon samples were machined according to the ASTM E8 Standard. The sample surface in the gauge section was polished up to 1200 grit finish in an orientation parallel to the subsequent loading direction of the SSRT. This ensured similar surface conditions for all tests. The INSTRON tensile machine 5965 was used to perform the SSRT at a strain rate of 0.000254 mm/s. All the tests were carried out at room temperature. After each test was completed, the fracture sample was immediately removed and cleansed using acetone for SEM examination.

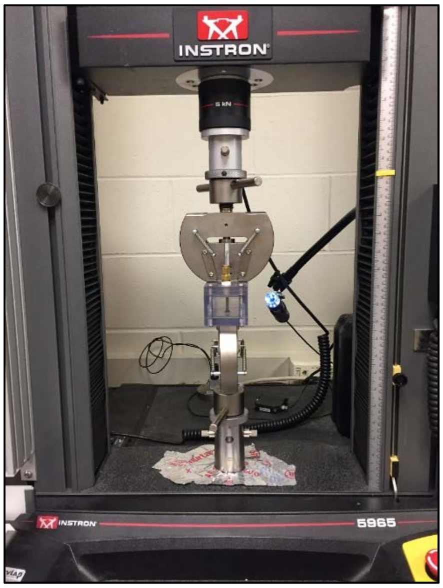

Figure.4.1 Glass autoclave and INSTRON tensile instrument used to perform the SSRT with the NS4 solution

The electrochemical tests were performed with an Interface1000E Potentiostat (Gamry Instrument). A standard three-electrode system was used with a cylindrical tensile sample of X52 steel as the working electrode, a platinum sheet as the counter electrode, and Ag/AgCl electrode as the reference electrode. The electrochemical impedance spectroscopy (EIS) measurements were taken in NS4 solution at different impressed potentials. In all EIS tests, a sinusoidal wave of potential (10 mV in amplitude) with a frequency of 0.01 Hz to 10 kHz was used. Ten points per decade (sampling rate) were recorded. The EIS were obtained after stationary conditions have been reached and measurements continued till the failure of each SSRT test. The fracture surfaces of the coupons tested in air and at different cathodic potentials were examined with scanning electron microscopy (SEM) to study the SCC susceptibility.

2. Results and Discussion

2.1 Residual Thermal Stress

Enamel bonds to the substrate steel by thermal fusion at a temperature of 830 °C for 10 minutes. The commercial software ABAQUS was used to simulate the coating process that can be divided into firing process and cooling process. During the firing process, enamel powder dry-sprayed on steel will not chemically react with steel until the powders behave as viscous fluids at 830 °C. Hence, the powders will not affect the thermal deformation of the steel substrate. During the cooling process, residual thermal stress is generated between the enamel and steel due to the mismatch of the thermal expansion coefficients. Since the thermal expansion coefficient of enamel is smaller than that of steel, the enamel will be in compression and the steel will be in tension when the temperature cools to 25 °C.

2.1.1 Modelling process from finite element analysis

In the firing process analysis, the steel without any coating was linearly heated from a room temperature (25 °C) to 830 °C for 26s. The enamel-coating layer was then created on the thermally deformed model, and the model with this new coating layer was again cooled at a uniform rate for 26s. The identical temperature conditions were imposed on all nodes of the FE models. Figures 4.2 and 4.3 show the properties of steel substrate and enamel coating.

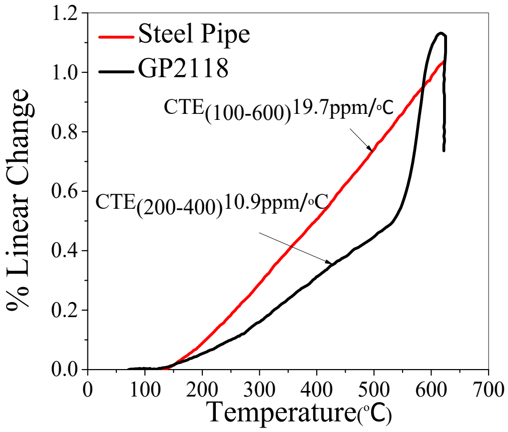

Figure 4.2 Coefficients of thermal expansion of enamel and steel

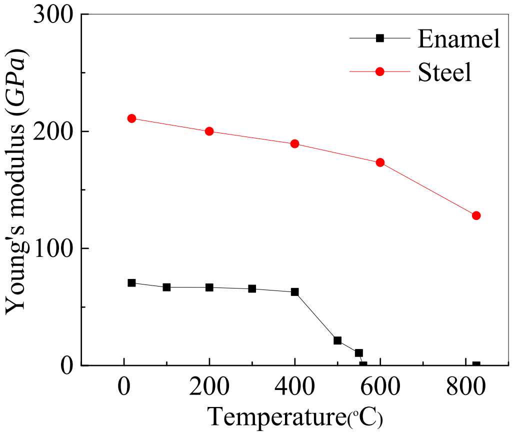

Figure 4.3 Young's modulus of enamel coating and steel at elevated temperature

Porcelain enamel is coated inside the steel pipe. The pipe has an outside diameter of 323.850 mm and a thickness of 9.525 mm. The length of the pipe is 3 m. Three-dimensional hexahedral eight-node (C3D8R) elements were used in this simulation. It is assumed that enamel powder was attached to its substrate steel with no stress until the powder was melted, cooled, and perfectly bonded to the steel. The enamel does not have any stress in itself after the glass softening temperature of 550 °C because its behavior is similar to that of a viscous fluid. Its elastic modulus above 550°C is defined as approaching 0. In the model, the coating thicknesses were set as 100 µm, 200 µm, and 400 µm in order to study the effect of coating thickness on the thermal residual stress in the coating. Besides, three mesh sizes (0.02, 0.03, and 0.04 m) were used to study the influence of mesh size to the coating thermal residual stress. Figure 4.4 shows the mesh model of a steel pipe internally coated with enamel. After simulation, minimum principal stress of the enamel coating will be checked to study the thermal residual stress.

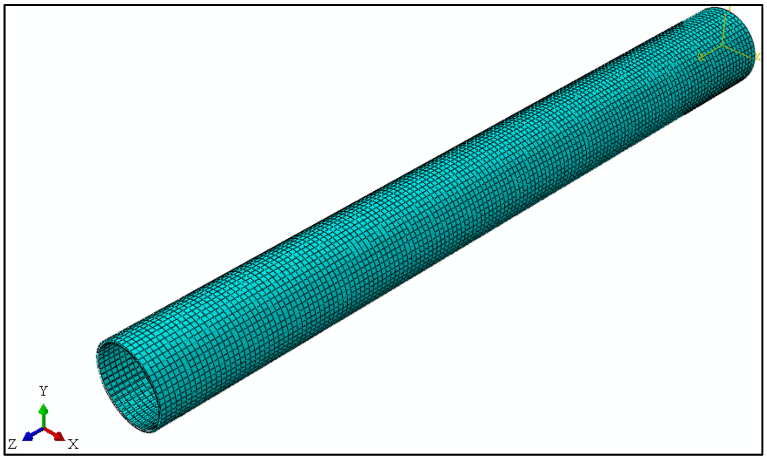

Figure 4.4 ABAQUS mesh model of a steel pipe internally coated with enamel

2.1.2 Prediction from finite element analysis

Table 4.1 shows a summary of the largest value of minimum principal stress of internal enamel coating layer. Figure 4.5 to Figure 4.13 show the minimum principal stress of internal enamel coating with different mesh size and coating thickness. Overall, the minimum principal stress is approximately 2.5 MPa. The enamel coating thickness and element size do not have significant influence on the residual stress.

Table 4.1 The minimum principal stress (MPa) of internal enamel coating layer

Element size (m) Coating thickness (μm)	0.04	0.03	0.02
100	-2.55	-2.46	-2.46
200	-2.51	-2.47	-2.48
400	-2.49	-2.49	-2.50

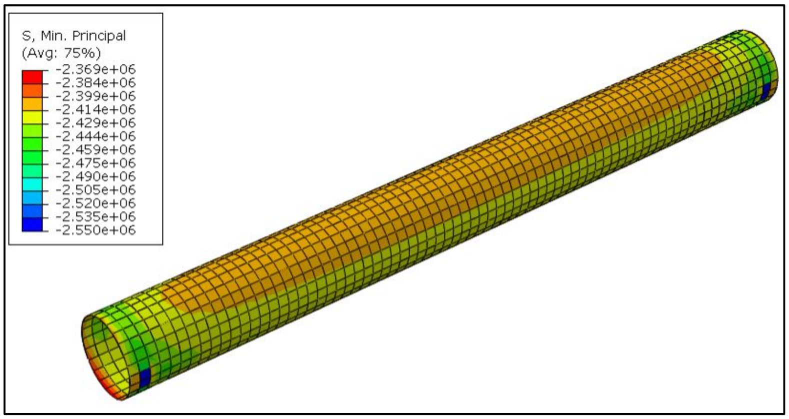

Figure 4.5 Minimum principal stress of internal enamel coating with a mesh size of 0.04 m and a coating thickness of 100 μm

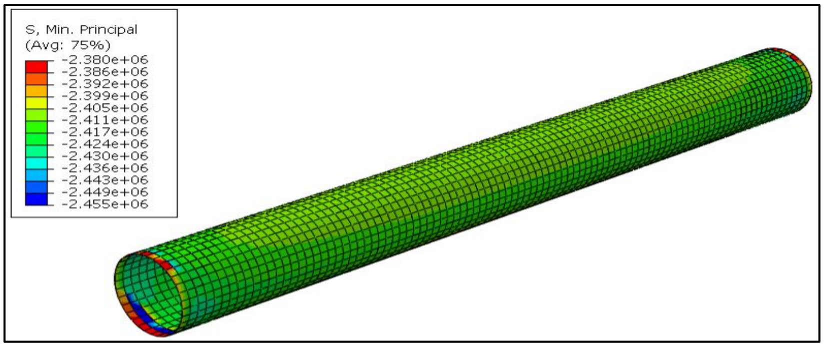

Figure 4.6 Minimum principal stress of internal enamel coating with a mesh size of 0.03 m and a coating thickness of 100 µm

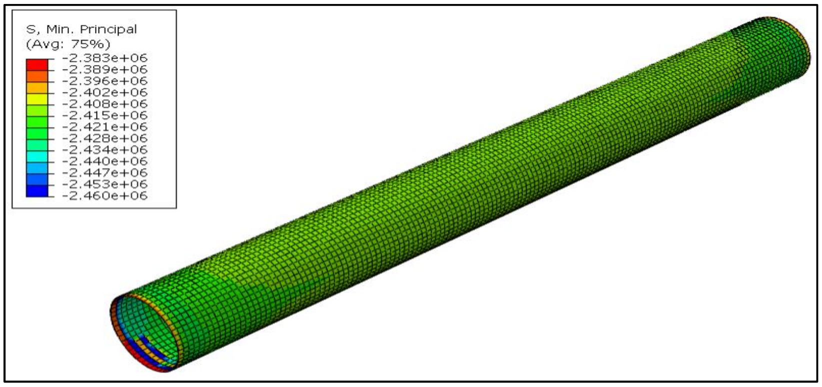

Figure 4.7 Minimum principal stress of internal enamel coating with a mesh size of 0.02 m and a coating thickness of 100 µm

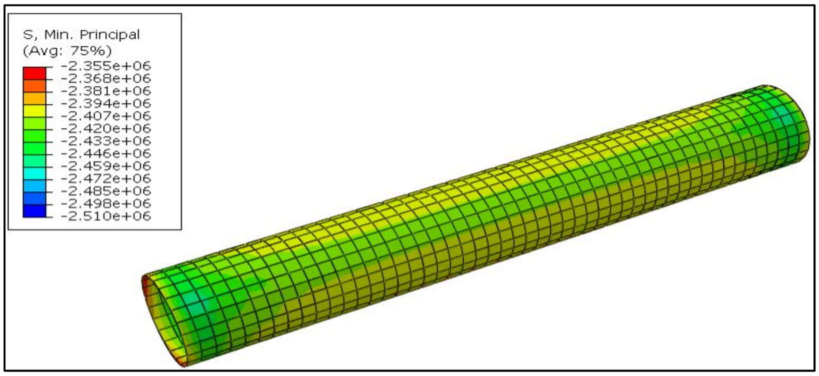

Figure 4.8 Minimum principal stress of internal enamel coating with a mesh size 0.04 m and a coating thickness of 200 µm

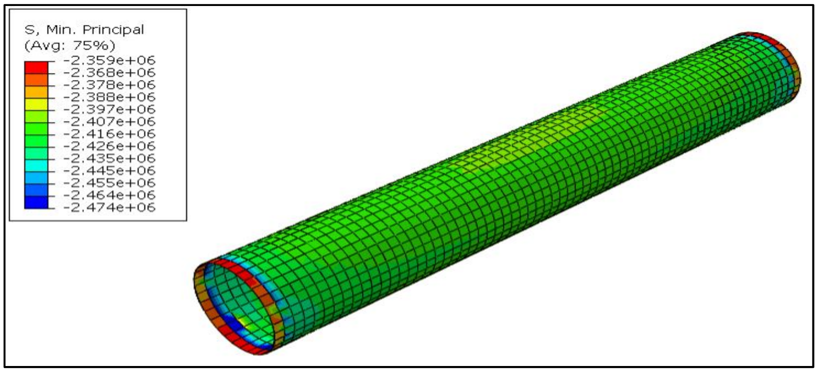

Figure 4.9 Minimum principal stress of internal enamel coating with a mesh size of 0.03 m and a coating thickness of 200 µm

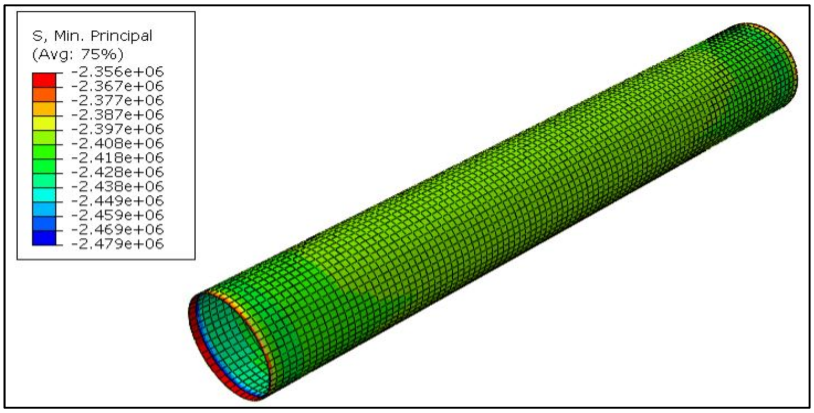

Figure 4.10 Minimum principal stress of internal enamel coating with a mesh size of 0.02 m and a coating thickness of 200 µm

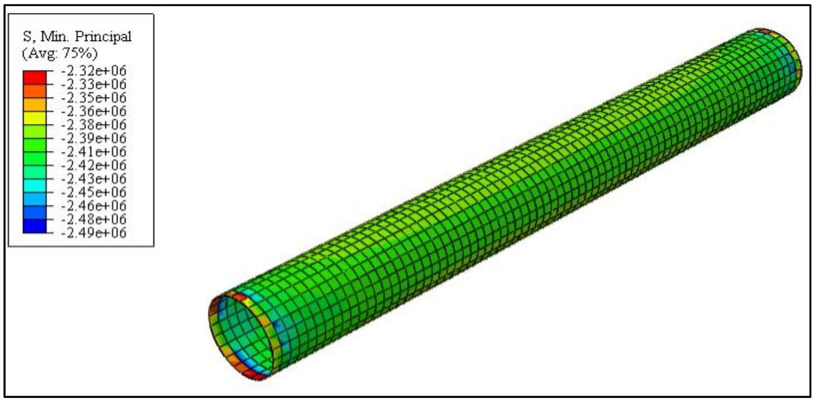

Figure 4.11 Minimum principal stress of internal enamel coating with a mesh size of 0.04 m and a coating thickness of 400 µm

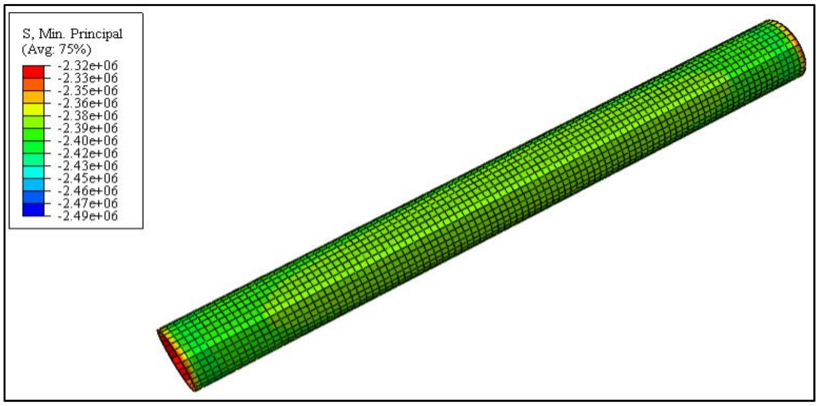

Figure 4.12 Minimum principal stress of internal enamel coating with a mesh size of 0.03 m and a coating thickness of 200 μm

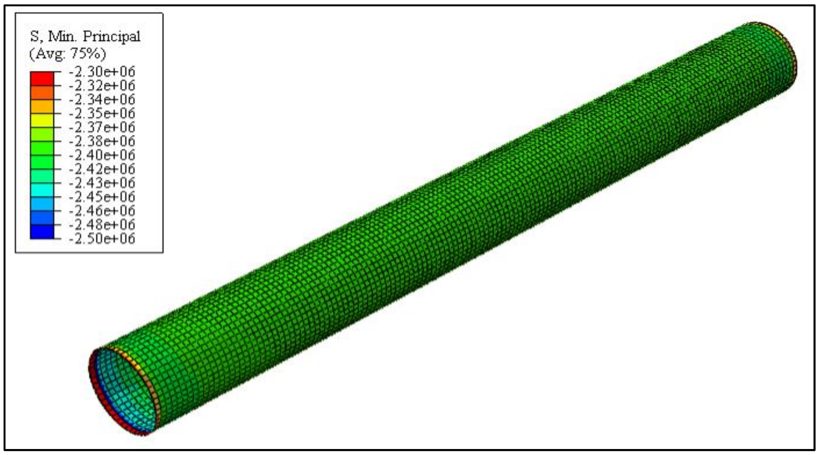

Figure 4.13 Minimum principal stress of internal enamel coating with a mesh size of 0.02 m and a coating thickness of 400 μm

The minimum principal stress represents the thermal residual stress in the coating. The stress distributes uniformly along the longitudinal direction of the steel pipe except at both ends of the pipe. As the stress is so small, the enamel coating layer does not have any effect on the steel. Steel deforms little during the enameling process since steel is much thicker than coating. Thermal heat can be conducted quickly to the surrounding area. Based on the previous pull-off test, the bond strength between the coating and the steel ranged from 16.12 MPa to 18.73 MPa. The maximum thermal residual stress is 2.55 MPa, which is much smaller than that of the chemical adhesion between the enamel and steel. Thus, the coating will not delaminate from the substrate during enameling process.

2.2 Stress Distribution on a Pipe Containing a Corrosion Defect

Residual thermal stress exists in the enamel-coated steel pipe. Enamel is in compression and the steel is in tension due to the mismatch of the thermal expansion coefficient. Besides, an existing underground pipeline is subjected to soil induced strain due to ground movement. During operation, the internal pressures of the pipe are usually 15, 20 or 25 MPa, which are 46, 62 and 77% of the specified minimum yielding strength (SMYS), respectively [37]. Besides, due to corrosion or other reasons, thin wall of the existing pipeline is sometimes uneven and not smooth prior to enamel coating. In this case, the stress concentration may occur around various dents. Therefore, the stress concentration of the overall pipeline under residual thermal stress, internal pressure and external pressure is studied.

2.2.1 Modelling process from finite element analysis

In this model, the coating thickness and the mesh size were set to be 200 μm and 0.02 m, respectively. The corrosion defect is 90 mm long and 1.191 mm deep. The internal pressures of the pipe were set to be 0, 5, 10, 15, 20 and 25 MPa. A 0.2% tensile and compressive strain was applied on pipe along the longitudinal direction to simulate the soil-induced strain due to ground movement, which usually ranges from 0 to 2.5%. Figure 4.14 is the mesh model of steel pipe internally coated with enamel. After simulation, von Mises stress at the corrosion defect of the pipe will be checked to understand the level of stress concentration.

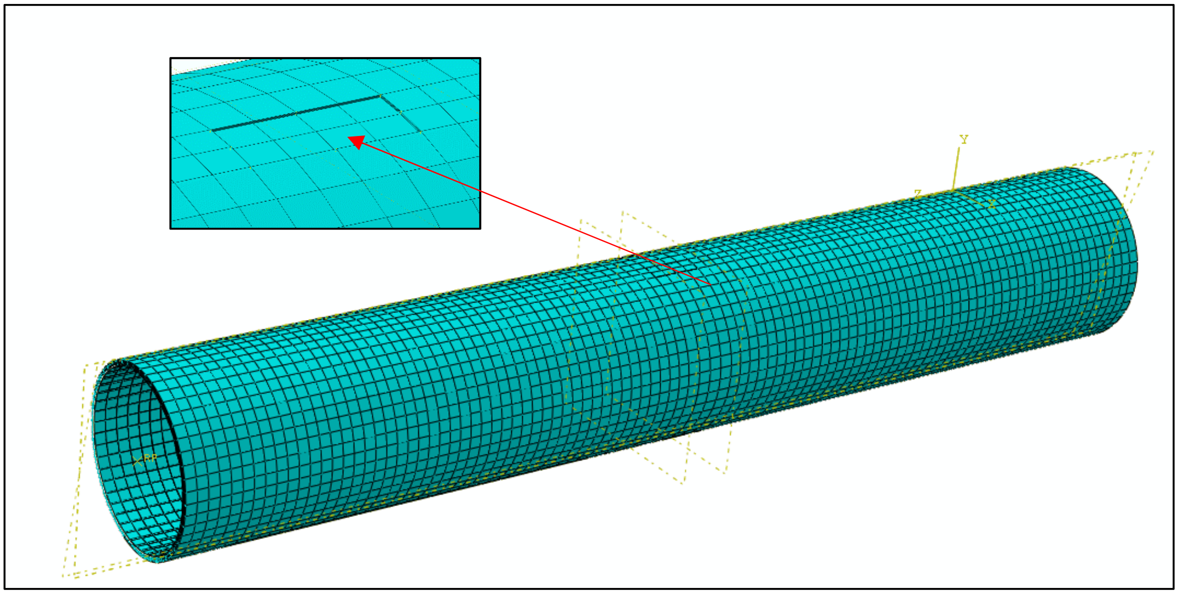

Figure 4.14 ABAQUS mesh model of steel pipe with corrosion defect

2.2.2 Prediction from finite element analysis

Figure 4.15 and Figure 4.16 show the stress distribution simulated by the finite element model on the steel pipe containing a corrosion defect under a synergistic effect of thermal stress, external soil strain, and internal pressure. It can be seen that the stress distribution around the corrosion defect is not uniform. The propagation of the stress distribution along the longitudinal direction is different from that along the circumferential direction. The highest stress concentration is at the center of the corrosion defect as the internal stress is applied. The stress concentration is 0 when the internal pressure is 0, and increases with the increase of the internal pressure regardless whether the external soil strain is in tension or compression. This stress concentration may result in a rapid fracture if the local stress exceeds the material strength.

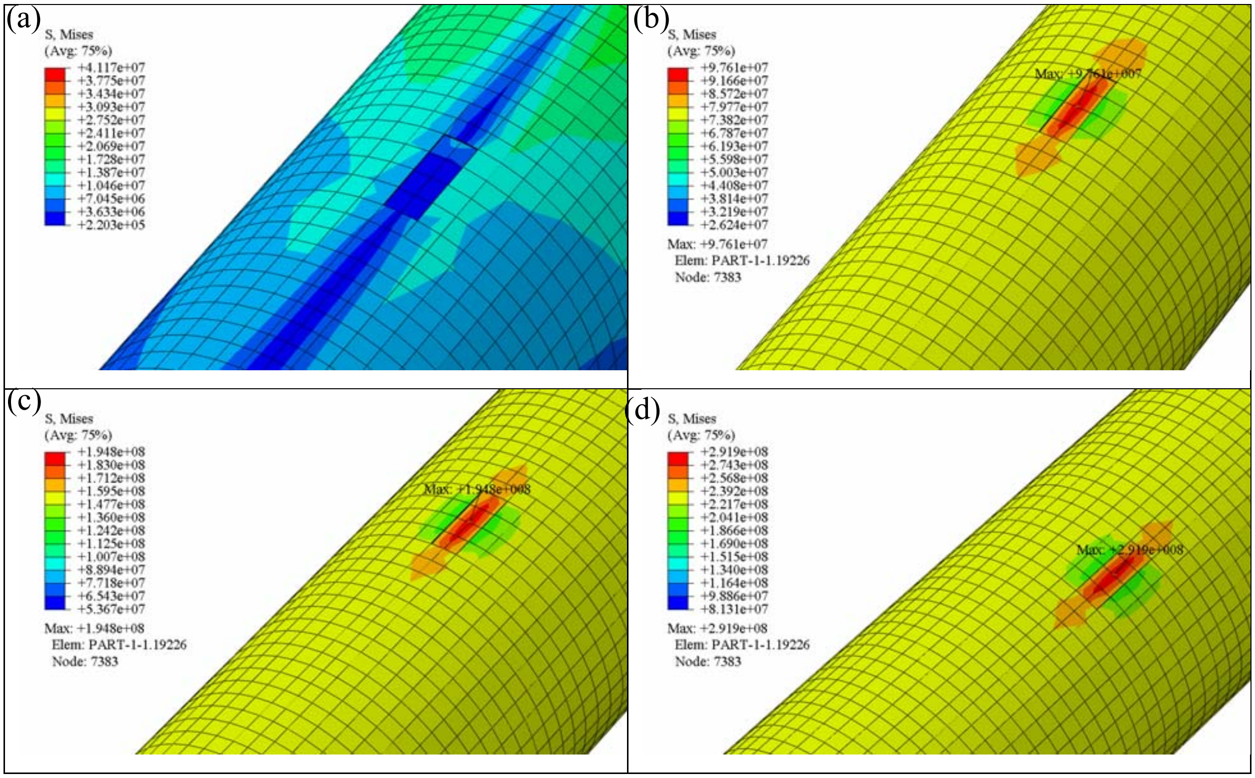

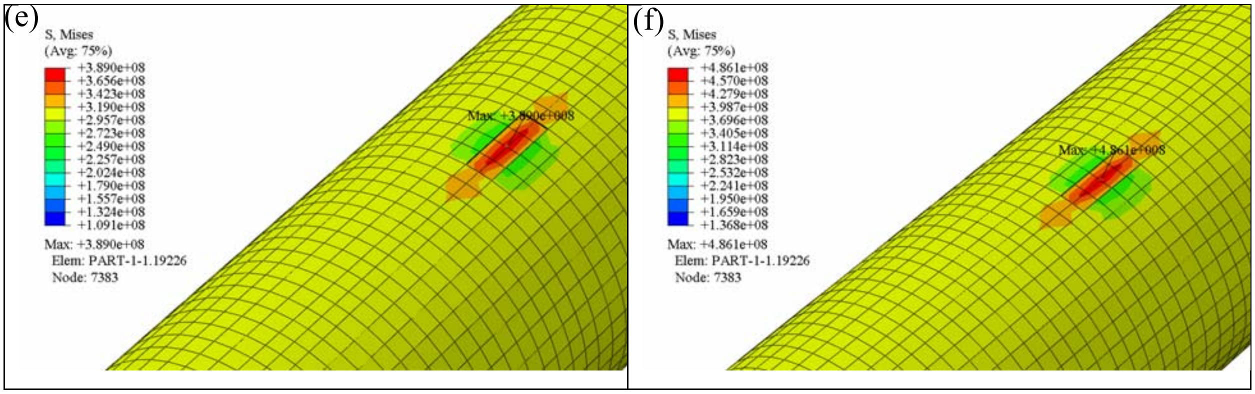

Figure 4.15 Distribution of stress on the steel pipe with a corrosion defect with compression soil strain of 0.2% and various local internal pressure 0, 5, 10, 15, 20 and 25 MPa for (a) to (f)

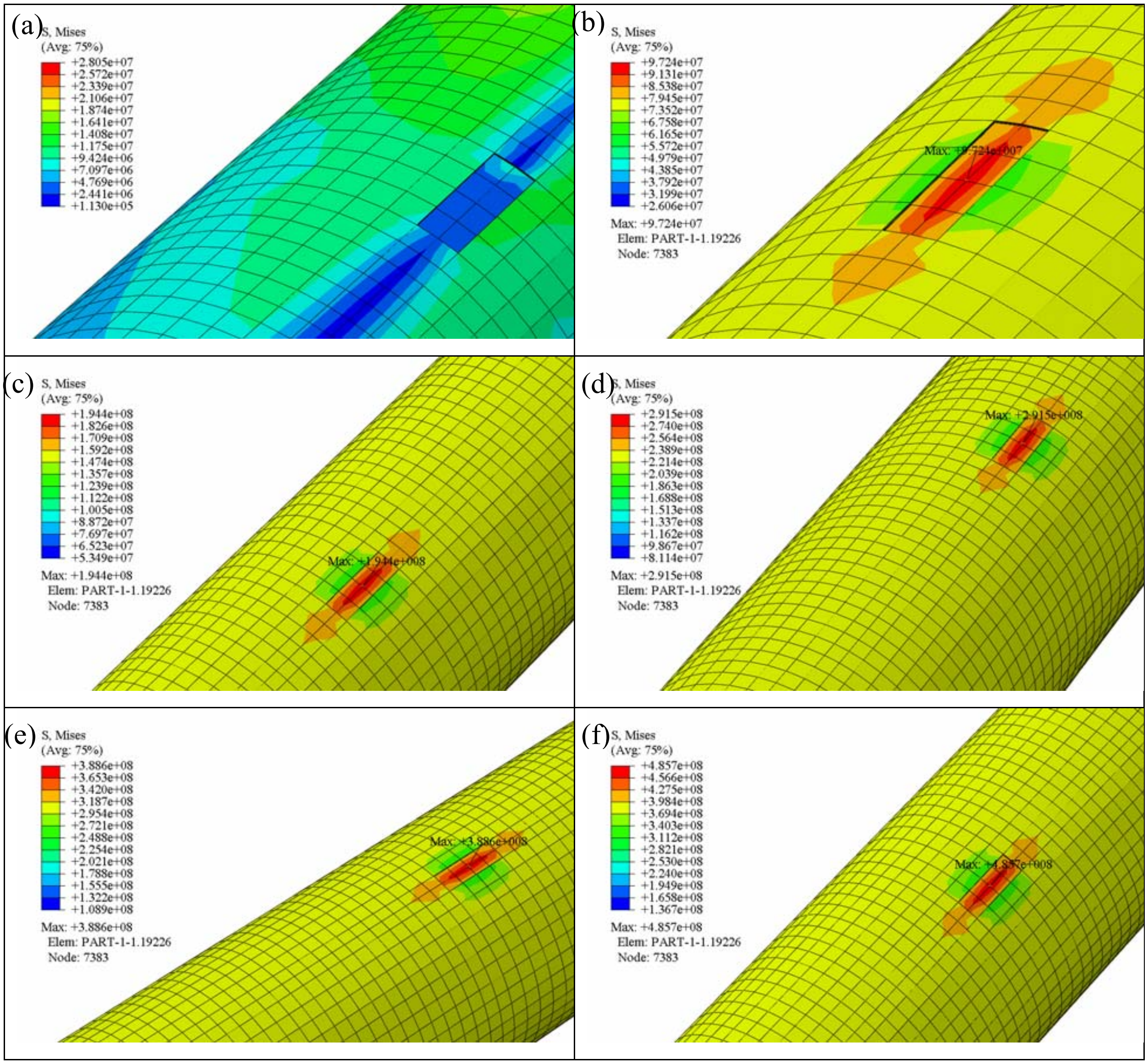

Figure 4.16 Distribution of stress on the steel pipe with a corrosion defect with tensile soil strain of 0.2% and various local internal pressure 0, 5, 10, 15, 20 and 25 MPa for (a) to (f)

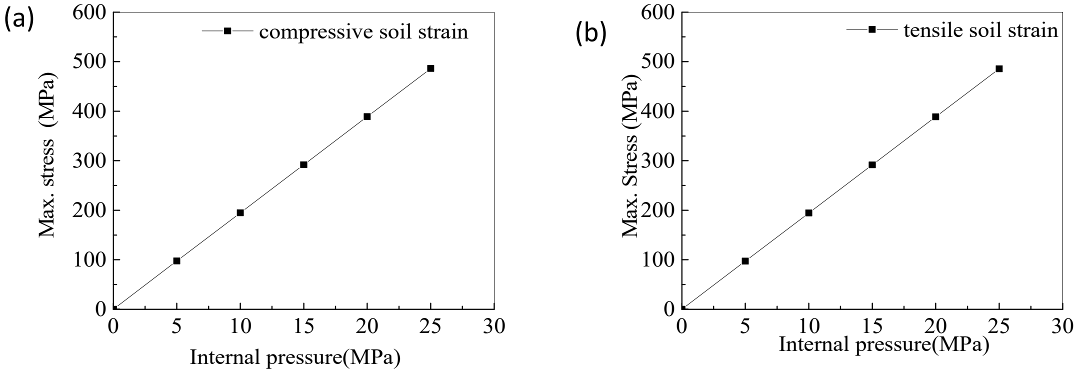

Figure 4.17 Max stress of the steel pipe as a function of internal pressure

The internal pressure has a large impact on the stress concentration. With the increase of internal pressure, the stress concentration increases linearly to around 480 Pa at the internal pressure of 25 MPa, which is close to the yield strength of the pipe steel. Further increase in internal pressure will put the pipe into the plastic stage and later may induce cracking at the corrosion defects. The stress concentration at the corrosion defect can contribute to stress corrosion cracking even in mildly corrosive environment, which can lead to unexpected sudden failure of steel pipe during operation.

2.3 Stress Corrosion Cracking

Stress corrosion cracking (SCC) is a cracking process of susceptible metals under a simultaneous action of corrosive environment and sufficient tensile stress. It poses a threat to the safe operation of pipelines and has, since 1965, contributed to major failures in pipelines around the world. The buried pipelines have generally experienced two main forms of SCC: high-pH and near-neutral pH SCC. High-pH SCC developed in a high-pH carbonate-bicarbonate electrolyte under a disbonded coating due to the CP (cathodic polarization)-driven cathodic reduction of water and the generation of hydroxyl ions. At the early stage of coating disbondment, corrosion pits initiated due to the presence of Cl^-, which prevents the formation of stable passivation and increases the anodic sensitivity of steel. The corrosion pits increase the stress concentration, which facilitates the transformation from pits to cracks. Then the stress will concentrate at the crack tips, rupture the passive film over the crack tips and activate dislocation to form slip bands or dislocation pile-ups, which significantly promotes crack propagation.

Nearly neutral-pH SCC of pipelines develops in anaerobic, diluted groundwater containing primarily bicarbonate ions due to ineffective CP to the pipe surface. SCC colonies are initiated on the outside surface with pitting due to the fluctuation of cathodic potential. The fluctuation results in a temporary anodic potential field and leads to anodic dissolution at local defects, thus initiating the corrosion pits. During SCC, the crack tips have always been close to fresh, bare steel while the crack wall is covered with a corrosion products layer, which enhances the anodic dissolution and hydrogen evolution. A critical hydrogen concentration results in steel embrittlement and promotes crack propagation.

Cathodic protection applied to the pipeline surface is a factor that influences the SCC mechanism. More internal cracks were seen in the steel with the highest level of cathodic protection applied, contributing to cracking associated with the so-called hydrogen embrittlement effect. The aim of this work is to evaluate the effect of cathodic polarization on the SCC of API X65 pipeline steel in terms of mechanical and electrochemical behavior in a simulated soil environment with a pH of 10 at room temperature. Relation between the mechanical properties and susceptibility to SCC is studied.

2.3.1 XRD

API 5L X65 pipe steel was used in this study. The pipe has an external diameter of 323.850 mm and wall thickness of 9.525 mm. As shown in Figure 4.18, both the as-received steel and the steel fired at 840 °C for two hours have the same ferrite microstructure based on the XRD test results.

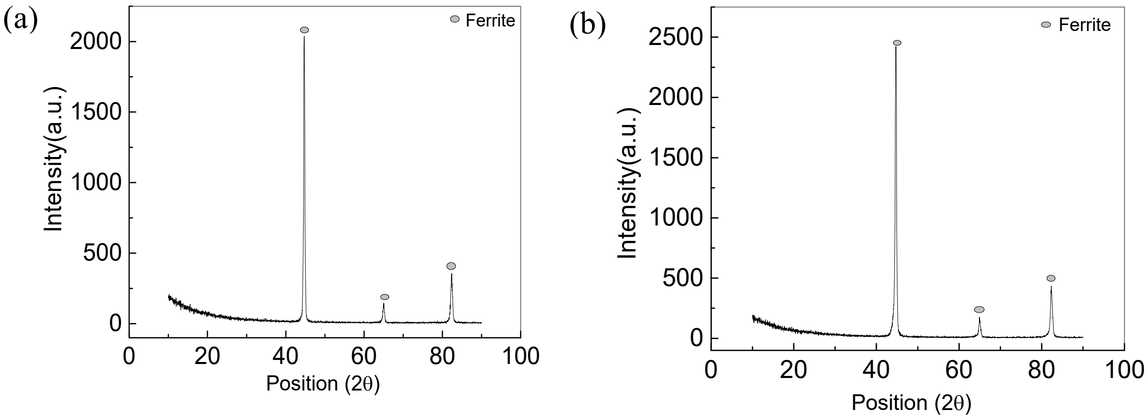

Figure 4.18 XRD patterns for (a) as-received steel and (b) the steel fired at 840 °C for two hours

2.3.2 Potentiodynamic test

Figure 4.19 compares the two polarization curves measured at fast and slow scanning rate. It can be seen from Figure 4.19 that the null-current positions divide the potential range into three zones. The so-called anodic reaction dominates Zone I (> -0.75V), the cathodic reaction dominates Zone III (< -0.833 V), and both the anodic and cathodic reactions co-exist in Zone II (-0.75 V ~ -0.833V). The open circuit potential was measured to be approximately -0.68 V, which falls in Zone I. The cathodic potentials chosen for slow strain rate tests are -0.79 V/SCE in Zone II, and -0.90 V/SCE and -1.20 V/SCE in Zone III.

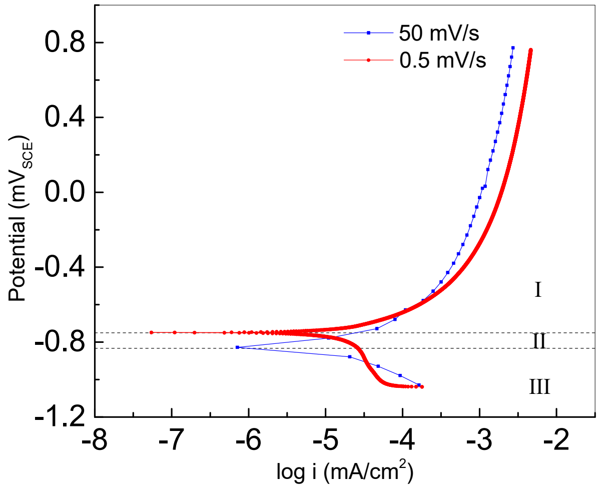

Figure 4.19 Polarization curves of the steel measured at high (50 mV/s) and low (0.5 mV/s) potential scanning rates in NS4 solution

2.3.3 Slow strain rate (SSR) test

A simulated ground water solution (NS4) with pH 7 was used to simulate a corrosive environment. Table 4.2 shows the chemical composition of the NS4 solution used in this study.

Table 4.2 Chemical composition of the NS4 solution (g/l)

$NaHCO_3$	$CaCl_2 \cdot H_2O$	$MgSO_4 \cdot 7H_2O$	KCl
0.483	0.181	0.131	0.122

Figure 4.20 shows the stress-strain curves of X65 steel obtained from the SSR tests with different applied potentials in alkaline soil solution. Table 3 shows a summary of the mechanical properties related to the SCC susceptibility.

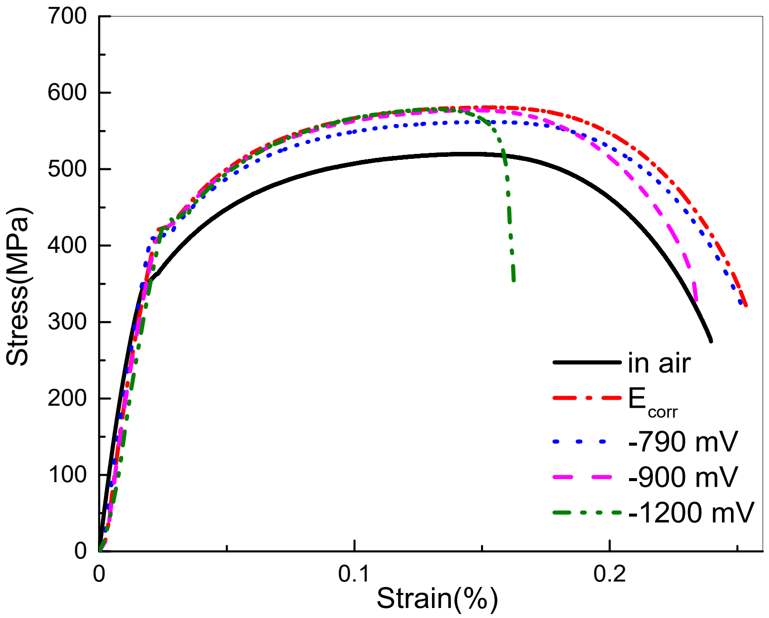

Figure 4.20 Stress vs. strain curves obtained from SSR tests

Table 4.3 Summary of the mechanical properties obtained from SSR tests

Condition	Yield strength (YS) (MPa)	Ultimate strength (US) (MPa)	Plastic elongation (mm)	Plastic strain (%)	Time to failure (s)
in Air	351	520	3.63	0.20	44340
OCP	421	581	4.26	0.23	47040
-0.79 V	411	562	4.25	0.23	46830
-0.90 V	419	577	3.89	0.21	43305
-1.20 V	417	578	2.51	0.14	30045

When the coupon samples were tested in the solution, both the yield strength and the ultimate strength increased. The yield strength and ultimate strength of the sample tested under the open circuit potential (OCP) are higher than those of the sample tested in air. An obvious passive film is observed on the surface of the sample tested under the open circuit potential. Such a passive film likely delays the initiation of crack on the surface of a coupon sample, thus requiring higher tensile stress to rupture the sample being tested. This result represents the combined action of anodic dissolution at grain boundaries and tensile stress.

The sample tested under OCP has relatively higher yield strength and ultimate strength than those tested under cathodic potentials (CP) because passive films are less likely formed on the surface of the samples tested under cathodic potentials. The enhanced strength of the steel coupon in the alkaline NS4 solution than in air is attributed to the fact that hydrogen atoms penetrate into the steel and block the dislocation movement. The steel sample is thus hardened with reduced ductility.

Since the internal LVDT in the Instron loading frame measures the displacement of crosshead, the plastic elongation of a sample is used to limit the displacement in the shoulders of the sample. The plastic elongation of the sample tested under OCP is close to that under a cathodic potential of -0.79 V. The plastic elongations and times to failure of the samples tested under cathodic potentials decreased as the cathodic potential decreased, indicating more hydrogen embrittlement at the more negative cathodic potential (larger potential value).

Figure 4.21 shows the dependence of change in cross-sectional area on the applied potential of X65 steel in the alkaline NS4 solution. The reduction in cross-sectional area (RA in %) is defined as

$$RA(\%) = \frac{D_I^2 - D_F^2}{D_I^2} \times 100 \tag{4-1}$$

where D_I and D_F represent the initial and final gauge section diameter at the fracture location. When the tensile tests were performed in air, the RA was measured to be 81.8%, which is larger than all the other samples tested in the solution. This indicates that the X65 steel is susceptible to environmentally assisted cracking, depending on the applied potential. The more negative the applied potential, the higher SCC susceptibility of the X65 steel in the simulated solution.

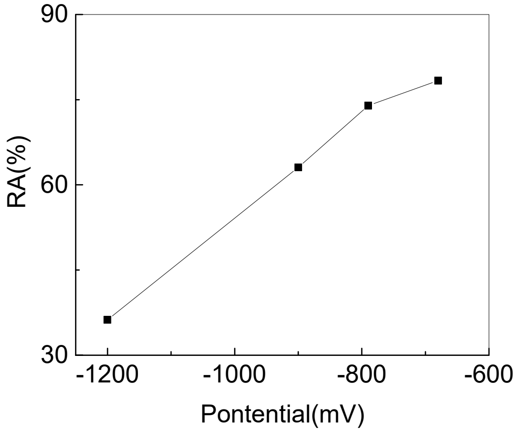

Figure 4.21 Dependence of RA on the applied potential of X65 steel in alkaline NS4 solution

The relationship between the SCC susceptibility of the steel under cathodic potentials and the electrochemical reaction mechanism is presented in Figure 4.22. When the applied potential falls in Zone I, the polarization curves measured at both low and fast scanning rates are within the anodic polarization range, indicating that the cracking process is controlled by the anodic dissolution (AD). When the applied potential falls in Zone III, both polarization curves are in the cathodic polarization range. The cathodic reaction charges hydrogen to the steel, causing embrittlement. Therefore, the SCC is referred to as a hydrogen embrittlement (HE) mechanism. When the applied potential falls in Zone II, the steel is in non-equilibrium state. The steel is in cathodic polarization when the scan rate is low, and in anodic polarization when the scan rate is high. In this case, the SCC is due to a combination of anodic dissolution and hydrogen embrittlement (AD+HE).

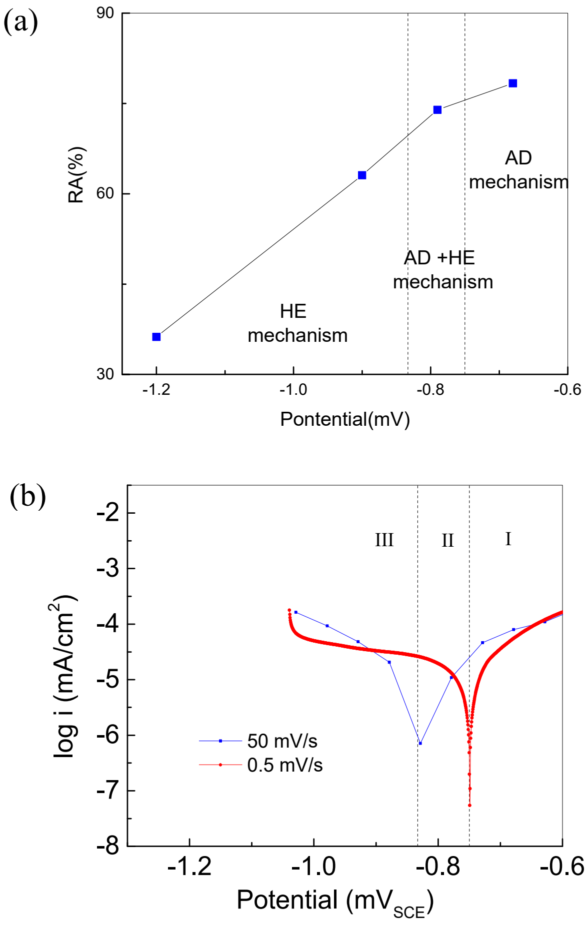

Figure 4.22 SCC susceptibility of the X70 steel in NS4 solution as a function of the cathodic potential (a) and the corresponding polarization curves (b) measured at slow and fast potential scanning rates

2.3.4 EIS test

The corresponding corrosion test results are presented in Figure 4.23. The Nyquist plots of all the tested samples with different potentials applied show different forms of semicircle arcs. The coupon sample surface is assumed to be quasi-stable so that the EIS test was conducted from the beginning to the fracture of the coupon sample. The semicircle arc of the sample tested under OCP increases significantly from 0.7 h to 3.4 h of immersion, and then stabilized till 8.9 h, which is slightly increased afterwards. The radii of semicircle arcs of the samples tested under cathodic potentials of -0.79 V/SCE and -0.90 V/SCE and the sample tested under -1.2 V/SCE are larger than and similar to those under OCP, respectively. The radii of semicircle arcs of all the samples tested under cathodic potentials decrease as the cathodic potentials decreased. Therefore, the cathodic potential can change the corrosion behavior of the pipeline steel.

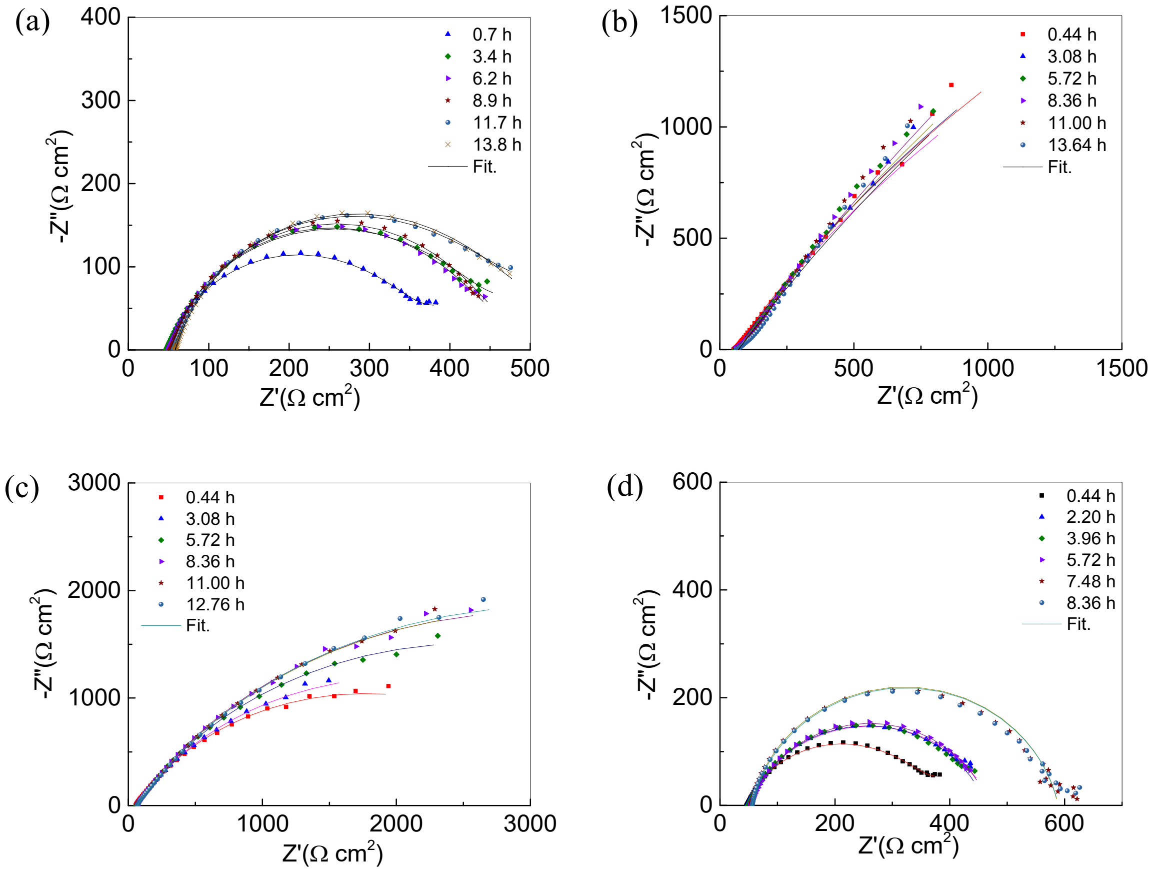

Figure 4.23 Nyquist plots from samples tested under (a) open-circuit potential; (b) a cathodic potential of -0.79 vs. SCE/V; (c) a cathodic potential of -0.90 vs. SCE/V; (d) a cathodic potential of -1.2 vs. SCE/V

The impedance data can be analyzed by fitting them into an equivalent circuit model (EEC). Model $R_s(Q(R_{ct}W))$ and Model $R_s(QR_{ct})$ were used for the samples tested under OCP and CP, respectively. Here, R_s represents the solution resistance and R_{ct} represents the charge transfer resistance at the steel-electrolyte interface. A constant phase element (CPE) representing double layer capacitance was used to replace a pure capacitor because of uneven roughness and a distribution of electrochemical reactivity on the surface of steel. A Warburg impedance W was included in the model to take into account the diffusion behavior, which was induced by the accumulation of corrosion products on the corrosion active sites. Figure 4.23 shows the extracted charge transfer resistance over time. Basically, R_{ct} of all the samples tested under cathodic potentials show a slow increase over time. R_{ct} drops slightly when the cathodic potential decreases from -0.79 V/SCE to -0.9 V/SCE but dramatically from -0.9 V/SCE to -1.2 V/SCE. The charge transfer resistance against electrons transferring across the steel surface is inversely proportional to the corrosion rate. So the sample tested under -0.79 V/SCE has the lowest corrosion rate while the sample tested under -1.2 V/SCE has the highest corrosion rate among all the samples tested under CP. As there is no cathodic protection for the sample tested under OCP, the sample has the highest corrosion rate.

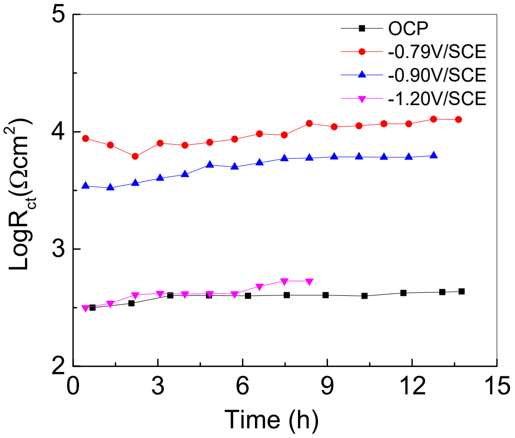

Figure 4.24 Charge transfer resistance over time for different samples tested under various cathodic potentials

2.3.5 Fracture surface morphology

Figure 4.25 shows a suite of SEM images for the understanding of fracture characteristics. The surfaces fractured in air consist of a great number of small dimples and micro-voids. Apparent necking can be observed and there is no cracks on the side wall, which demonstrate totally ductile fracture. For the fracture surfaces of the coupon tested under open circuit potential, dimples and micro-voids can still be observed but corrosion products cover one fracture surface, which means the anodic dissolution dominates the cracking process. Some side wall cracks demonstrate that the coupon is susceptible to SCC. The surfaces fractured under a cathodic potential of -790 mV/SCE still have micro-voids and small dimples that are covered by crystallization of the chemical compositions. A mixture of quasi-cleavage and dimples appeared on the surface so the fracture contains both ductile and brittle fracture. For the coupon tested under a cathodic potential of -900 mV/SCE, the necking is not in the round shape and the fracture surface is uneven and dominated by dimples and river-like cleavage. For the coupon tested under a cathodic potential of -1200 mV/SCE, there is no apparent necking and the fracture is totally cleavage. With the decrease of cathodic potential, the fracture surfaces gradually transform from the ductile to brittle stage. As more hydrogen is generated with the decrease of cathodic potential, the coupons are more prone to suffer from hydrogen-induced embrittlement.

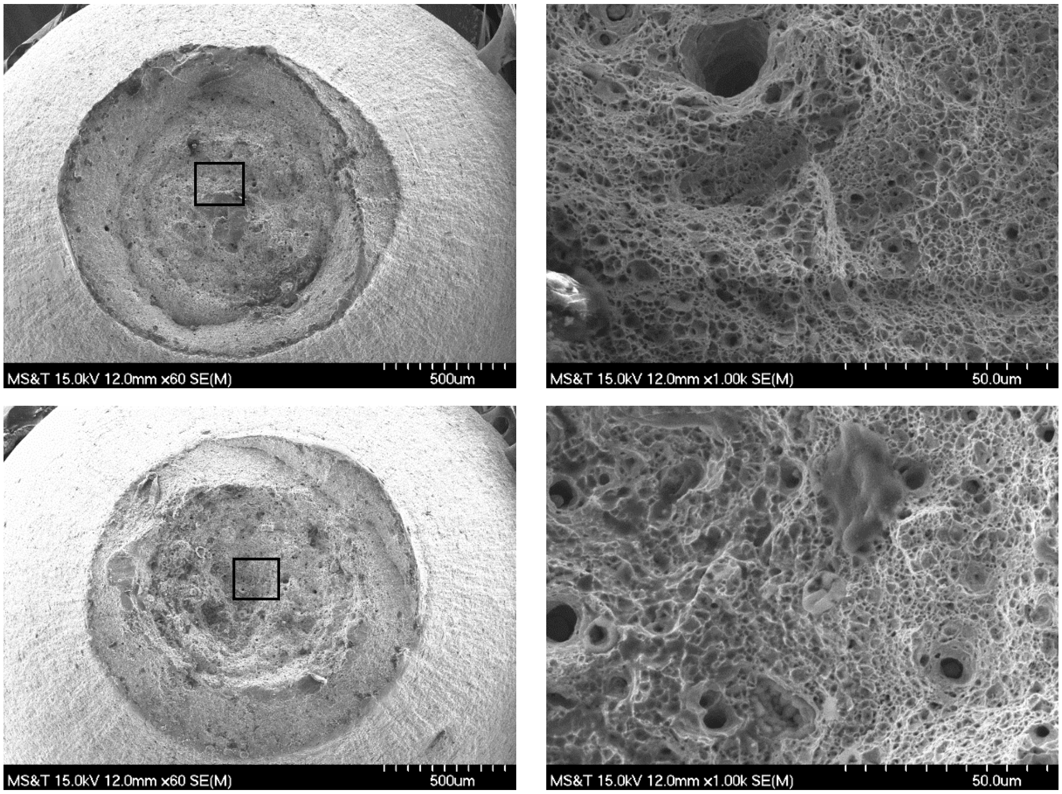

(a)

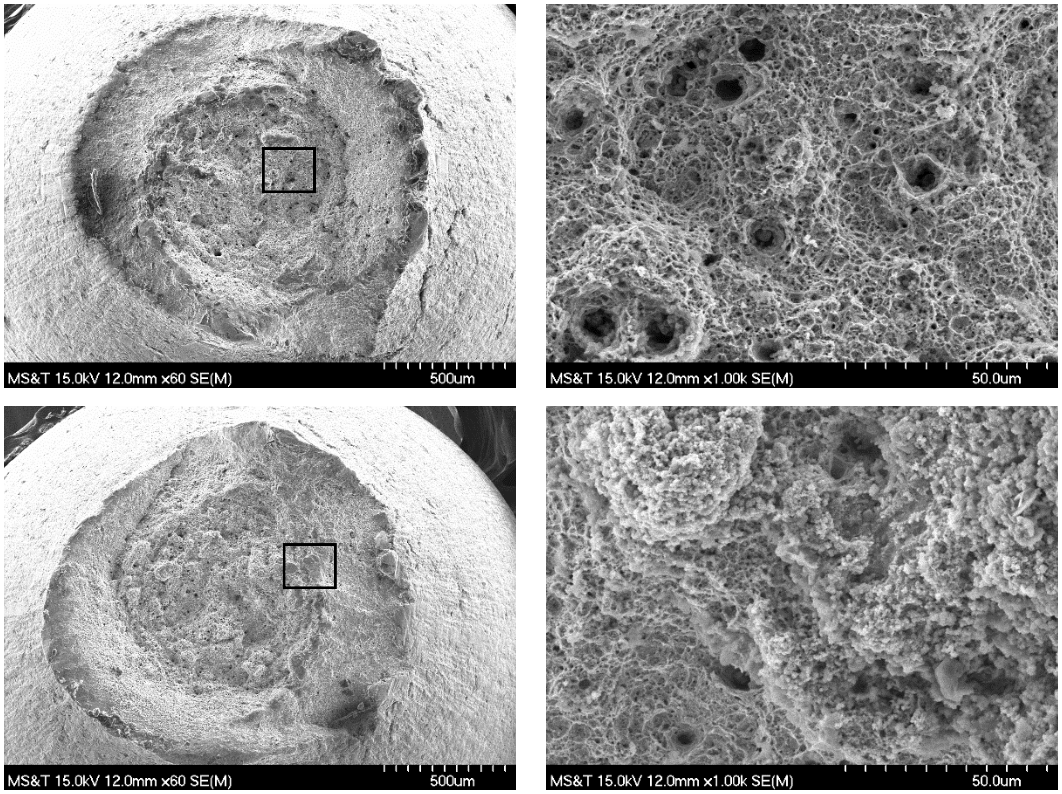
MS&T 15.0kV 12.0mm x60 SE(M) 500um
MS&T 15.0kV 12.0mm x1.00k SE(M) 50.0um
MS&T 15.0kV 12.0mm x60 SE(M) 500um
MS&T 15.0kV 12.0mm x1.00k SE(M) 50.0um

(b)

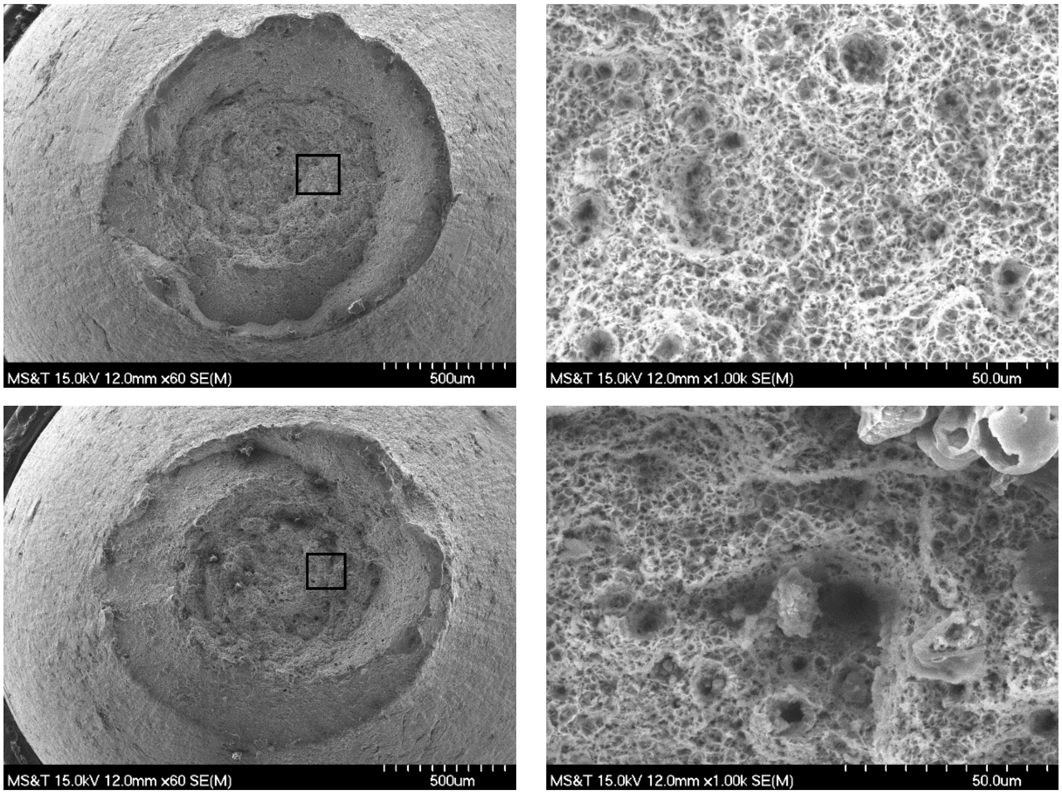
MS&T 15.0kV 12.0mm x60 SE(M) 500um
MS&T 15.0kV 12.0mm x1.00k SE(M) 50.0um
MS&T 15.0kV 12.0mm x60 SE(M) 500um
MS&T 15.0kV 12.0mm x1.00k SE(M) 50.0um

(c)

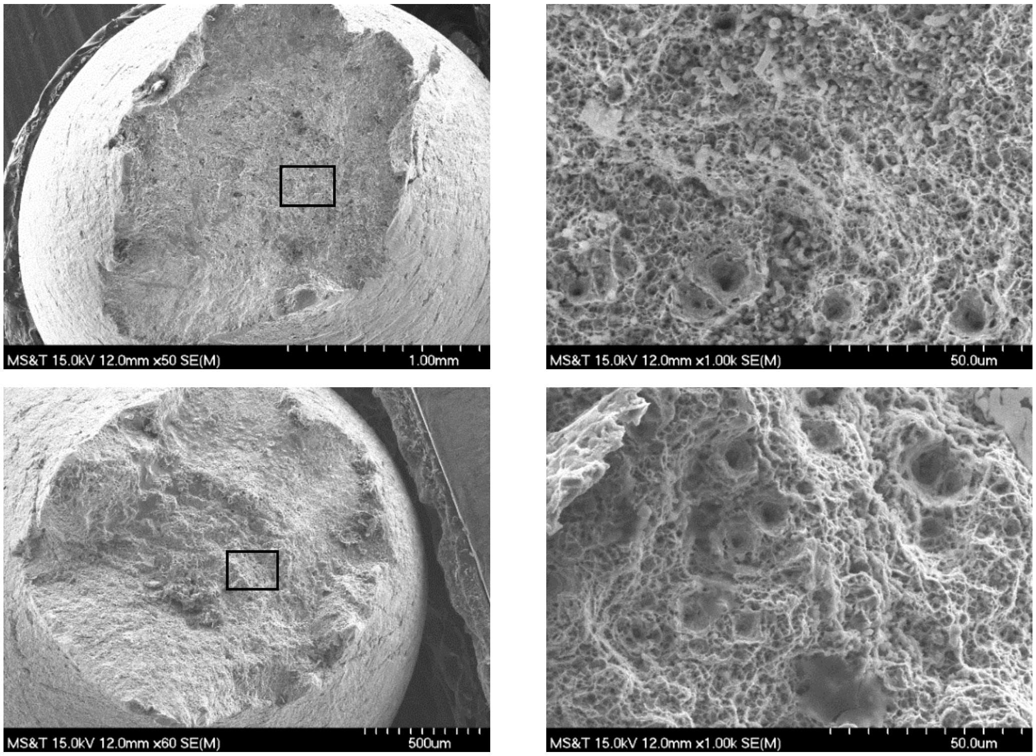

(d)

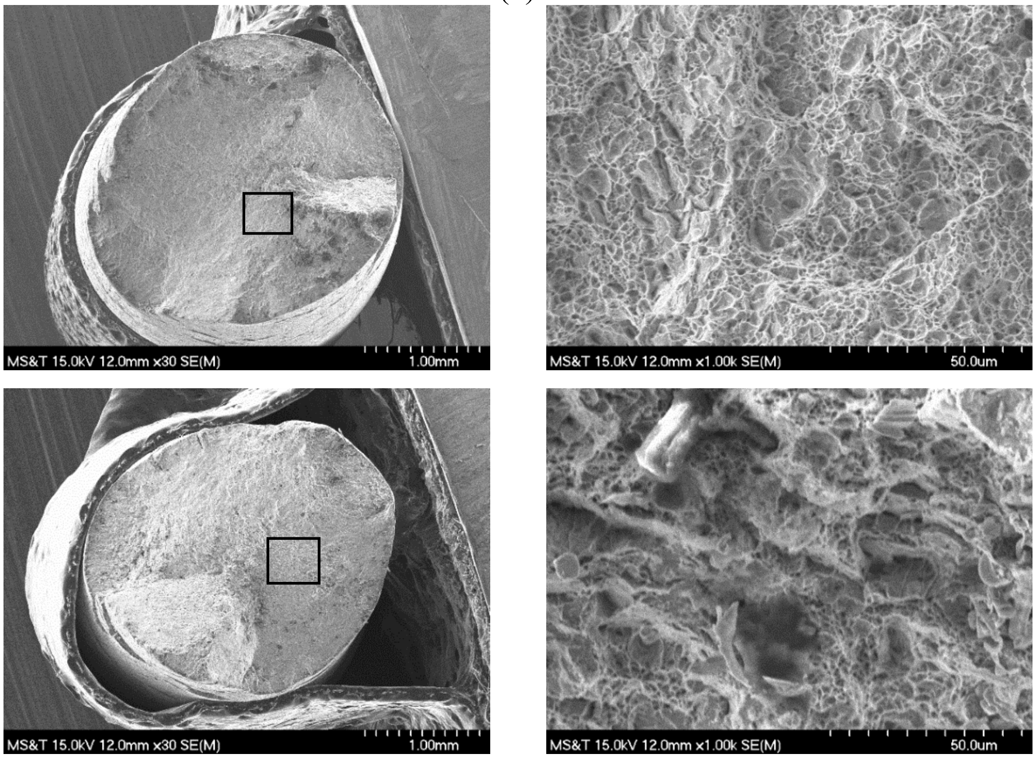

(e)

Figure 4.25 Surface fracture morphology of X65 steel with different potentials after SSRT in simulated soil solution (a) in the air; (b) at OCP; (c) at -790 mV; (d) at -900 mV; and (e) -1200 mV

2.3.6 Conclusions

Based on the experimental results and analysis from one representative sample in each test condition, the following conclusions can be drawn:

1. The enamel coating is subjected to initial compression due to its lower CTE than that of steel, thus less susceptible to tensile cracks. In comparison with epoxy coating, the enamel coating has a higher glass transition temperature, and thus allows an increase of pipeline operation temperature up to 400 °C with a safety factor of approximately 1.25.
2. Enamel residuals remained between anchor points of the substrate steel after the enamel coating had been chipped off due to impact loading. During all the corrosion tests, no further delamination was found, and the CP did not change the coating properties and the mechanical condition at the coating-substrate interface.
3. At the intact coating areas, the more negative potential (up to -1.15 V/SCE) applied in CP, the higher the coating resistance and charge transfer resistance. The CP does not cause debonding between the coating and its steel substrate, decelerates the degradation process of the coating and delay the electrochemical reactions at the steel-electrolyte interface.
4. The resistances of all the damaged coatings are less than 1k Ω cm^2, indicating the loss of their barrier effect in protecting the substrate steel from corrosion. The introduction of CP does not improve the performance of coating once damaged.
5. The resistances against electrolyte penetration into the enamel coating and charge transfer through the steel-electrolyte interface in the intact and damaged enamel coating areas differed by at least 10^4 times after 70 days of tests. Thus, it is important to separate the electrochemical processes in the intact and damaged zones during corrosion tests.

VII. Conclusions

The overarching goal of this study is to improve the corrosion protection and safety, and to reduce the pressure loss and operation cost of hazardous liquid and natural gas pipelines. To achieve the goal, this study aims to explore and develop chemically-bonded porcelain enamel coating for corrosion protection and safety of metallic pipelines. The objective is met by optimizing a mix of several commercial enamels for durability and thermal compatibility, by developing a spraying and heating process of coating for thickness consistency and low surface roughness, by evaluating the porosity, bond strength, and corrosion resistance of enamel-coated specimens, and by evaluating the stress distribution and stress corrosion cracking of enamel-coated pipelines. The chemically-bonded enamel coating has smooth surface for flow efficiency, protects metallic pipelines from corrosion in their life span, and restrains pitting corrosion into a locally breached coating area in the event of unexpected damage.

Through testing the thermal properties, coating microstructures, and short-term corrosion performance, two coatings are chosen for the application in pipeline: Tomatec applied in the wet process, and GP2118 applied in the electrostatic process. It is found that small Fe protrusions grow into the coatings to form anchor points at enamel-steel interfaces. Thus, strong chemical bond is formed between the enamel coating and its substrate steel. The surface roughness of two coatings is only around 1 um so the flow efficiency of transport oil or gas can be improved to a large content.

The long-term electrochemical tests (OCP, LPR, and EIS) show that the coating can prevent the steel pipe from corrosion in the 3.5 wt.% sodium chloride solution. The salt spray test on the large specimens shows that only minor corrosion occurred on the sample surfaces. Besides, cathodic potential (CP) does not change the coating properties and the mechanical condition at the coating-substrate interface. The CP does not cause debonding between the coating and its steel substrate, decelerates the degradation process of the coating and delay the electrochemical reactions at the steel-electrolyte interface. The residual thermal stress at the interface between the enamel coating and steel is only 2.5 MPa so steel just deforms little during the enameling process. The as-received steel and the steel fired at 840 °C for two hours have the same ferrite microstructure so enamel coating will not change the substrate steel property and not increase the susceptibility of the SCC. However, the test results show that the more negative the applied CP, the higher the corrosion rate and more susceptible of the SCC will be.

VIII. Future Work

Electrostatic enameling on full-size pipes requires further validation. In collaboration with pipeline operators, a synchronized enamel spraying and heating process may be tested in a real-world field operation condition to address the heat sink effect of massive steel in application.

IX. References

[1] Koch, G. H., M. P. H. Brongers, N. G. Thompson, Y. P. Virmani, and J. H. Payer. Corrosion Cost and Preventive Strategies in the United States. Final Report No. FHWA-RD-01-156, Federal Highway Administration, 2002.

[2] Managing Corrosion of Pipelines that Transport Crude Oils, Pipeline & Gas Journal 240(3), March 2013.

[3] Prabhu, S.. Gas Pipelines: Internal Corrosion Protection and Fire Prevention. Corrosionpedia Newsletter, January 1, 2016.

[4] https://primis.phmsa.dot.gov/comm/FactSheets/FSInternalCorrosion.htm?nocache=2447).

[5] Schweitzer, P. A. Corrosion-Resistant Piping Systems, p193.

[6] Kehr, A. Fusion-bonded Epoxy Internal Linings and External Coatings for Pipeline Corrosion Protection. Piping Handbook, Chapter B10, 7th Edition.

[7] Yan, D. M., S. Reis, X. Tao, G.D. Chen, R. K. Brow, and M. L. Koenigstein. "Effect of chemically reactive enamel coating on bonding strength at steel/mortar interface." Construction and Building Materials, 28(1): 512-518, 2012.

[8] Tang, F. J., G. D. Chen, R. K. Brow, J. S. Volz, and M. L. Koenigstein. "Corrosion resistance and mechanism of steel rebar coated with three types of enamel." Corrosion Science, 59: 157-168, 2012.

[9] Tang, F. J., X. M. Cheng, G. D. Chen, R. K. Brow, J. S. Volz, and M. L. Koenigstein. "Electrochemical behavior of enamel-coated carbon steel in simulated concrete pore water solution with various chloride concentrations." Electrochimica Acta, 92: 36-46, 2013.

[10] Tang, F. J., G. D. Chen, J. S. Volz, R. K. Brow, and M. L. Koenigstein. “Cement-modified enamel coating for enhanced corrosion resistance of steel reinforcing bars.” Cement and Concrete Composites, 35(1): 171-180, 2013.

[11] Sadeghimeresht, E., N. Markocsan, and P. Nylén. “A comparative study of corrosion resistance for HVAF-sprayed Fe-and Co-based coatings.” Coatings, 6(2): 16, 2016.

[12] Walter, G. W. “A review of impedance plot methods used for corrosion performance analysis of painted metals.” Corrosion Science, 26(9), 681-703, 1986.

[13] Harb, S. V., F. C. dos Santos, B. L. Caetano, S. H. Pulcinelli, C. V. Santilli, and P. Hammer. “Structural properties of cerium doped siloxane–PMMA hybrid coatings with high anticorrosive performance.” Research Advances, 5(20): 15414-15424, 2015.

[14] Zhu, C., R. Xie, J. Xue, and L. Song. “Studies of the impedance models and water transport behaviors of cathodically polarized coating.” Electrochimica Acta, 56(16): 5828-5835, 2011.

[15] Zuo, Y., R. Pang, W. Li, J.P. Xiong, and Y. M. Tang. “The evaluation of coating performance by the variations of phase angles in middle and high frequency domains of EIS.” Corrosion Science, 50(12): 3322-3328, 2008.

[16] Presa, M. R., R. I. Tucceri, M.I. Florit, and D. Posadas. “Constant phase element behavior in the poly (o-toluidine) impedance response.” Journal of Electroanalytical Chemistry, 502(1-2): 82-90, 2001.

[17] Yao, Z., Z. Jiang, and F. Wang. “Study on corrosion resistance and roughness of micro-plasma oxidation ceramic coatings on Ti alloy by EIS technique.” Electrochimica Acta, 52(13): 4539-4546, 2007.

[18] Orazem, M. E., and B. Tribollet. Electrochemical Impedance Spectroscopy, 2nd Edition, John Wiley & Sons, April 2017.

[19] Hirschorn, B., M.E. Orazem, B. Tribollet, V. Vivier, I. Frateur, I., and M. Musiani. “Determination of effective capacitance and film thickness from constant-phase-element parameters.” Electrochimica Acta, 55(21): 6218-6227, 2010.

[20] Córdoba-Torres, P., T. J. Mesquita, O. Devos, B. Tribollet, V. Roche, and R. P. Nogueira. “On the intrinsic coupling between constant-phase element parameters α and Q in electrochemical impedance spectroscopy.” Electrochimica Acta, 72: 172-178, 2012.

[21] Hassan, H. H., E. Abdelghani, and M. A. Amin. “Inhibition of mild steel corrosion in hydrochloric acid solution by triazole derivatives: Part I. Polarization and EIS studies.” Electrochimica Acta, 52(22): 6359-6366, 2007.

[22] Liu, X., J. Xiong, Y. Lv, and Y. Zuo. "Study on corrosion electrochemical behavior of several different coating systems by EIS." Progress in Organic Coatings, 64(4): 497-503, 2009.

[23] Liu, H. H., Y. Shueh, F. S. Yang, and P. Shen. "Microstructure of the enamel-steel interface: cross-sectional TEM and metallographic studies." Materials Science and Engineering: A 149(2): 217-224, 1992.

[24] Yang, X., A. Jha, R. Brydson, and R. C. Cochrane. "An analysis of the microstructure and interfacial chemistry of steel–enamel interface." Thin Solid Films, 443(1): 33-45, 2003.

[25] Tang, F., Y. Bao, Y. Chen, Y. Tang, and G. Chen. "Impact and corrosion resistances of duplex epoxy/enamel coated plates." Construction and Building Materials, 112: 7-18, 2016.

[26] Zhang, J., J. Hu, J. Zhang, and C. Cao. "Studies of water transport behavior and impedance models of epoxy-coated metals in NaCl solution by EIS." Progress in Organic Coatings, 51(2): 145-151, 2004.

[27] Walter, G. W. "A review of impedance plot methods used for corrosion performance analysis of painted metals." Corrosion Science, 26(9): 681-703, 1986.

[28] Hassan, H. H., E. Abdelghani, and M. A. Amin. "Inhibition of mild steel corrosion in hydrochloric acid solution by Triazole derivatives: Part I. polarization and EIS studies." Electrochimica Acta, 52(22): 6359-6366, 2007.

[29] Tang, F. and G. Chen. "Chemically reactive enamel coating of steel rebar for enhanced durability of reinforced concrete structures." International Journal of Structural Engineering, 6(1): 56-72, 2015.

[30] Zhang, X. L., Z. H. Jiang, Z. P. Yao, Y. Song, and Z. D. Wu. "Effects of scan rate on the potentiodynamic polarization curve obtained to determine the Tafel slopes and corrosion current density." Corrosion Science, 51(3): 581-587, 2009.

[31] ASTM D4541-09e1, Standard Test Method for Pull-off Strength of Coatings Using portable Adhesion Tester, American Society for Testing and Materials (ASTM), 2010.

[32] ASTM G14-04, Standard Test Method for Impact Resistance of Pipeline Coatings (falling weight test), American Society for Testing and Materials (ASTM), 2010.

[33] Liu, H. H., Y.S. Shueh, F. S. Yang, and P. Y. Shen. "Microstructure of the enamel-steel interface: cross-sectional TEM and metallographic studies." Materials Science and Engineering: A, 149(2): 217-224, 1992.

[34] PosiTest AT Pull-off Adhesion Testers Quick Guide v.5.0, DeFelsko Corporation.

[35] Lin, W. T, and A. Cheng. “Relationship between microscopy contributions and durability of cement-based composites.” Current Microscopy Contributions to Advances in Science and Technology, A.Méndez-Vilas, Ed., 2012.

[36] Ranade, S., M. Forsyth, and M.Y.J. Tan. “In situ measurement of pipeline coating integrity and corrosion resistance losses under simulated mechanical strains and cathodic protection.” Progress in Organic Coatings, 101: 111-121, 2016.

[37] Xu, L, and F. Y. Cheng. “Assessment of the complexity of stress/strain conditions of X100 steel pipeline and the effect on the steel corrosion and failure pressure prediction.” In the 9th International Pipeline Conference, pp. 319-324, American Society of Mechanical Engineers, September 24, 2012.